# *Studies on*
# *The Crystal Structure and Magnetic Properties of Melilite-Type Compounds*

メリライト型化合物の結晶構造と磁気的性質に関する研究

Takashi Endo

Graduate School of Chemical Sciences and Engineering

Hokkaido University

2018

# Contentes

# Chapter 1

# General Introduction

## 1.1 Introduction

The solid-state chemistry is a branch of inorganic chemistry; it is the study of the synthesis, structure, and properties of materials. It is an interdisciplinary field of chemistry, physics, and crystallography that focus on ways to explore the novel compounds and to investigate their physical properties. Among them, inorganic crystalline compounds show a massive variety of structure and superior functionality due to electronic structures of atoms or ions. Some examples are magnetic properties, electrical properties, optical properties, dielectric properties, and ionic conductor[1]. An inorganic crystalline solid has become a high-performance product like a motor, generator, transistor, integrated circuit, solid cell, and catalyst that has contributed to the energy and electronics fields; thus it has become part of modern technology[2].

Magnetism is one of the major research fields of the solid-state chemistry that are exhibited properties in the magnetic field[3, 4]. It has been studied for a long time, but the theoretical model developed mainly in the 20$^{th}$ century. Weiss proposed the molecular-field formalism for ferromagnetism in 1907[5]; Heisenberg proposed the formulation of a many-body exchange Hamiltonian for the coupling energy of a system of atomic spins in 1928[6]; Néel proposed antiferromagnetism and ferrimagnetism in 1948[7].

Such valuable chemical and physical properties including magnetism cause to the electron interaction especially *d* electrons of transition metal atoms and the *f* electrons of lanthanide atoms[8].In particular, solid state compounds containing transition metals and lanthanide atoms have their *d* and *f* electrons greatly influenced by the surrounding coordination environment, and exhibit entirely different properties from the single element. Therefore, focusing on the combination and crystal structure of atoms, the

discovery of a compound showing a new function is one of the essential roles that the solid-state chemistry field brings to society.

Among them, the solid-state compounds in which transition metals and lanthanide ions are arranged in a layered (two-dimensional) or linear (one-dimensional) form in the crystal unit cell show different magnetic interactions from in a standard (three-dimensional) compounds. Such a group of compounds is called low-dimensional magnetic compounds. Since the discovery of high-temperature superconductivity[9-11] and spin frustration, many-layered oxides have been synthesized, and an understanding of the relationships between crystal structures and physical properties makes rapid progress in strongly correlated electron systems.

One of such layered compounds, the melilite type compounds have attracted attention. Melilite is also called yellow feldspar, which is one of the skarn minerals caused by contact between limestone and magma and refers to a group of compounds classified as pyrosilicates[12]. At first, the crystal structure of a synthetic melilite was determined by Razz and Warren[13,14]. After that, many melilite compounds have been synthesized[12]. Its composition is generally represented by $A_2MM'_2X_7$ ($A$ = alkaline earth metals; $M$, $M'$ = transition metals Si, Ga, Ge; X = O, S). Melilite-type compounds have several different names depending on the mineralogical composition: (1) Akermanite contains divalent metal ion at the $M$ site (e.g., $Ca_2MgSi_2O_7$). (2) Gellenite contains tetravalent metal ion at the $M$ site (e.g., $Ca_2Al(AlSi)O_7$). However, in this thesis, the name "melilite" is used as a generic term for $A_2MM'_2X_7$ compounds.

The crystal structure of many melilite-type compounds is tetragonal. The crystal structure is shown in Figure 1.1. Two kinds of tetrahedrons $MX_4$ and $M'X_4$ exist in the unit cell at a ratio of 1:2. The Tetrahedral $MX_4$ is located at the apex and bottom of the unit cell and is connected to $M'X_4$ by a vertex share, which forms a 5-membered ring. Further, this five-membered ring network layer and $A$ ions layer are alternately stacked in the $c$-axis direction to form a layered structure.

Melilite-type compounds have been reported to exhibit various physical properties depending on the combination of elements entering each crystallographic site. For the first time, natural minerals like melilite such as containing Ca, Mg, Al, and Si were synthesized by sintering or hydrothermal conditions. $Ca_2MM'_2O_7$ (*M* = Mg, Co, Zn; M' =Si, Ge) show the commensurate-incommensurate phase transition at a low temperature due to the misfit between the five-membered ring network layer and *A* ions layer[13,15,16] .

Due to the acoustic and nonlinear characteristics, some melilite-type compounds doped with luminescent ions have been synthesized. The lanthanide-doping melilite, $Ca_2MgSi_2O_7$: $Eu^{2+}$, $Dy^{3+}$ , exhibits absorption by the transition from $4f^7$ to $4f^6\,5d^1$ for $Eu^{2+}$ in the excitation-emission spectrum[17]. This compound is classified as an afterglow phosphor for a long time because the excited $Eu^{2+}$ electrons are confined in $Dy^{3+}$ and then return to the ground state. Besides, Zhang et al. have reported that this compound exhibits mechanical luminescence[18]. Also, alkaline earth melilite is known to have high biocompatibility, and it is expected as a biosensor material combined with optical properties[19].

The acceptor-doped melilite has been interested because of the high ion conducting properties in the field of energy conversion technologies[20, 21]. Ca-doped peroxide melilite $La_{1.54}Sr_{0.46}Ga_3O_{7.27}$ achieved an ionic conductivity of 0.02~0.1 $Scm^{-1}$ at 600~900 °C, due to the passage of interstitial oxygen in two-dimensional layer[22].

Since melilite has the high degree of freedom of chemical composition and a layered structure, it has also been investigated in the field of electromagnetism. The first study on magnetic properties of melilite is the Fe-doped $Ca_2MgSi_2O_7$ [23]. The temperature dependence of the magnetization is 1.12 emu at 4.2K, in a field of 7 T. The magnetization curve increases almost linearly in proportion to the magnetic field due to antiferromagnetic interaction. However, the magnetic properties of this compound are not clear, because the magnetic Fe ions are disordered arrangement in the several crystallography sites and then form complicated magnetic interaction pathways.

The lanthanide-containing melilites $Ln^{3+}{}_2M^{4+}Be^{2+}{}_2O_7$ (*Ln* = Nd - Eu, Tb, Ho - Lu, *M* = Si, Ge) were prepared by Mill et al[24]; they are paramagnetic down to 4.8 K[25]. In general, since *f* electrons of lanthanide ions are present in the inner shell, the interaction between *f* electrons is very weak, and no magnetic anomaly occurs even at low temperatures.

Recently, some melilites show a two-dimensional magnetic behavior due to the square-planar arrangement in an *ab*-plane when the magnetic ions are situated at the *M* sites. Barium-containing melilite, $Ba_2CuGe_2O_7$ shows helical antiferromagnetic structures and an incommensurate-commensurate magnetic transition at 3.26 K[26] due to the Dzyaloshinskii-Moriya interaction, which is allowed by symmetry only for antisymmetric exchange paths. Many tetragonal melilites show magnetic ferroelectricity due to no inversion symmetry in its crystal structure. $A_2CoSi_2O_7$ (*A* = Ca, Sr) shows both antiferromagnetic transition and dielectric anomalies at low temperatures[27].

Although the melilite has the high degree of freedom of chemical composition, few studies have focused on the changes the magnetic interactions between the *d* electrons of transition metal and the *f* electrons of lanthanide atoms. In this study, we have paid attention to the development of new properties derived from the crystallographic structure of the melilite-type compounds. The principal motivation of this investigation is to elucidate the magnetic properties of these compounds.

## 1.2 The scope of this thesis

This thesis is composed of seven Chapters. In Chapter 2 are summarized the principles and methods of the experimental technique used in this study.

First, we studied the magnetic properties of $A_2MM'_2X_7$ compounds containing magnetic ions only at the *M* sites. In Chapter 3, we investigated the crystal structures and magnetic properties of melilite-type oxides, $Sr_2MGe_2O_7$ (*M* = Mn, Co). In these compounds, the magnetic *M* ions form a square-planar lattice in the *ab* plane. Moreover, the *M*-O-*M* superexchange pathway along the *c* axis does not exist, and the possible magnetic pathway is the *M*-O-O-*M* one in the basal *ab* plane. In this study, we measured the magnetic susceptibility and temperature dependence of the specific heat of the synthetic compound to clarify the magnetic properties. Further, powder neutron diffraction measurement was carried out to determine the magnetic structure.

Next, we focused on the melilites containing magnetic ions in both A (= lanthanides) and *M* (= transition metals) sites. Such compounds are expected to show magnetic behavior, reflecting both *d* - *d* interactions, *f* - *f* interactions and *f* - *d* interactions. In chapter 4, we investigated the crystal structures and magnetic properties of new melilite-type oxides $Eu_2MSi_2O_7$ (*M* = Mg, Mn). The results of the powder X-ray diffraction, $^{151}$Mössbauer spectrum, magnetic susceptibility, and specific heat measurements are discussed.

Finally, we have paid our attention to the anion substation to explore further interesting magnetic compounds. In Chapters 5 and 6, we investigated the crystal structures and magnetic properties of new melilite-type oxysulfides $A_2MnGe_2S_6O$ (*A* = Sr, Eu). These compounds are obtained by substituting a part of oxygen ions with sulfur ions. In order to elucidate the magnetic properties, magnetic susceptibility and specific heat measurements have been performed.

Concluding remarks are given in Chapter 7.

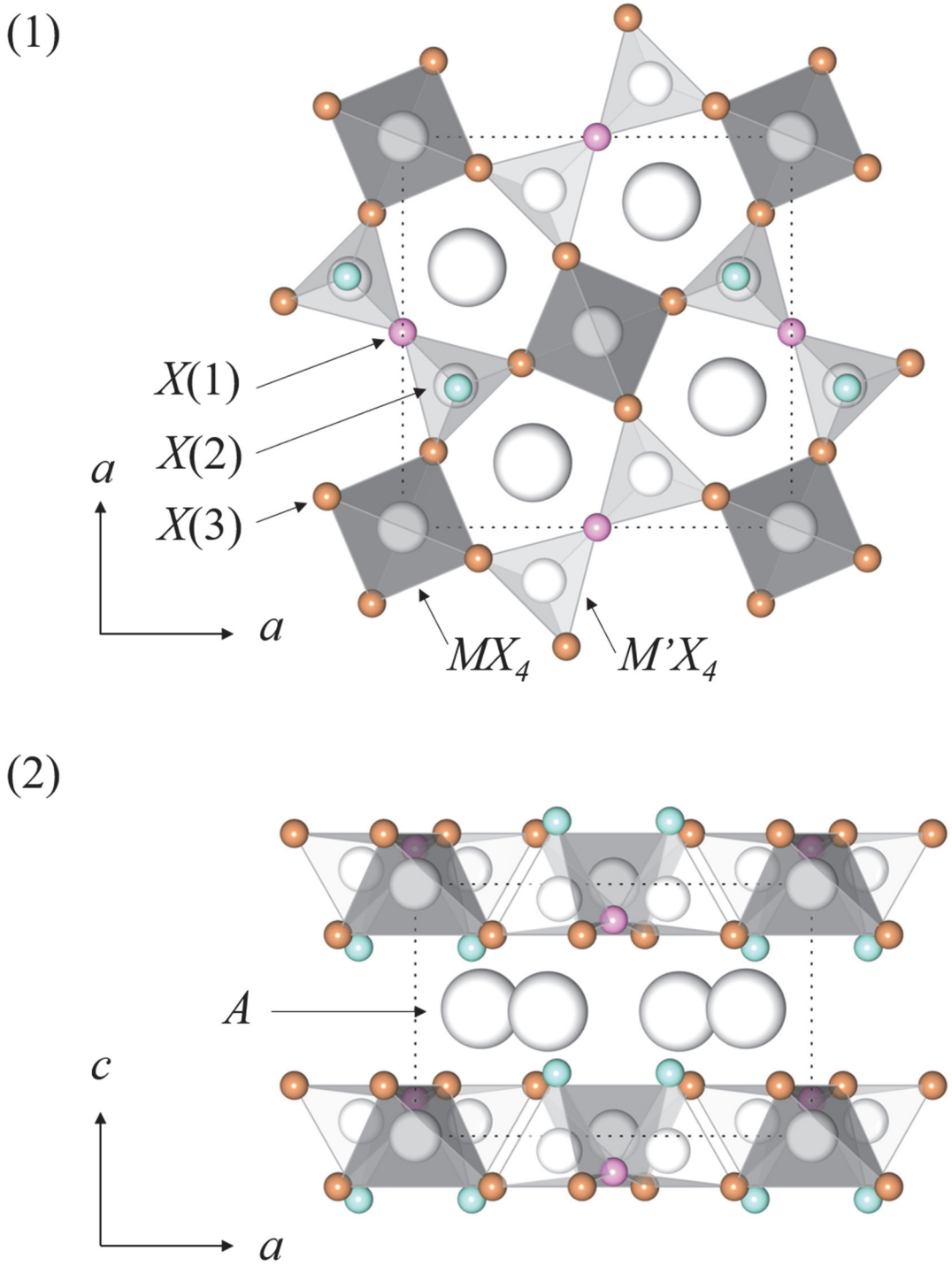


Figure 1.1. Schematic crystal structures of melilite-type compounds $A_2MM'_2X_7$: (1) viewed from the *c* axis, (2) projection of the structure in *ac* plane.

## 1.3 References

(1) Rao, C. N. R.; Winter School in Solid State Chemistry. Indian Institute of Technology, K. *Solid State Chemistry*; M. Dekker: New York, 1974.

(2) Hedvall, J. A. *Solid State Chemistry : Whence, Where and Whither*; Elsevier Pub. Co.: Amsterdam ; New York, 1966.

(3) Goodenough, J. B.; Cotton, F. A. *Magnetism and the Chemical Bond*; Interscience monographs on chemistry; Interscience: New York, 1963; Vol. . Inorgani.

(4) Carlin, R. L. *Magnetochemistry*; Springer-Verlag: Berlin ; Tokyo, 1986.

(5) Weiss, P. L'hypothèse Du Champ Moléculaire et La Propriété Ferromagnétique. *J. Phys. Theor. Appl.* **1907**, *6*, 661–690.

(6) Heisenberg, W. Zur Theorie Des Ferromagnetismus. *Zeitschrift für Phys.* **1928**, *49*, 619–636.

(7) Néel, M. Louis. Propriétés Magnétiques Des Ferrites ; Ferrimagnétisme et Antiferromagnétisme. *Ann. Phys.* **1948**, *12*, 137–198.

(8) Galasso, F. S. *Structure and Properties of Inorganic Solids*; International series of monographs in solid state physics; Pergamon Press: Oxford ; New York, 1970; Vol. v. 7.

(9) Bednorz, J. G.; Müller, K. A. Possible High $T_c$ Superconductivity in the Ba—La —Cu—O System. **1986**, *193*, 267–271.

(10) Nagamatsu, J.; Nakagawa, N.; Muranaka, T.; Zenitani, Y.; Akimitsu, J. Superconductivity at 39 K in Magnesium Diboride. *Nature* **2001**, *410*, 63.

(11) Takahashi, H.; Igawa, K.; Arii, K.; Kamihara, Y.; Hirano, M.; Hosono, H. Superconductivity at 43 K in an Iron-Based Layered Compound LaO1-XFxFeAs. *Nature* **2008**, *453*, 376.

(12) Burzo, E. Melilites and Related Silicates. In *Sorosilicates*; Springer-Verlag: Berlin/Heidelberg, 2009; Vol. 14, pp 29–60.

(13) Louisnathan, S. J. Refinement of the Crystal Structure of a Natural Gehlenite, $Ca_2Al(Al,Si)_2O_7$. *Can. Mineral.* **1971**, *10*, 822–837.

(14) Warren, B. E. The Structure of Melilite (Ca, $Na)_2$(Mg, Al)(Si, $Al)_2O_7$. *Zeitschrift für Kristallographie - Crystalline Materials*. **1930**, p 131.

(15) Seifert, F.; Czank, M.; Simons, B.; Schmahl, W. A Commensurate-Incommensurate Phase Transition in Iron-Bearing Åkermanites. *Phys. Chem. Miner.* **1987**, *14*, 26–35.

(16) Bern, U. Layer Topologyo Stacking Variation , and Site Distortion in Melilite-Related Compounds in the System CaO-ZnO-GeOr-SiO , Trronr . Ts Anvrnnusrnn. **1990**, *7*, 847–858.

(17) Jiang, L.; Chang, C.; Mao, D.; Feng, C. Luminescent Properties of $Ca_2MgSi_2O_7$ Phosphor Activated. **2004**, *27*, 51–55.

(18) Zhang, H.; Yamada, H.; Terasaki, N.; Xu, C.-N. Green Mechanoluminescence of $Ca_2MgSi_2O_7$:Eu and $Ca_2MgSi_2O_7$:Eu,Dy. *J. Electrochem. Soc.* **2008**, *155*, J55.

(19) Zhang, H.; Terasaki, N.; Yamada, H.; Xu, C. N. Mechanoluminescence of Europium-Doped $SrAMgSi_2O_7$ (A = Ca, Sr, Ba). *Jpn. J. Appl. Phys.* **2009**, *48*, 48–51.

(20) Tealdi, C.; Chiodelli, G.; Pin, S.; Malavasi, L.; Flor, G. Ionic Conductivity in Melilite-Type Silicates. *J. Mater. Chem. A* **2014**, *2*, 907–910.

(21) Wei, F.; Gasparyan, H.; Keenan, P. J.; Gutmann, M.; Fang, Y.; Baikie, T.; Claridge, J. B.; Slater, P. R.; Kloc, C. L.; White, T. J. Anisotropic Oxide Ion Conduction in Melilite Intermediate Temperature Electrolytes. *J. Mater. Chem. A* **2015**, *3*, 3091–3096.

(22) Kuang, X.; Green, M. A.; Niu, H.; Zajdel, P.; Dickinson, C.; Claridge, J. B.; Jantsky, L.; Rosseinsky, M. J. Interstitial Oxide Ion Conductivity in the Layered Tetrahedral Network Melilite Structure. *Nat. Mater.* **2008**, *7*, 498.

(23) Nöller, R.; Knoll, H. Magnetic Properties of Calcium-Silicates (Diopside and Gehlenite) Doped with Iron (III). *Solid State Commun.* **1983**, *47*, 237–239.

(24) Mill, B. V.; Bailbakova, G. D. New Compounds with Melilite Structure: $Ln_2SiBe_2O_7$ (Ln = Nd-Eu, Tb, Ho-Lu) and $Ln_2GeBe_2O_7$ (Ln = Nd, Eu, Tb, Ho, Tm-Lu). *Russ. J. Inorg. Chem.* **1990**, *35*, 341–343.

(25) Ochi, Y.; Morikawa, H.; Marumo, F.; Nozaki, H. Structures and Magnetic Properties of Rare Earth Compounds in the Melilite Group. *Yogyo Kyokaishi* **1983**, *91*, 229–235.

(26) Zheludev, A.; Maslov, S.; Shirane, G.; Sasago, Y.; Koide, N.; Uchinokura, K. Field-Induced Commensurate-Incommensurate Phase Transition in a Dzyaloshinskii-Moriya Spiral Antiferromagnet. *Phys. Rev. Lett.* **1997**, *78*, 4857–4860.

(27) Akaki, M.; Kuwahara, H.; Matsuo, A.; Kindo, K.; Tokunaga, M. Successive Magnetic Transitions of $Ca_2CoSi_2O_7$ in High Magnetic Fields. *J. Phys. Soc. Japan* **2014**, *83*, 093704.

# Chapter 2

# Experimental

## 2.1 Solid-state reaction

The solid-state reaction is one of the synthesis methods for the preparation of target compounds from a mixture of starting materials[1–3]. In this method, the diffusion becomes an essential role because of the movement of atoms or molecules in the solid-state reaction much lower than the other (gas or liquid) reaction methods.

The diffusion is the movement of matter due to the concentration gradient. The relationship between the flow velocity in the one direction and the concentration gradient is,

$$J_x = -D\frac{dC}{dx}, \tag{2.1}$$

where $J_x$ is the diffusion flux, $D$ is the diffusion coefficient, and $dC/dx$ is the concentration. The diffusion coefficient $D$ depends on the temperature,

$$D = D_0 exp\left(\frac{\Delta E_d}{RT}\right), \tag{2.2}$$

where $\Delta E_d$ is the activation energy of diffusion, $D_0$ is the frequency factor, $R$ is the gas constant, $T$ is the temperature. If the temperature increases by 100 °C, the diffusion distance increases by several tens of times in a temperature range where reaction proceeds rapidly.

On the other hand, the concentration gradient causes to change with time, the diffusion equation is as follows,

$$\frac{\partial C}{\partial t} = \frac{d[D(\partial C/\partial x)]}{\partial x}, \tag{2.3}$$

when it does not depend on concentration,

$$\frac{\partial C}{\partial t} = D\frac{\partial^2 C}{\partial x^2}, \tag{2.4}$$

this relationship is called Fick's second law and is shown the diffusion length with time t in one-dimension from a boundary located at position x = 0 to infinite where the surface concentration is constant,

$$n(x,t) = n_0\varphi\left(\frac{x}{2\sqrt{Dt}}\right), \tag{2.5}$$

where $n_0$ is the concentration at the starting position (x = 0) and $\varphi$ is the complementary error function. To make the diffusion distance $n$ times, it is necessary to increase the reaction time to $n^2$.

From the eqs.(2.2) and (2.5), the diffusion distance has a higher temperature contribution than the reaction time. Therefore, the synthesis was carried out while changing the reaction temperature variously and fixed the reaction time was set to 12 hours.

## 2.2 X-ray diffraction

### 2.2.1 Crystal systems

The crystal is a solid material in which atoms are periodically ordered in arranged in the three-dimensions[4, 5]. The directions are usually defined to three crystallographic axes, x, y, and z. The volume of the periodically structure is called a unit cell, it contains the primitive translation vector ($a$, $b$, $c$) and the angles between them ($\alpha$, $\beta$, $\gamma$). The all three-dimensional crystals belong to the seven-lattice system (cubic, tetragonal, orthorhombic, hexagonal, rhombohedral, monoclinic, triclinic,). These lattices are

classified by 230 space group with 14 Bravais lattices instead of the original lattice systems in the three-dimensions.

The all lattice positions described to be located in a parallel and equally space plane. The directions of the planes of alignment through the crystal are indicated by the Miller indices ($h = x/a$ , $k = y/b$ , $l = z/c$). The perpendicular distance between any two nearest planes is called the interplanar spacing by the symbol $d_{hkl}$. The calculation of interplanar spacing is carried out by each crystal system. Among then, the interplanar spacing in the tetragonal system is given by the equation,

$$\frac{1}{d_{hkl}^2} = \frac{h^2 + k^2}{a^2} + \frac{l^2}{c^2} \, . \tag{2.6}$$

## 2.2.2 Principle of X-ray diffraction

The X-ray beam is an electromagnetic radiation wave. It has a wavelength range 0.1 to 10 Å which is close to the size of unit cell in crystals and interatomic distances in molecules. When the X-ray irradiate to the crystal, they are scattered from the electron clouds of atoms by the interplanar distance $d_{hkl}$. The X-ray beam strikes the parallel and equally space plane at an angle $\theta$ and is reflected at the angle $\theta'$. When the scattered waves interfere constructively, they are the same integer multiple wavelength but difference path lengths from plane 1 and 2, that is $n\lambda$. The difference in path is equal to the optical path difference which in turn equals $2d \sin\theta$ when $\theta = \theta'$. It is known as the Bragg's law.

$$n\lambda = 2d_{hkl} \sin\theta. \tag{2.7}$$

The intensity of the X-ray diffraction beam depends on the structure factor of crystal structures,

$$I_{hkl} = |F_{hkl}|^2. \tag{2.8}$$

The structure factor is shown by

$$F_{hkl} = \sum_{j=1}^{N} f_j N exp\{2\pi i(hx_j + ky_j + lz_j)\}, \quad (2.9)$$

where $N$ is the number of atoms, $f_j$ is the structure factors of atoms which is proportional to the atomic number, $h$, $k$ and $l$ are Miller indices, $x_j$, $y_j$, and $z_j$, are an atom $j$ at position in a unit cell.

### 2.2.3 Measurement of X-ray diffraction

X-ray diffraction profiles at room temperature were measured with Cu-K$\alpha$ radiation (40 kV, 20mA) on a RINT2200 diffractometer or MultiFlex diffractometer (Rigaku) equipped with a curve graphite monochromator. The data were collected in a step-scanning mode over the $2\theta$ range of 10-120°. The step width and step time are 0.02° and 7.5 s, respectively. The crystal structures of samples were determined by the Rietveld analysis method.

## 2.3 Neutron diffraction

### 2.3.1 The advantage of using neutron diffraction

There are many similarities between X-ray and neutron diffraction, but there are also significant differences. Differences stem from the distinctive properties of thermal neutron themselves.

The neutron has two major features, an electrically neutral particle and has a magnetic moment of spin 1/2. By the former feature, neutrons can penetrate deeply into

most materials. This is an essential advantage in studies of bulk materials and facilitates the use of furnaces, cryostats and pressure cells for studies of materials under conditions encountered in real applications. By the latter feature, it becomes possible to probe the magnetic structure and magnetic dynamics of atomic systems. For magnetically ordered materials, the magnetic powder diffraction pattern may be separated from the nuclear on by comparing patterns above and below the magnetic ordering temperature and thus allowing the determination of the magnetic structure.

The difference in the scattering cross-section is also essential. X-rays are scattered by the electron clouds of atoms, and the X-ray scattering cross-section decreases with scattering angle. On the other hand, neutrons are scattered by the nuclei of atoms, and the neutron scattering cross-sections are independent of scattering angle. Further, X-ray scattering cross-sections increase monotonically with atomic number, while neutron cross-sections vary erratically with atomic number. Their features of neutrons result in useful contrastive effects, including high sensitivity to light elements, the ability to distinguish adjacent elements in the periodic table and scattering powers which can be manipulated by isotopic substitution.

### 2.3.2 Measurement of neutron diffraction

Powder neutron diffraction profiles were measured with two powder neutron diffractometers at the JRR-3M reactor of Japan Atomic Energy Agency (JAEA)[6]. One is a High-Resolution Powder Diffractometer (HRPD) of JAEA. The Ge (331) monochromator ($\lambda$ = 1.82268 Å) of Si (533) monochromator ($\lambda$ = 1.1624 Å) were used. The collimators used were 6'-20'-6', which were placed before and after the monochromator, and between the sample and each detector. The set of 64 detector and collimators, which were placed every 2.5 degrees, rotate around the sample. Another diffractometer is the Kinken powder diffractometer for high efficiency and high-resolution measurements, HERMES, of Institute for Materials Research(IMR), Tohoku

University[7]. The wavelength of the neutron is 1.8196 Å. The quantity of powder samples is 6-10 g; the samples were contained in vanadium cans. The measurements were made at several temperatures (8-300 K for HRPD; 2-300 K for HERMES). The crystal and magnetic structures were determined by the Rietveld method.

### 2.3.3 Magnetic structure amplitude factor[8]

At first, it is supposed that the magnetic moments of atoms are in fixed orientations, e.g., in the simple case that the moments are parallel or antiparallel. The differential magnetic scattering cross- section per unit solid angle is expressed by

$$d\sigma_m = q^2 g^2 J^2 \left(\frac{e^2\gamma}{2mc^2}\right) f^2 = p^2 q^2, \tag{2.10}$$

where $e$ and $m$ are the electron charge and mass, $c$ is the velocity of light, $J$ is the total angular momentum, $g$ is the Landé splitting factor, $\gamma$ is the magnetic moment of the neutron expressed in nuclear magnetons, and $f$ is an amplitude form factor. The q is the magnetic interaction vector defined by

$$\boldsymbol{q} = \varepsilon(\varepsilon \cdot \boldsymbol{K}) - \boldsymbol{K}, \tag{2.11}$$

where $\boldsymbol{K}$ is a unit vector in the direction of the atomic magnetic spin and ε is a unit vector in the direction perpendicular to the effective reflecting planes, i.e., the so-called scattering vector. It follows from the definition of q provide by Eq. (2.11) that **q** lies in the plane of e and $\boldsymbol{K}$ and is perpendicular to wand of magnitude sinα. Thus

$$|\mathbf{q}| = \sin\alpha, \tag{2.12}$$

and $\boldsymbol{K}$ is the direction of the spin is the magnetic material. The vector is in the opposite direction to that of the applied field or the magnetization in the material, simply because the spin moment arises from negative electrons.

It is of crucial importance to consider the interplay of the magnetic and nuclear scattering. The general effect of the polarization can be seen from Halpern and Johnson's expression for the differential scattering cross-section in the case of a magnetic system in which all the magnetic moments are aligned parallel or antiparallel to a single direction, i.e., in a ferromagnetic or a simple antiferromagnetic material. This cross-section is given by

$$d\sigma = b^2 + 2bp\lambda + p^2q^2 \,, \tag{2.13}$$

where $b$ is the nuclear scattering length and $\lambda$ is a unit vector in the direction of the spin of the incident neutron. When the neutron beam is unpolarized, i.e., when the unit vector $\lambda$ can take all possible directions, then the middle term in this expression will average to zero. Therefore, for an unpolarized beam, the cross-section is given by

$$d\sigma = b^2 + p^2q^2 \,. \tag{2.14}$$

In the more usual case where the neutron beam contains all directions of spin, the nuclear-magnetic interference term averages to zero, and the square of the structure amplitude factor $F_{hkl}$ for ($hkl$) reflection is given by the sum of two terms, which represents the nuclear and magnetic intensity respectively.

Thus

$$|F_{hkl}|^2 = \left|\sum_n b_n exp\left\{2\pi i\left(\frac{hx_n}{a} + \frac{ky_n}{b} + \frac{lz_n}{c}\right)\right\}\right|^2 + \left|\sum_n \boldsymbol{q}_n p_n exp\left\{2\pi i\left(\frac{hx_n}{a} + \frac{ky_n}{b} + \frac{lz_n}{c}\right)\right\}\right|^2 \tag{2.15}$$

where the first term is the 2nd power of nuclear structure amplitude factor, and the quantity,

$$\boldsymbol{F}_{mag} = \sum_n \boldsymbol{q}_n p_n exp\left\{2\pi i\left(\frac{hx_n}{a} + \frac{ky_n}{b} + \frac{lz_n}{c}\right)\right\} \tag{2.16}$$

can be regarded as the magnetic structure amplitude factor. Particularly in relation to cooperative magnetic materials in which the magnetic moments point to more than one direction, it should be noted that $\boldsymbol{F}_{mag}$ is a vector quantity. More correctly, the terms in Eqs.(2.15) and (2.16) should include a Debye-Waller factor. The essential feature of Eq. (2.16) is that there is no coherence between the nuclear and magnetic scattering with unpolarized neutrons and the two intensity components are additive.

## 2.4 Rietveld analysis

The Rietveld method is a technique for refining structural parameters (fractional coordinates, thermal parameters, occupation factors, and magnetic moments, etc.) directly from whole powder diffraction profiles without separating reflections. Variable parameters in Rietveld analysis are much more than those in the single-crystal structural refinement despite less structural information contained in powder diffraction data. Peak-shift, background, profile-shape, preferred-orientation, and lattice parameters must be refined in addition to scale factors and structural parameters in the Rietveld analysis.

### 2.4.1 Model function

#### 2.4.1.1 Symmetric profile-shape function

The pseudo-Voight function was used as a symmetric profile-shape function. The Voigt function, i.e., a convolution of the Lorentz function with the Gauss function, can be satisfactorily approximated by a linear combination of the two functions:

$$\phi(\Delta 2\theta) = \eta\phi_L(\Delta 2\theta) + (1-\eta)\phi_G(\Delta 2\theta)$$

$$= \frac{2}{\pi H_K}\left\{1 + 4\left(\frac{\Delta 2\theta}{H_K}\right)^2\right\}^{-1} + (1-\eta)\frac{2\sqrt{ln2}}{\sqrt{\pi}H_K} exp\left\{-4ln2\left(\frac{\Delta 2\theta}{H_K}\right)^2\right\} \quad , \qquad (2.17)$$

with

$$= 1.36603\eta\left(\frac{H_{KL}}{H_K}\right) - 0.47719\left(\frac{H_{KL}}{H_K}\right)^2 + 0.1116\left(\frac{H_{KL}}{H_K}\right)^3, \quad (2.18)$$

and

$$H_k = (H_{kG^5} + 2.69269H_{kG^4}H_{kL} + 2.42843H_{kG^3}H_{kL^2} + 4.47163H_{kG^2}H_{kL^3} + 0.07842H_{kG}H_{kL^4} + H_{kL^5})^{0.2}. \quad (2.19)$$

Here, $\Delta 2\theta = 2\theta_i 2\theta_k$ ($i$: step number, $k$: reflection number, $2\theta i$ : diffraction angle at the $i$th step, and $\theta_k$: Bragg angle for the $k$th reflection), $\phi_L$ is the normalized Lorentz function, $\phi_G$ is the normalized Gauss function, $\eta$ is the fraction of the Lorentzian component, $H_k$ is the full-width-at-half-maximum (FWHM) of $\phi_L$, $\phi_G$,, $H_{kL}$, and $H_{kG}$ are the Lorenzian and Gaussian FWHM's for the Voigt function corresponding to the above pseudo-Voigt function, respectively. $H_{kG}$ is related to the variance of the Gaussian component, $\sigma^2$ by

$$H_{kG} = \sqrt{8\sigma^2 ln2}\,, \quad (2.20)$$

with

$$\sigma^2 = U\,tan^2\theta_k + V\,tan\theta_k + W\,. \quad (2.21)$$

Thus, $H_{kG}$ is a function of the three Gaussian FWHM parameters, $U$, $V$, $W$. The first term in Eq. (2.21) contains a component of Gaussian micro-strain broadening. $H_{kL}$ varies with $\theta_k$ as

$$H_{kL} = X\sec\theta_k + Y\tan\theta_k\,. \quad (2.22)$$

The first part proportional to $\sec\theta_k$ has the angular dependence associated with Scherrer approximation for crystallite-size broadening. $X$ and $Y$ are isotropic-broadening coefficients[9].

2.4.1.2 Profile asymmetry and peak shift

Profile asymmetry is introduced by employing a multi-term Simpson's rule integration devised. In this method, $n$ symmetric profile-shape functions with different Simpson's coefficients for weights, $g_j$, and shifts, $f_j$ are positioned asymmetrically and superimposed with each other:

$$\phi'^{(\Delta 2\theta)} = \frac{1}{3(n-1)} \sum_{j=1}^{n} g_j \, \phi(\Delta 2\theta'), \tag{2.23}$$

with

$$\Delta 2\theta' = \Delta 2\theta + f_i A_s cot 2\theta_k + Z + D_s cos\theta_k + T_s sin 2\theta_k \, . \tag{2.24}$$

Here, $\phi'(\Delta 2\theta)$ is the asymmetric pseudo-Voigt function, and $\Delta 2\theta$ is the $2\theta$ difference modified for profile asymmetry, $A_S$, and peak shifts for each component profile: zero-point shift, $Z$, specimen displacement, $D_S$ and specimen transparency, $T_S$. The corresponding Simpson's coefficients are:

n = 3: $g_1 = g_3 = 1$; $g_2 = 4$,

n = 5: $g_1 = g_5 = 1$; $g_2 = g_4 = 4$; $g_5 = 2$,

n = 7: $g_1 = g_7 = 1$; $g_2 = g_4 = g_6 = 4$; $g_5 = 2$,

$$f_i = \left(\frac{j-1}{n-1}\right)^2 . \tag{2.25}$$

The number of terms, n (=3, 5, 7), in Eq.(2.25) is automatically adjusted for each reflection using its FWHM and $A_S$ must be positive to give reasonable tendencies of peak symmetry.

2.4.1.3 Preferred-orientation function

The preferred orientation is corrected with the MarchDollase function, $P_k$, which is independent of the diffraction geometry and applicable to both plate and needle crystallites. The March-Dollase function is expressed by

$$P_k = \frac{1}{m_k}\sum_{j=1}^{m_k}\left(r^2 cos^2\alpha_j + r^{-1} sin^2\alpha_j\right)^{-3/2} \quad (2.26)$$

where $r$ is an adjustable parameter, and $\alpha_j$ is the angle between the preferred-orientation direction and the $j$th member of the symmetry-equivalent set of $m_k$ diffraction planes. The March-Dollase function displays the best overall performance for structural studies. It converses scattering matter, thereby allowing its use in the quantitative analysis of mixtures.

The referable parameter, $r$, represents the effective sample compression or extension due to the preferred orientation. Its value depends on both the diffraction geometry and the crystallite shape. For samples exhibiting no preferred orientation, $r$ is equal to one.

2.4.1.4 Absorption factor

No absorption correction is needed in Bragg-Brentano-type X-ray powder diffraction using flat-plate samples, because the absorption factor is constant regardless of $2\theta$. On the other hand, absorption correction is indispensable in the Debye-Scherrer geometry, e.g., neutron powder diffraction using cylindrical containers. Rouse et al. gave an analytical approximation of the absorption factor, $A(\theta i)$, for cylindrical samples with the radius, $r_c$:

$$A(\theta_i)exp\{-(a_1 + a_2 sin^2\theta_i)\mu r_c - (a_3 + a_4 sin^2\theta_i)(\mu r_c)^2\} \quad (2.27)$$

with $a_1$ = 1.7133, $a_2$ = -0.0368, $a_3$ = -0.0927, and $a_4$ = -0.3750. The value of the linear absorption coefficient, $\mu$ is calculated from the density of a sample[10].

## 2.4.2 Criteria of fit

The Rietveld refinement process will adjust the refinable parameters until the residual

$$S_y = \sum_i w_i \, (y_i - y_{ci})^2 \tag{2.28}$$

where

$W_i$ = 1/y,

$y_i$ = observed (gross) intensity at the $i$th step,

$y_{ci}$ = calculated intensity at the $i$th step,

is minimized in some sense. In order to judge the result, there are some of $R$-factors as follows:

$$R_{wp} = \left\{ \frac{\sum_i w_i \, (y_i - y_{ci})^2}{\sum_i w_i \, {y_i}^2} \right\}^{1/2}, \tag{2.31}$$

$$R_I = \frac{\sum_k \left| \left( I_k(\text{obs}) \right) - \left( I_k(\text{calc}) \right) \right|}{\sum_k I_k(\text{obs})}, \tag{2.30}$$

$$R_F = \frac{\sum_k \left| \left( I_k(\text{obs}) \right)^{1/2} - \left( I_k(\text{calc}) \right)^{1/2} \right|}{\sum_k (I_k(\text{obs}))^{1/2}}. \tag{2.29}$$

Here, $I_k$ is the intensity assigned to $k$th Bragg reflection at the end of the refinement cycles. The goodness-of-fit indicator, $S$, is

$$S = \left\{ \frac{S_y}{(N - P)} \right\}^{1/2} = R_{wp}/R_e, \tag{2.32}$$

$$R_e = \left\{\frac{(N-P)}{\sum_i w_i y_i{}^2}\right\}^{1/2}, \tag{2.33}$$

where, $N$ is the number of observations (e.g., the number of $y_i$'s used), and $P$ is the number of parameters adjusted.

## 2.5 Measurements of magnetic properties

Most of the magnetic property measurements in this thesis were carried out using a SQUID (superconducting quantum interference device) magnetometer. The SQUID consists of two superconductors separated by thin insulating layers to form two parallel Josephson junctions. The device arrangement is comprised as a magnetometer to detect incredibly small magnetic fields. The Quantum Design Magnetic Property Measurement System (MPMS 5S model) was used as a SQUID magnetometer. This magnetometer is a sophisticated analysis instrument comprised for the study of the magnetic properties of small experimental samples over the temperature range of 1.8 ~ 400 K and the magnetic field up to 5.5 T.

The magnetic property measurements performed in this thesis are (a) the temperature-dependence of the magnetic susceptibility, (b) the field-dependence of the magnetization, and (c) the temperature-dependence of the remnant magnetization. The detailed measurement procedures are as follows:

(a) Magnetic susceptibility. The magnetic susceptibilities were measured after zero field cooling (ZFC) and field cooling (FC) conditions. In the ZFC condition, the samples were cooled in a zero field down to a minimum temperature of each measurement, and then, a magnetic field was applied, and their magnetic susceptibilities were measured in a heating-up process. After the ZFC measurement had ended at a higher temperature than the magnetic transition temperature of the samples, the FC magnetic susceptibility was

measured in a cooling-down process, in which the applied magnetic field was left as it was.

(b) Magnetization. The magnetization was measured at several temperatures by changing the magnetic field strength in the range between 5 and 5 T or between 0 and 5 T. Normally the sample was cooled down to a temperature for the measurement in a zero field (the ZFC condition). In some cases, the magnetization measurements also in the FC condition were carried out.

(c) Remnant magnetization. The temperature dependence of the remnant magnetization was carried out as follows. The samples were cooled down to a minimum temperature of each measurement (below the magnetic transition temperature of the sample) in a zero field. The magnetic field was applied up to 5 T and then reduced to 0 T, and the magnetization measurement was started in a heating-up process.

The samples were contained in the diamagnetic capsules for the medical use. The measured susceptibilities were corrected by extraction the contribution from diamagnetic ionic susceptibilities[11].

## 2.6 Specific heat

Specific heat measurements were performed by the Physical Property Measurement System (Quantum Design, PPMS model). This system uses a relaxation technique. After each measurement cycle, which is a heating period followed by a cooling period, the heat capacity measurements fit the entire temperature response of the sample platform to a model that accounts for both the thermal relaxation of the sample platform to the bath temperature and the relaxation between the sample platform and sample must be considered when the thermal connection shared by the sample and sample platform is poor. The sample in the form of the pellet was mounted on a thin alumina plate with apiezon greases for better thermal contact.

## 2.7 Mössbauer spectroscopy

### 2.7.1 Mössbauer effect

In the case of the electron in atom and molecule systems, the energy levels and resonant absorption of nucleus exist. However, the energy differences between nuclear levels are about 1000 times larger than those between electron levels in the atom and molecule systems. The energy differences between nuclear levels are equivalent to the energy of the γ-ray (~10 ~100 keV). In the case of the emission and absorption of the $\gamma$-ray, the free atomic nucleus recoils, and this recoil energy is large compared with the energy of the $\gamma$-ray. When the $\gamma$-ray is emitted from the nucleus, the conservation law of the energy gives the following relation,

$$E = E_r + E_R \tag{2.34}$$

where $E$ is the difference in energy between the ground and the excited levels in a gamma transition, $E_r$ is the energy of the emitted $\gamma$-ray, and $E_R$ is the recoil energy in the emission process of the $\gamma$-ray. In the absorption process of the $\gamma$-ray, the absorbed nucleus recoil towards the incident direction of the $\gamma$-ray and the $\gamma$-ray needs to have the recoil energy $E_R$ in addition to the energy $E$. Therefore, the loss of the emission and absorption energy of the $\gamma$-ray is $2E_R$.

In general, the $E_R$ is much smaller than $E$ and is negligible. However, in the case of the atomic nucleus, $E_R$ is not so small compared with $E$. Thus, the atomic nuclear recoil resonant phenomenon of $\gamma$-ray is hard to occur.

The recoil energy $E_R$ is written by

$$E_R = \frac{p^2}{2M} = \frac{\left(E_p/c\right)^2}{2M} \tag{2.35}$$

where $M$ is the mass of the emitting nucleus, p is the momentum of emitted or absorbed atoms. The atomic nucleus in the solid state is not free but is restrained at lattice point,

and the recoil can be received by many atoms in the solid state. Thus, $M$ is very large, and the probability of $E_R = 0$ occurs, i.e., recoil-free resonance occurs. This recoil-free resonance is called Mösbauer effect associated with discoverer.

## 2.7.2 Recoil-free fraction

Considering the case of the excitation of the phonon in the emission process of the $\gamma$-ray, $f$ is defined as the probability of the emission of the γ-ray without the excitation of the phonon. The recoil energy of $^{57}$Fe Mössbauer transition is $10^{-3}$ eV, comparable to the energy of the phonon. Therefore, the relation between the recoil energy $E_R$ and the probability $f$ is given by

$$E_R = (1 - f)\hbar\varpi. \tag{2.36}$$

This probability $f$ is called the recoil-free fraction Zero phonon absorption and indicates the probability of Mössbauer effect.

The recoil-free fraction depends on three factors, which are the free-atom recoil energy (which is proportional to $E\gamma^2$), the properties of the solid lattice, and the ambient temperature. Particularly, the relationship between $f$ and last two factors is expressed by using the Debye model[12]

$$f = exp\left[\frac{-6E_R}{k_B\theta_D}\left\{\frac{1}{4} + \left(\frac{T}{\theta_D}\right)^2 \int_0^{\theta_D/T} \frac{xdx}{e^x - 1}\right\}\right] \tag{2.37}$$

where $k_B$ is the Boltzmann constant and $\theta_D$ is the Debye temperature.

### 2.7.3 Measurements of Mössbauer spectrum

The $^{151}$Eu Mössbauer spectrum was measured with a Mössbauer spectrometer VT-6000 (Laboratory Equipment Co.) in the constant acceleration mode. The spectrometer was calibrated with a $^{57}$Fe Mössbauer spectrum of $\alpha$-Fe at room temperature. A $^{151}SmF_3$ radiation source (1.85 GBq) was used, and the γ-rays were detected with a NaI scintillation counter. The source vibrates against the sample and the energy of the γ-ray having only one wavelength is modulated by Doppler effect. The transmission of the γ-ray vs. the Doppler velocity is a Mössbauer spectrum. $EuF_3$ was used as a reference standard for the chemical isomer shift. The sample was lapped in an aluminum foil.

### 2.7.4 Hyperfine interactions

The nuclear transitions are very sensitive to the local environment of the atom, and Mössbauer spectroscopy is a sensitive probe of the different environments at an atom occupies in a solid material. With the change of electron state, the nuclear levels change in which causes the peak shift and/or splitting in Mössbauer spectrum. Therefore, the spectrum gives the hyperfine structure. Isomer shift, second-order Doppler shift, and electric quadrupole interaction related to this study are explained as follows.

### 2.7.5 Isomer shift

The atomic nucleus is surrounded by electronic charge. The energy of interaction can be computed classically by considering a uniformly changed spherical nucleus embedded in its *s*-electron charge cloud. Since there exists the Coulomb interaction between the electron and nucleus, a change in the chemical state will result as a shift of the nuclear levels.

In the Mössbauer spectrum, this effect is observed as the shift of the spectrum. Such an energy shift due to the chemical state is called as an isomer shift, γ, which is written by

$$\delta = \frac{4\pi}{5} Ze^2 R_n^2 \left(\frac{\Delta R_n}{R_n}\right) \{|\Psi_A(0)|^2 - |\Psi_S(0)|^2\} \tag{2.38}$$

where $Z$ is the atomic number, $R_n$ is the radius of the nucleus, $|\Psi_A(0)|^2$ and $|\Psi_S(0)|^2$ are the density of electron at the nucleus of absorber and source, respectively. Isomer shift depends on two factors. One is the difference between the radius of the ground state and excited state. Another is the electronic charge density at the nucleus, which is basically an atomic or chemical parameter since it is affected by the valence state of the atom.

## 2.7.6 Electric quadrupole interaction

When the nuclear spin $I$ is 0 or 1/2, the nuclear change is spherical symmetric and has zero quadrupole moment. When $I \geq 1$, on the other hand, the change distribution of the nucleus is distorted from spherical symmetry, and the nucleus has non-zero quadrupole moment. The magnitude of the change deformation of a nucleus is described as the nuclear quadrupole moment $Q$, given by

$$eQ = \int \rho_d r^2 (3\cos^2\theta - 1) d\tau \tag{2.39}$$

where, $\rho_d$ is the change density in a volume element $d\tau$, which is at a distance r from the center of the nucleus and making an included angle $\theta$ to the nuclear spin quantization axis. The sign of $Q$ depends on the shape of the deformation. A negative quadrupole moment indicates that the nucleus is oblate or flattened along the spin axis, whereas for a positive moment it is prorate or elongated.

In a chemical bonded atom, the electronic charge distribution is usually not spherically symmetric. The electric field gradient at the nucleus is defined as a tensor,

$$E_{ij} = -V_{ij} = -\left(-\partial^2 V/\partial x_i \partial x_j\right) \ (x_i, x_j = x, y, z), \tag{2.40}$$

where $V$ is the electrostatic potential. It is customary to define the coordinate axis for the system and $V_{ZZ} = eq$ is the maximum value of the field gradient. The orientation of the nuclear-quantized axis with respect to the principal axis, z, is quantized. There is an interaction energy between $Q$ and $eq$ which is different for each possible orientation of the nucleus.

The Laplace equation requires that the electric field gradient is traceless tensor, so that

$$V_{xx} + V_{yy} + V_{zz} = 0. \tag{2.41}$$

Consequently, only two independent parameters are needed to specify the electric field gradient completely, and the two, which are usually chosen, are $V_{zz}$ and an asymmetry parameter $\eta$ defined as

$$\eta = \frac{V_{xx} - V_{yy}}{V_{zz}}, \tag{2.42}$$

using the relationships of $|V_{zz}| > |V_{yy}| \geq |V_{xx}|$ ensures that $0 \leq \eta \leq 1$.

The Hamiltonian of the quadrupole interaction can be written as

$$H_{quad} = \frac{eQ}{2I(2I-1)}\left(V_{zz}\hat{I}_z^2 + V_{xx}\hat{I}_x^2 + V_{yy}\hat{I}_y^2\right), \tag{2.43}$$

where $\hat{I}_z$, $\hat{I}_x$ and $\hat{I}_y$ are the nuclear spin operators. Using Eq. (2.42), the Hamiltonian becomes,

$$H_{quad} = \frac{eQ}{2I(2I-1)}\left\{3\hat{I}_z^2 - I(I+1) + \eta\left(\hat{I}_+^2 + \hat{I}_-^2\right)\right\} \tag{2.44}$$

where $\hat{I}_+$, $\hat{I}_-$ and are shift operators. The calculated matrix elements of $H_{\text{quad}}$ are

$$\langle \Psi_{\mathrm{I},I_z} | H_{quad} | \Psi_{\mathrm{I},I_z} \rangle = \frac{e^2 qQ}{4I(2I-1)} \{ 3\hat{\mathrm{I}}_z^2 - I(I+1) \} \tag{2.45}$$

and

$$\langle \Psi_{\mathrm{I},I_z} | H_{quad} | \Psi_{\mathrm{I},I_z} \rangle = \frac{e^2 qQ}{8I(2I-1)} \eta \{ (I \mp I_z)(I \pm I_z + 1)(I \mp I_z - 1)(I \pm I_z + 2) \}^{1/2} \tag{2.46}$$

and the other matrix elements are equal to zero. The eigenvalues of $H_{\mathrm{quad}}$ are obtained by calculating the determinant,

$$\left| \langle \Psi_{\mathrm{I},I_z} | H_{quad} | \Psi_{\mathrm{I},I_z} \rangle - E\delta_{I_z, I_z'} \right| = 0. \tag{2.47}$$

As an example, a typical energy level scheme with the quadrupole interaction for $^{151}$Eu ($I$ = 5/2 → $I$ = 7/2).

## 2.8 Diffuse reflectance spectrum

The optical absorption edge of semiconductor is characterized by an absorption constant which rises exponentially with photon energy:

$$(\mathrm{h}\nu\alpha)^{1/n} = A(\mathrm{h}\nu - E_g) \tag{2.48}$$

where h is the planck's constant, v is the frequency of vibration, $\alpha$ is the absorption coefficient, A is proportional constant. $E_g$ is the band gap, n is dependent on whether the band-gap transition, i.e. for direct allowed transition (n = 1/2), for direct forbidden transition (n = 3/2), for indirect allowed transition (n = 2), for indirect forbidden transition (n = 3) [13–15]. Therefore, an optical band gap can be calculated by measuring the absorption coefficient.

Diffuse reflection measurements are known as a method for determining the absorption coefficient of a powder sample. When white light is applied to a powder sample, the specular and the diffuse reflected light emerges from the surface and interior

of sample respectively. Among them, the diffuse reflected light shows a spectrum like transmission spectrum except scattering effect. Kubelka and Munk suggested that the scattering effect is a first order phenomenon[16],

$$\mathrm{f}(R_\infty) = \frac{(1-R_\infty)^2}{2R_\infty} = \frac{K}{S} \tag{2.49}$$

where $\mathrm{f}(R_\infty)$ is the Kubelka-Munk function, $R_\infty$is the absolute reflectance when the sample is infinitely thick, $K$ is the molecular absorption coefficient, $S$ is the scattering coefficient[17]. In actual measurement, it is obtained by the relative reflectance of a standard powder (KBr), since the determination of absolute reflectance is difficult. After the diffuse reflection spectrum is converted by Kubelka-Munk function, the optical absorption edge can be described,

$$(\mathrm{h}\nu R_\infty)^{1/n} = A\left(\mathrm{h}\nu - E_g\right). \tag{2.50}$$

Here, plotting curve of this relationship with $\mathrm{h}\nu$[eV] : tauc plot , a line is drown from the inflection on the curve to horizontal axis becomes the band gap $E_g$ value[18 19].

## 2.9 Electronic structure calculation

The density functional theory is a method to calculate the potential and physical properties of a substance from the electron density. For solid state crystals which fixed atomic position, approximation by Local Spin Density can be applied to the calculation. The total energy is described within the spin densities $\rho_\sigma(r)$ as,

$$\begin{gathered}\mathrm{E}_{tot}(\rho\uparrow,\rho\downarrow) = \\ T_S(\rho\uparrow,\rho\downarrow) + E_{ee}(\rho\uparrow,\rho\downarrow) + E_{Ne}(\rho\uparrow,\rho\downarrow) + E_{xc}(\rho\uparrow,\rho\downarrow) + E_{NN}\end{gathered} \tag{2.51}$$

where labeled conventionally as, the kinetic energy, the electron-electron repulsion, the nuclear-electron attraction, exchange-correlation energies, and the repulsive Coulomb energy of the fixed nuclei and electric contributions, respectively. The exchange-

correlation energies ($E_{xc}$) have several forms in literatures. The WIEN2k program package employs the full−potential linearized augmented plane wave + local orbitals (FP−LAPW+lo) method with the generalized gradient approximation (GAA) [20, 21].

## 2.10 References

(1) Fick, A. Ueber Diffusion. *Ann. Phys.* **1855**, *170*, 59–86.

(2) 日本化学会. 無機化合物; 実験化学講座 / 日本化学会編; 丸善: 東京, 2005; Vol. 23.

(3) 柳田博明; 永井正幸. セラミックスの科学; 技報堂出版: 東京, 1993.

(4) McLachlan, D. *X-Ray Crystal Structure*; McGraw-Hill: New York, 1957.

(5) James, R. W. *The Optical Principles of the Diffraction of X-Rays*; The crystalline state / edited by Sir W.H. Bragg and W.L. Bragg; G. Bell: London, 1954; Vol. 2.

(6) MORII, Y. Special Issue-New Evolution of the Powder Diffraction Method. Neutron Powder Diffraction with Monochromated Steady-State Beam. *Nihon Kessho Gakkaishi* **1992**, *34*, 62–69.

(7) Ohoyama, K.; Kanouchi, T.; Nemoto, K.; Ohashi, M.; Kajitani, T.; Yamaguchi, Y. The New Neutron Powder Diffractometer with a Multi-Detector System for High-Efficiency and High-Resolution Measurements. *Jpn. J. Appl. Phys.* **1998**, *37*, 3319.

(8) Bacon, G. E. *Neutron Diffraction*; Monographs on the physics and chemistry of materials; Clarendon Press: Oxford [Eng.], 1975.

(9) Young, R. A. *The Rietveld Method*; International Union of Crystallography monographs on crystallography; International Union of Crystallograhy: [Chester, England], 1993; Vol. 5.

(10) Rouse, K. D.; Cooper, M. J.; York, E. J.; Chakera, A. Absorption Corrections for Neutron Diffraction. *Acta Crystallogr. Sect. A* **1970**, *26*, 682–691.

(11) König, E.; König, G.; Hellwege, K. H.; Hellwege, A. M. *Magnetische Suszeptibilitäten*; Landolt-Börnstein Zahlenwerte und Funktionen aus

Naturwissenschaften und Technik, Neue Serie / Gesamtherausgabe, K.-H. Hellwege; Springer: Berlin ; Tokyo, 1984; Vol. Gruppe 2.

(12) Mahesh. K.; On the Usability of Debye Theory in Mössbauer Spectroscopic Studies. *Phys. status solidi,* **1974**, 695–700.

(13) Davis, E. A.; Mott, N. F. Conduction in Non-Crystalline Systems V. Conductivity, Optical Absorption and Photoconductivity in Amorphous Semiconductors. *Philos. Mag.* **1970**, *22*, 903–922.

(14) America, O. S. of; Bass, M.; Li, G.; Stryland, E. Van. *Optical Properties of Materials, Nonlinear Optics, Quantum Optics*; Handbook of optics / sponsored by the Optical Society of America ; Michael Bass, editor in chief; McGraw-Hill: New York, 2010; Vol. v. 4.

(15) Hecht, E. *Optics*; Pearson: Boston, 2017.

(16) Džimbeg-malčić, V.; Barbarić-mikočević, Ž.; Itrić, K. Kubelka-Munk Theory in Describing Optical Properties of Paper (1). *Tech. Gaz.* **2011**, *18*, 117–124.

(17) Kubelka, P.; Munk, F. Ein Beitrag Zur Optik Der Farbanstriche. *Z. Techn. Phys.* **1931**, *12*, 593.

(18) Tauc, J.; Grigorovici, R.; Vancu, A. Optical Properties and Electronic Structure of Amorphous Germanium. *Phys. Stat. Sol* **1966**, *15*, 627.

(19) Abelès, F. *Optical Properties of Solids*; North-Holland: Amsterdam, 1972.

(20) Blaha, P.; Schwarz, K.; Madsen, G.; Kvasnicak, D.; Luitz, J. WIEN2k, An Augmented Plane Wave Plus Local Orbitals Program for Calculating Crystal Properties.; 2001.

(21) Koller, D.; Tran, F.; Blaha, P. Merits and Limits of the Modified Becke-Johnson Exchange Potential. *Phys. Rev. B* **2011**, *83*, 195134.

# Chapter 3

# Magnetic and Neutron Diffraction Study on Melilite-Type Oxides $Sr_2MGe_2O_7$ ($M$ = Mn, Co)

## 3.1 Introduction

Layered transition metal oxides are potential targets for exploring interesting magnetic and electronic properties because of their low-dimensional characteristics[1]. As one of such fascinating systems, the magnetic properties of melilite-type oxides have been attracting interests. They have a general formula $A_2MM'_2O_7$ ($A$ = larger cations such as alkali earth and lanthanide ions; $M$, $M'$ = smaller divalent to tetravalent ions), and typically adopt a tetragonal structure (space group $P\text{-}42_1m$) with a unit cell of $a \approx 8$ Å and $c \approx 5$ Å. The schematic crystal structure of the title compounds is illustrated in Figure 3.1. In this structure, the $M$ and $M'$ ions occupy tetrahedral sites and these tetrahedra form a two-dimensional (2D) network in the $ab$-plane, and larger $A$ ions locate between the networks[2–4].

The melilite-type oxides show a variety[5–16] of magnetic properties as listed in Table 3.1. For example, $Ba_2MGe_2O_7$ ($M$ = Mn, Co, Cu) show the 2D antiferromagnetic behavior due to the square-planer arrangement of the magnetic $M$ ions, although the shortest $M$–$M$ distance is along the $c$-axis. At low temperatures an antiferromagnetic transition ($M$ = Mn)[9], multiferroic behavior derived from antiferromagnetic and ferroelectric transitions under the magnetic field (Co)[10–14], and spiral antiferromagnetic ordering and incommensurate-commensurate magnetic transition (Cu) have been observed[15] . In addition, by introducing further magnetic ions into the $M'$ and $A$ sites, the

spin-glass behavior in $Ba_2Fe_2GeO$[17,18], and ferrimagnetic ordering between $Eu^{2+}$ and $Mn^{2+}$ moments in $Eu_2MnSi_2O_7$ have been found[5].

In order to understand the structural and magnetic properties of melilite-type oxides, we focus our attention on the strontium melilites $Sr_2MGe_2O_7$ ($M$ = Mn, Co). According to Naruse *et al*[19], these compounds are isostructural to the barium analogues; the substitution of Sr for Ba at the $A$ site should shorten the $M$–$M$ distance along the $c$-axis. This may change the relationship between the intralayer and interlayer magnetic interactions in the melilites. Therefore, we investigated the syntheses, crystal structures, and magnetic properties of $Sr_2MGe_2O_7$ ($M$ = Mn, Co, Zn) by means of X-ray and neutron powder diffraction, magnetic susceptibility and specific heat measurements.

## 3.2 Experimental procedures

### 3.2.1 Synthesis

Polycrystalline samples (0.5 g) of $Sr_2MGe_2O_7$ ($M$ = Mn, Co, Zn) were prepared by the standard solid-state reaction. As starting materials, SrO, $SrCO_3$, MnO, CoO, ZnO, and $GeO_2$ were used. The SrO was prepared by the decarbonation of $SrCO_3$ at 1400ºC for 12 h. These starting materials were weighed out in a stoichiometric ratio and well mixed in an agate mortar. The reaction mixture for $Sr_2CoGe_2O_7$ was calcined in air at 1200 ºC for 12 h. For $Sr_2MnGe_2O_7$, the mixture was pressed into pellets and enclosed in a platinum tube. Then the platinum tube was sealed in an evacuated quartz tubes and heated at 1200ºC for 24 h.

### 3.2.2 Powder diffraction analysis

Powder X-ray diffraction (XRD) measurements were performed at room temperature using a Multi-Flex diffractometer (Rigaku) with a Cu Kα X-ray radiation source equipped with a curved graphite-monochromator. The data were collected by step-scanning in the angle range of $10^{o} \leq 2\theta \leq 120^{o}$ at a step size of 0.02º. For $Sr_2MnGe_2O_7$ and $Sr_2CoGe_2O_7$, the neutron powder diffraction (NPD) measurements were collected in the range $3^{o} \leq 2\theta \leq 152^{o}$ using $2\theta$ step size of 0.1º with the wavelength of 1.84843 Å, at low temperature (2.5 – 20 K). The measurements were performed on the Kinken powder diffractometer for high-resolution measurements, HERMES, of the Institute for Materials Research (IMR), Tohoku University[20], installed at the JRR-3M Reactor in the Japan Atomic Energy Agency (JAEA), Tokai. The XRD and NPD data were analyzed by the Rietveld method using the program RIETAN-FP[21], and the crystal and magnetic structures were drawn by using the VESTA program[22].

### 3.2.3 Magnetic measurements

The temperature dependence of the magnetic susceptibilities were measured with a SQUID magnetometer (Quantum Design, MPMS-5S). The measurements were performed under both zero-field-cooled (ZFC) and field-cooled (FC) conditions over the temperature range between 1.8 - 300 K in an applied magnetic field of 0.1 T. The field dependence of the magnetizations was measured over the magnetic field rage between -5 and 5 T at 5 K. The remnant magnetization measurements were also performed. The sample was cooled to 1.8 K in a zero magnetic field. The magnetic field was applied up to 5 T and then reduced to zero, and the magnetization measurements were performed in the temperature range from 1.8 K to 30 K.

### 3.2.4 Specific heat measurements

The specific heat measurements were performed using a relaxation technique with a commercial physical property measurement system (Quantum Design, PPMS) in the temperature range of 1.8 - 300 K. The pelletized sample was mounted on a thin alumina plate with Apiezon N-grease for better thermal contact.

## 3.3 Results and discussion

### 3.3.1 Crystal structure

The melilite-type oxides $Sr_2MGe_2O_7$ ($M$ = Mn, Co, Zn) were successfully prepared. They were obtained as white ($M$ = Mn, Zn) or blue (Co) colored polycrystalline samples. Their X-ray diffraction (XRD) profiles are shown in Figure 3.2. The observed peaks were indexed on a tetragonal unit cell ($a \sim 8$Å, $c \sim 5$Å) with the space group $P\text{-}42_1m$, which is typical for the melilite-type compounds [2,3]. Among these three compounds, only the $Sr_2MnGe_2O_7$ contains a small amount of $\alpha$-$Sr_2GeO_4$ (~ 1%) as an impurity[23]. All XRD data were analyzed by the Rietveld method using the structural model for $Sr_2ZnGe_2O_7$[24]. The calculated profiles are plotted in Figure 3.2, and the refined structural parameters and reliability factors are summarized in Table 3.2. For Co and Zn compounds, the structural parameters are in good agreement with the results reported previously[19,24]. On the other hand, the lattice parameters of Mn compound are different from those by earlier researchers [19]. This is due to the fact that the oxidation state of Mn ions are different between our sample and earlier researcher's sample (ref.19). In this study, we prepared $Sr_2MnGe_2O_7$ in an evacuated quartz tube. On the other hand, the earlier researchers prepared their sample in air. In order to clean this point, we also prepared $Sr_2MnGe_2O_7$

in air. The lattice parameters prepared in air are in good agreement with those by earlier researchers, which will be shown in Table 3.3 and Figure 3.3.

The neutron powder diffraction (NPD) measurements for $Sr_2MnGe_2O_7$ and $Sr_2CoGe_2O_7$ (at 20, 2.5 K) were carried out to obtain further information about the structural and magnetic properties. The NPD profiles were shown in Figure 3.2 and Figure 3.3. For the data collected at 20 K, all observed peaks were indexed with the structural model determined by the XRD measurement at room temperature. Thus, no structural phase transition occurs at low temperatures. We carried out the Rietveld analysis of these NPD data taking into account the possibilities of the cation disorder between *M* and *M'* sites and the oxygen defect. However, no evidence of such possibilities has not been found. The structural parameters for Mn and Co compounds are shown in Table 3.4 and Table 3.5, respectively. At 2.5 K, additional diffraction peaks are observed. As will be discussed later, they are due to an antiferromagnetic ordering of $Mn^{2+}$ or $Co^{2+}$ moments.

The schematic crystal structure of the title compounds is illustrated in Figure 3.1, and some selected interatomic distances calculated from the structural parameters are listed in Table 3.6. In this structure, both the *M* and Ge ions occupy the tetrahedral sites, and the $MO_4$ and $GeO_4$ tetrahedra form a two-dimensional network by sharing corner-oxygen ions. On the other hand, the Sr ions are coordinated by eight oxygen ions and locate between networks. The bond valence sums (BVS)[25,26] are calculated from the interatomic distances, and they are also showed in Table 3.6. These values indicate that the Sr and *M* ions are in the divalent state and the Ge ion is in the tetravalent state. The magnetic ions ($Mn^{2+}$ and $Co^{2+}$) occupy the *M* site. In this structure, the *M*-O-*M* super exchange pathway along the *c*-axis does not exist. The possible magnetic pathway is the *M*-O-O-*M* one in the basal *ab*-plane.

## 3.3.2 Magnetic susceptibility

### 3.3.2.1 $Sr_2MnGe_2O_7$

Figure 3.6 shows the temperature dependence of the magnetic susceptibility for $Sr_2MnGe_2O_7$. No deviation is found between the ZFC and FC in the measured temperature range. The data were fitted by the Curie-Weiss law between 100 and 300 K, using an equation,

$$\chi_M = \frac{C}{T-\theta} + \chi_{TIP} \tag{3.1}$$

where $C$, $\theta$, and $\chi_{TIP}$ mean the Curie constant, Weiss constant, and temperature independent paramagnetic susceptibility, respectively. The effective magnetic moment ($\mu_{eff}$) was determined to be 5.84(2) $\mu_B$/ Mn, which is close to the spin-only value expected for $Mn^{2+}$ ($3d^5$) ion in a high-spin state (5.92 $\mu_B$). The Weiss constant $\theta$ is -10.6(1) K, and the negative $\theta$ value indicates that the predominant magnetic interaction between $Mn^{2+}$ ions is antiferromagnetic.

At low temperatures, the data show a maximum at 6.0 K and another anomaly at ~4 K. (see the inset of Figure 3.6). The former feature is often found in the low dimensional magnet [1,27]. In this compound, the arrangement of the $Mn^{2+}$ ions can be regarded as the square-planar lattice if the interlayer magnetic interaction is much weaker. The observed magnetic susceptibility (5 ~ 300 K) was fitted by using a high temperature series (HTS) expansion of the square-planar lattice for the Heisenberg model:

$$\chi_M = \frac{N_A g^2 \mu_B^2 S(S+1)}{3k_B T} \sum a_n (J/k_B T)^n \tag{3.2}$$

where $N_A$, $g$, $\mu_B$, $k_B$, and $J$ are the Avogadro constant, $g$ factor, Bohr magnetion, Bolzmann constant, and exchange integrals for the nearest neighbor Mn-Mn ions in the $ab$-plane, respectively, and $a_n$ (n = 1-8) are the coefficients given in previous results[28–31]. The fitting equation was obtained by applying the Padé approximation ([4, 4] Padé) to the equation

(2). We calculated *g* factor and *J* as fitting parameters. The calculation result is shown in Figure 6 as a solid blue line and it is in good agreement with the experimental data. The *g* factor of the $Mn^{2+}$ ion and the value of *J* are determined to be 1.92(1) and -0.34(1) K, respectively. The effective magnetic moment $\mu_{\text{eff}}$ and the Weiss constant $\theta$ were calculated to be 5.68 $\mu_B$ and -7.93K, respectively, from the equations $\mu_{\text{eff}} = g\sqrt{S(S+1)}$ and $q = \sum 2zJS(S+1)/3k_B$ where z = 4. These values are comparable to those estimated from the Curie-Weiss law (5.92 $\mu_B$ and -10.6 K). This fitting indicates that $Sr_2MnGe_2O_7$ shows a two dimensional behavior in spite of the shorter Mn-Mn distance along the *c*-axis (interlayer; 5.32 Å) compared with that in the *ab*-plane (intralayer; 5.86 Å) *i.e.* It is reasonable approximation to ignore the next nearest neighbor interaction. A comparable magnitude of the *J* value has been reported for the analogous compound $Ba_2MnGe_2O_7$ ($|J|$ = 0.323 K in *ab*-plane, $|J'|$ = 0.0012 K along the *c*-axis) from the inelastic neutron scattering measurements[9].

Figure 3.7(a) shows the temperature dependence of the specific heat for $Sr_2MnGe_2O_7$. The data show a λ-type anomaly at 4.4 K, indicating the occurrence of the long-range antiferromagnetic ordering of $Mn^{2+}$ ions. The magnetic entropy ($S_{\text{mag}}$) due to the magnetic ordering was calculated by using $S_{mag} = \int_0^T C_{mag}/TdT$, in which the magnetic specific heat ($C_{\text{mag}}$) was estimated by subtracting the lattice and electronic specific heat from the experimental specific heat of $Sr_2MnGe_2O_7$. For the lattice and electronic contributions, we used the specific heat of a nonmagnetic and isostructural compound $Sr_2ZnGe_2O_7$. The magnetic specific heat below 1.8 K was extrapolated by the relation $C_{\text{mag}} \propto T^3$ from the spin-wave model for an antiferromagnet[32]. The temperature dependence of the magnetic specific heat divided by temperature ($C_{\text{mag}}/T$) and magnetic entropy ($S_{\text{mag}}$) are plotted in Figure 3.7(b). The $S_{\text{mag}}$ value reaches 13.9 J $mol^{-1}$ $K^{-1}$ at 20 K, which is close to the theoretical value $R\ln(2S+1) = R\ln 6$ = 14.90 J $mol^{-1}$ $K^{-1}$ ($R$ : gas

constant). This result shows that the observed magnetic transition is due to the long-range antiferromagnetic ordering of the $Mn^{2+}$ ion in a high-spin configuration $S = 5/2$.

Figure 3.4 (b) is powder neutron diffraction profile measured at 2.5 K. The data show a number of low-angle peaks, which are associated with the antiferromagnetic transition found from the magnetic susceptibility and specific heat measurements. All theses reflections can be indexed using a propagation vector $\boldsymbol{k}$ = (0, 0, 1/2), i.e. the magnetic unit cell is represented as $a_{mag} = a$, $c_{mag} = 2c$. In order to determine all the possible magnetic structures compatible with the crystal symmetry ($P$-42$_1m$), the representational analysis was performed using the program *SARAh*[33]. For the $Mn^{2+}$ ions on the 2*a* site the decomposition of magnetic representation is

$$\Gamma = 1\Gamma_1^1 + 1\Gamma_2^1 + 0\Gamma_3^1 + 0\Gamma_4^1 + 2\Gamma_5^2 \tag{3.3}$$

The constraint from the Landau theory requires three possible magnetic structures (the representations $\Gamma_1$, $\Gamma_2$ and $\Gamma_5$), and basis vectors for these representations are listed in Table 7. The Mn site is divided into two magnetic sublattices, Mn1 (0, 0, 0), and Mn2 (1/2, 1/2, 0). The $\Gamma_1$ and $\Gamma_2$ represent the collinear antiferromagnetic structures along the *c*-axis, in which the Mn1 and Mn2 spins are antiparallel or parallels arrangements. On the other hand, the $\Gamma_5$ means non-collinear antiferromagnetic structures with orthogonal spin arrangements in the *ab*-plane. The best fit was only achieved by using a model including the representation $\Gamma_1$. The calculated profiles are plotted in Figure 3.4, and the magnetic structure is illustrated in Figure 3.12(a). The results of the Rietveld analysis are listed in Table 3.4. The ordered magnetic moment of the $Mn^{2+}$ ion is determined to be 3.99(5) $\mu_B$. The smaller value than the theoretical moment (5 $\mu_B$) expected from the high-spin $3d^5$ configuration is due to the fact that neutron diffraction measurements were performed just below $T_N$.

In this magnetic structure, the magnetic interaction of Mn ions in the *ab*-plane (next nearest neighbor) is antiferromagnetic and it is predominant, *i.e.,* thus 2D nature in the

temperature dependence of the magnetic susceptibility with the negative $J$ value. In addition, the magnetic interaction of Mn ions along the $c$-axis is also antiferromagnetic. $Sr_2MnGe_2O_7$ has the same magnetic structure as that of the $Ba_2MnGe_2O_7$. The difference between these two compounds is in the direction of ordered magnetic moment, parallel or perpendicular ($// c$ or $\perp c$)[9].

3.3.2.2 $Sr_2CoGe_2O_7$

Figure 3.8 shows the temperature dependence of the reciprocal magnetic susceptibility for $Sr_2CoGe_2O_7$. From the result of fitting the data above 100 K by using Eq. (3.1), the effective magnetic moment was determined to be 4.43(5) $\mu_B$/ Co. This value is somewhat larger than the spin only value (3.87 $\mu_B$) of $3d^7$ ion in a tetrahedral coordination ($S$ = 3/2), which may be due to the effect of orbital angular momentum[34]. Similar value (4.3 $\mu_B$) has been observed for the analogous melilite $Ba_2CoSi_2O_7$ (4.3 $\mu_B$) [7].The negative $\theta$ value (-18.1(6) K) indicates that the predominant magnetic interaction between $Co^{2+}$ ions is antiferromagnetic.

The ZFC and FC magnetic susceptibilities for $Sr_2CoGe_2O_7$ in the low temperature range are plotted in the inset of Figure 3.8. The data show two anomalies: the large divergence between ZFC and FC susceptibilities at 8.4 K and a cusp in the susceptibility *v.s.* temperature curve at 6.4 K, which indicates the existence of a small ferromagnetic moment. To study the ferromagnetic moment, the remnant magnetization measurements were performed. The field dependence of magnetization and the temperature dependence of the remnant magnetization are shown in Figure 3.9 and Figure 3.10, respectively. The remnant magnetization rapidly decreases at 6.7 K. Both data show that the remnant magnetization is very small (~ 0.001 $\mu_B$). This weak ferromagnetic component associated with the magnetic transition is due to the Dzyaloshinsky-Moriya interaction[10,15].

Figure 3.11(a) shows the temperature dependence of the specific heat. A $\lambda$-type anomaly is observed at 6.5 K, indicating the occurrence of the long-range

antiferromagnetic ordering of $Co^{2+}$ ions. By the same way as the case for $Sr_2MnGe_2O_7$, the magnetic entropy is obtained and it reaches 10.6 J $mol^{-1}$ $K^{-1}$ at 20 K, which is close to the theoretical value for $S = 3/2$ ion, *i.e.,* $R\ln(2S+1) = R\ln 4 = 11.52$ J $mol^{-1}$ $K^{-1}$ . This result shows that the observed magnetic transition is due to the antiferromagnetic ordering of the $Co^{2+}$ ion.

The neutron diffraction measurements were carried out at low temperatures (2.5 and 20 K). The data at 2.5 K show the magnetic Bragg reflections at lower angles. These reflections can be indexed using a propagation vector $\boldsymbol{k}$ = (0, 0, 0); *i.e.,* the magnetic cell is the same as the crystal one. From the representational analysis, the decomposition of magnetic representation is obtained:

$$\Gamma = 1\Gamma_1^1 + 1\Gamma_2^1 + 0\Gamma_3^1 + 0\Gamma_4^1 + 2\Gamma_5^2 \tag{3.4}$$

The basis vectors for each irreducible representation are shown in Table 3.8. The representations $\Gamma_1$ and $\Gamma_2$ represent the collinear antiferromagnetic and ferromagnetic structures along the *c*-axis, respectively. From the representation $\Gamma_5$, various magnetic structures can be led, in which all the magnetic moments lay on the *ab*-plane. We tried to explain the diffraction data by these models; finally, we have succeeded in determining the magnetic structure as the linear combination of basis vectors belonging to $\Gamma_5$. The calculated profiles are plotted in Figure 3.5, the magnetic structure is illustrated in Figure 3.12(b), and the results of the Rietveld analysis are shown in Table 3.5. In this magnetic structure, the magnetic moments of Co1 (0, 0, 0) and Co2 (1/2, 1/2, 0) sublattices adopt a parallel arrangement. The ordered magnetic moment for the $Co^{2+}$ ion is determined to be 2.81(5) $\mu_B$ at 2.5 K, which is in good agreement with the 3 $\mu_B$ expected from the $3d^7$ ion. The magnetic moments of $Co^{2+}$ ion lie in the *ab*-plane, but its exact directions could not be determined because the magnetic structure of $Sr_2CoGe_2O_7$ has a tetragonal symmetry as shown in Figure 3.12(b). The magnetic moments of $Mn^{2+}$ ions in the $Sr_2MnGe_2O_7$ are aligned along the *c*-axis, while the $Co^{2+}$ moments are confined in the *ab*-

plane of the $Sr_2CoGe_2O_7$. This result is mainly due to the anisotropic character of the $Co^{2+}$ ions compared with the isotropic $Mn^{2+}$.

## 3.4 Summary

We investigated synthesis, crystal structure and magnetic properties of $Sr_2MGe_2O_7$($M$ = Mn, Co). They crystallize in a tetragonal melilite-type structure with space group $P\text{-}42_1m$. The magnetic susceptibility and specific heat measurements for $Sr_2MnGe_2O_7$ and $Sr_2CoGe_2O_7$ showed that an antiferromagnetic transition is observed at 4.4 K and 6.5 K, respectively. Furthermore, the 2D-Heisenberg square lattice antiferromagnetic model can account for the magnetic susceptibility of $Sr_2MnGe_2O_7$. The magnetic structures for both compounds have been determined by neutron diffraction measurements. In $Sr_2MnGe_2O_7$, the magnetic moment of $Mn^{2+}$ is along the $c$-axis. On the other hand, the magnetic moment of $Co^{2+}$ in $Sr_2CoGe_2O_7$ is on the $ab$-plane.

## 3.5 Tables and figures

Table 3.1 Magnetic properties of melilite type oxides.

| SAMPLE | Space group | $T_c$(K) | Magnetic properties | ref |
|---|---|---|---|---|
| $Sr_2MnSi_2O_7$ | *P*-42$_1$*m* | 3.4 | antiferromagnet | 5 |
| $Ca_2CoSi_2O_7$ | *P*-42$_1$*m* | 5.7 | antiferromagnet | 6 |
| $Sr_2CoSi_2O_7$ | *P*-42$_1$*m* | ≈ 7 | antiferromagnet | 6 |
| $Ba_2CoSi_2O_7$ | *C*2/*c* | ≈ 5 | antiferromagnet | 6, 7 |
| $BaCo_2SiO_7$ | *C*2/*c* | 21 | antiferromagnet | 7 |
| $BaCu_2Si_2O_7$ | *Pnma* | 9.2 | Quasi-1D-AFM | 8 |
| $Sr_2MnGe_2O_7$ | *P*-42$_1$*m* | 4.4 | antiferromagnet, $k$ = (0, 0, 1/2) | This study |
| $Sr_2CoGe_2O_7$ | *P*-42$_1$*m* | 6.5 | antiferromagnet, $k$ = (0, 0, 0) | This study |
| $Ba_2MnGe_2O_7$ | *P*-42$_1$*m* | 4.66 | 2D-AFM, $k$ = (0, 0, 1/2) | 9 |
| $Ba_2CoGe_2O_7$ | *P*-42$_1$*m* | 6.7 | 2D-AFM, $k$ = (0, 0, 0), multiferroic behavior | 10-14 |
| $Ba_2CuGe_2O_7$ | *P*-42$_1$*m* | 3.26 | 2D-spiral AFM, incommensurate - commensurate transition | 15 |
| $Ln_2GeBe_2O_7$ | *P*-42$_1$*m* | | *Ln* =Y, La, Pr, Sm, Gd, Dy, paramagnet ($T$ > 5 K) | 16 |
| $Eu_2MgSi_2O_7$ | *P*-42$_1$*m* | | Paramagnet ($T$ > 1.8 K) | 5 |
| $Eu_2MnSi_2O_7$ | *P*-42$_1$*m* | 10.7 | Ferrimagnet | 5 |

Table 3.2 Structural parameters for $Sr_2MGe_2O_7$ ($M$ = Mn, Co, Zn) determined by the Rietveld analysis of the XRD data at room temperature.

| Atom | Site | x | y | z | B (Å$^2$) |
|---|---|---|---|---|---|
| | | $Sr_2MnGe_2O_7$ [a] | | | |
| Sr | 4*e* | 0.1666(1) | 0.6666 | 0.5064(2) | 1.08(4) |
| Mn | 2*a* | 0 | 0 | 0 | 0.55(7) |
| Ge | 4*e* | 0.6402(2) | 0.14020 | 0.9454(2) | 0.73(2) |
| O(1) | 2*c* | 0 | 1/2 | 0.1919(20) | 1.3(1) |
| O(2) | 4*e* | 0.6362(7) | 0.1362 | 0.2675(11) | 1.3 |
| O(3) | 8*f* | 0.0839(7) | 0.1871(7) | 0.2097(11) | 1.3 |
| | | $Sr_2CoGe_2O_7$ [b] | | | |
| Sr | 4*e* | 0.1650(1) | 0.6650 | 0.5072(3) | 1.22(4) |
| Co | 2*a* | 0 | 0 | 0 | 0.96(4) |
| Ge | 4*e* | 0.6423(2) | 0.14230 | 0.9522(3) | 0.94(4) |
| O(1) | 2*c* | 0 | 1/2 | 0.1833(21) | 1.2(1) |
| O(2) | 4*e* | 0.6383(7) | 0.1383 | 0.2742(12) | 1.2 |
| O(3) | 8*f* | 0.0858(7) | 0.1807(7) | 0.2021(11) | 1.2 |
| | | $Sr_2ZnGe_2O_7$ [c] | | | |
| Sr | 4*e* | 0.1658(1) | 0.66584 | 0.5062(3) | 0.89(3) |
| Zn | 2*a* | 0 | 0 | 0 | 0.62(5) |
| Ge | 4*e* | 0.6424(1) | 0.1424 | 0.9533(3) | 0.52(3) |
| O(1) | 2*c* | 0 | 1/2 | 0.1785(2) | 1.0(2) |
| O(2) | 4*e* | 0.6389(6) | 0.1389 | 0.2841(1) | 1.0 |
| O(3) | 8*f* | 0.0819(6) | 0.1798(6) | 0.2032(9) | 1.0 |

Note :

[a] Space group $P\text{-}42_1m$ (No. 113), $Z = 2$, $a = 8.2871(3)$ Å, $c = 5.3189(2)$ Å, $V = 365.28(2)$ Å$^3$, $R_{wp} = 8.95$ %, $R_p = 6.60$ %, $R_B = 2.26$ %, $R_F = 1.55$%.

[b] Space group $P\text{-}42_1m$ (No. 113), $Z = 2$, $a = 8.1694(2)$ Å, $c = 5.3253(1)$ Å, $V = 355.40(2)$ Å$^3$, $R_{wp} = 8.11$ %, $R_p = 6.54$ %, $R_B = 2.06$ %, $R_F = 1.55$ %.

[c] Space group $P\text{-}42_1m$ (No. 113), $Z = 2$, $a = 8.1528(2)$ Å, $c = 5.3267(1)$ Å, $V = 354.05(1)$ Å$^3$, $R_{wp} = 8.90$ %, $R_p = 6.23$ %, $R_B = 2.05$ %, $R_F = 1.15$ %.

Table 3.3 Structural parameters for the $Sr_2MnGe_2O_7$ which prepared in air condition expected by the Rietveld analysis of the XRD data at room temperature.

| Atom | Site | x | y | z | B ($Å^2$) |
|---|---|---|---|---|---|
| Sr | 4*e* | 0.1703(1) | 0.6703 | 0.5022(4) | 1.04(4) |
| Mn | 2*a* | 0 | 0 | 0 | 0.5(1) |
| Ge | 4*e* | 0.6403(2) | 0.1403 | 0.9686(4) | 1.0(1) |
| O(1) | 2*c* | 0 | 1/2 | 0.1523(30) | 1.0(1) |
| O(2) | 4*e* | 0.6349(8) | 0.1349 | 0.2867(15) | 1.0 |
| O(3) | 8*f* | 0.0858(8) | 0.1734(8) | 0.1754(14) | 1.0 |

Note:
Space group $P\text{-}42_1m$ (No. 113), $Z = 2$, $a = 8.0676(4$ Å, $c = 5.3891(2)$ Å, $V = 350.76(3)$ $Å^3$, $R_{wp} = 10.04$ %, $R_p = 7.77$ %, $R_B = 5.89$ %, $R_F = 3.02$%.

Table 3.4 Structural parameters for $Sr_2MnGe_2O_7$ by NPD data.

| Atom | Site | *x* | *Y* | *z* | *B* (Å$^2$) |
|---|---|---|---|---|---|
| 20 K[a] | | | | | |
| Sr | 4*e* | 0.1659(2) | 0.6660 | 0.50161(3) | 0.22(5) |
| Mn | 2*a* | 0 | 0 | 0 | 0.15(9) |
| Ge | 4*e* | 0.6408(1) | 0.1408 | 0.9427(4) | 0.24(5) |
| O(1) | 2*c* | 0 | 1/2 | 0.1860(7) | 0.24(5) |
| O(2) | 4*e* | 0.6387(2) | 0.1387 | 0.2674(5) | 0.34(6) |
| O(3) | 8*f* | 0.0800(2) | 0.1842(2) | 0.2167(4) | 0.29(5) |
| 2.5 K[b] | | | | | |
| Sr | 4*e* | 0.1656(2) | 0.6656 | 0.5062(4) | 0.29(4) |
| Mn | 2*a* | 0 | 0 | 0 | 0.21(10) |
| Ge | 4*e* | 0.6405(2) | 0.1405 | 0.9427(4) | 0.35(4) |
| O(1) | 2*c* | 0 | 1/2 | 0.1862(7) | 0.41(8) |
| O(2) | 4*e* | 0.6389(2) | 0.1389 | 0.2674(4) | 0.36(5) |
| O(3) | 8*f* | 0.0801(2) | 0.1844(2) | 0.2167(4) | 0.37(4) |

Note :

[a] Space group *P*-42$_1$*m* (No. 113), $Z = 2$, $a = 8.2833(26)$ Å, $c = 5.3096(16)$ Å, $V = 364.31(19)$ Å$^3$, $R_{wp} = 5.99$ %, $R_p = 4.34$ %, $R_B = 1.11$ %, $R_F = 0.46$%.

[b] Space group *P*-42$_1$*m* (No. 113), $Z = 2$, $a = 8.2838(1)$ Å, $c = 5.3100(1)$ Å, $V = 364.38(1)$ Å$^3$, $\mu_{Mn} = 3.99(5)\ \mu_B$, $R_{wp} = 5.84$ %, $R_p = 4.17$ %, $R_B = 1.12$ %, $R_F = 0.52$ %, $R_{mag\ B} = 2.13$ %, $R_{mag\ F} = 0.66$ %,

Table 3.5 Structural parameters for $Sr_2CoGe_2O_7$.

| Atom | Site | *x* | *y* | *z* | *B* (Å$^2$) |
|---|---|---|---|---|---|
| 20 K[a] | | | | | |
| Sr | 4*e* | 0.1653(1) | 0.6653 | 0.5065(3) | 0.24(4) |
| Co | 2*a* | 0 | 0 | 0 | 0.20(11) |
| Ge | 4*e* | 0.6425(1) | 0.1425 | 0.9496(2) | 0.29(4) |
| O(1) | 2*c* | 0 | 1/2 | 0.1818(5) | 0.27(6) |
| O(2) | 4*e* | 0.6384(2) | 0.1384 | 0.2738(3) | 0.37(5) |
| O(3) | 8*f* | 0.0818(2) | 0.1792(2) | 0.2094(3) | 0.39(4) |
| 2.5 K[b] | | | | | |
| Sr | 4*e* | 0.1653(1) | 0.6653 | 0.5069(2) | 0.20(3) |
| Co | 2*a* | 0 | 0 | 0 | 0.12(9) |
| Ge | 4*e* | 0.6424(1) | 0.1424 | 0.9494(2) | 0.29(3) |
| O(1) | 2*c* | 0 | 1/2 | 0.1818(5) | 0.29(6) |
| O(2) | 4*e* | 0.6384(2) | 0.1384 | 0.2737(3) | 0.39(4) |
| O(3) | 8*f* | 0.0816(2) | 0.1793(2) | 0.2095(3) | 0.43(4) |

Note :

[a] Space group *P*-42$_1$*m* (No. 113), $Z = 2$, $a = 8.1616(25)$ Å, $c = 5.3103(16)$ Å, $V = 353.72(18)$ Å$^3$, $R_{wp} = 4.64$ %, $R_p = 3.50$ %, $R_B = 0.84$ %, $R_F = 0.35$%.

[b] Space group *P*-42$_1$*m* (No. 113), $Z = 2$, $a = 8.1621(2)$ Å, $c = 5.3101(1)$ Å, $V = 353.76(1)$ Å$^3$, $\mu_{Mn} = 2.84(5)$ $\mu_B$ $R_{wp} = 4.15$ %, $R_p = 3.03$ %, $R_B = 0.75$ %, $R_F = 0.31$%, $R_{mag\ B} = 3.19$ %, $R_{mag\ F} = 0.45$%

Table 3.6 Selected interatomic distances (Å) and bond valence sums.

| | $Sr_2MnGe_2O_7$ | | $Sr_2CoGe_2O_7$ | | $Sr_2ZnGe_2O_7$ |
|---|---|---|---|---|---|
| | XRD (RT) | NPD (20 K) | XRD (RT) | NPD (20 K) | XRD (RT) |
| Sr-O(3)×2 | 2.561(6) | 2.572(3) | 2.558(4) | 2.559(1) | 2.568(6) |
| Sr-O(1) | 2.571(8) | 2.582(3) | 2.568(5) | 2.572(1) | 2.576(5) |
| Sr-O(2) | 2.589(5) | 2.615(3) | 2.589(5) | 2.580(2) | 2.589(6) |
| Sr-O(2)'×2 | 2.746(3) | 2.805(2) | 2.742(4) | 2.748(2) | 2.755(4) |
| Sr-O(3)'×2 | 2.903(6) | 2.838(2) | 2.904(1) | 2.857(1) | 2.875(5) |
| BVS ($Sr^{2+}$) | 1.72 | 1.73 | 1.78 | 1.82 | 1.77 |
| M-O3×4 | 2.033(6) | 2.023(2) | 1.957(6) | 1.954(1) | 1.941(5) |
| BVS ($M^{2+}$) | 2.08 | 2.13 | 1.95 | 1.96 | 2.10 |
| Ge-O2 | 1.714(6) | 1.724(3) | 1.715(7) | 1.722(2) | 1.708(5) |
| Ge-O3×2 | 1.717(6) | 1.752(2) | 1.726(6) | 1.753(1) | 1.742(5) |
| Ge-O1 | 1.798(4) | 1.786(3) | 1.796(5) | 1.786(2) | 1.786(4) |
| BVS ($Ge^{4+}$) | 4.15 | 3.94 | 4.10 | 3.94 | 4.042 |

Table 3.7 Basis function of the irreducible group representation of the space group $P\text{-}42_1m$ appearing in the magnetic representation with $\boldsymbol{k}$ = (0, 0, 1/2).

| Irreducible Group | Basis Vector | Mn(1)* | | | Mn(2)* | | |
|---|---|---|---|---|---|---|---|
| | | $m_x$ | $m_y$ | $m_z$ | $m_x$ | $m_y$ | $m_z$ |
| $\Gamma_1$ | $\Psi_1$ | 0 | 0 | 4 | 0 | 0 | -4 |
| $\Gamma_2$ | $\Psi_2$ | 0 | 0 | 4 | 0 | 0 | 4 |
| $\Gamma_5$ | $\Psi_3$ | 2 | 0 | 0 | 0 | -2 | 0 |
| | $\Psi_4$ | 0 | 2 | 0 | -2 | 0 | 0 |
| | $\Psi_5$ | 0 | -2 | 0 | -2 | 0 | 0 |
| | $\Psi_6$ | 2 | 0 | 0 | 0 | 2 | 0 |

Note : The atoms of the nonprimitive basis are defined as (0, 0, 0) for Mn(1) and (1/2, 1/2, 0) for Mn(2) in $Sr_2MnGe_2O_7$

Table 3.8 Basis function of the irreducible group representation of the space group $P\text{-}42_1m$ appearing in the magnetic representation with $\boldsymbol{k}$ = (0, 0, 0).

| Irreducible Group | Basis Vector | Co(1)* | | | Co(2)* | | |
|---|---|---|---|---|---|---|---|
| | | $m_x$ | $m_y$ | $m_z$ | $m_x$ | $m_y$ | $m_z$ |
| $\Gamma_1$ | $\Psi_1$ | 0 | 0 | 4 | 0 | 0 | -4 |
| $\Gamma_2$ | $\Psi_2$ | 0 | 0 | 4 | 0 | 0 | 4 |
| $\Gamma_5$ | $\Psi_3$ | 4 | 0 | 0 | 0 | 0 | 0 |
| | $\Psi_4$ | 0 | 0 | 0 | 0 | -4 | 0 |
| | $\Psi_5$ | 0 | 0 | 0 | -4 | 0 | 0 |
| | $\Psi_6$ | 0 | -4 | 0 | 0 | 0 | 0 |

Note : The atoms of the nonprimitive basis are defined as (0, 0, 0) for Co(1) and (1/2, 1/2, 0) for Co(2) in $Sr_2CoGe_2O_7$

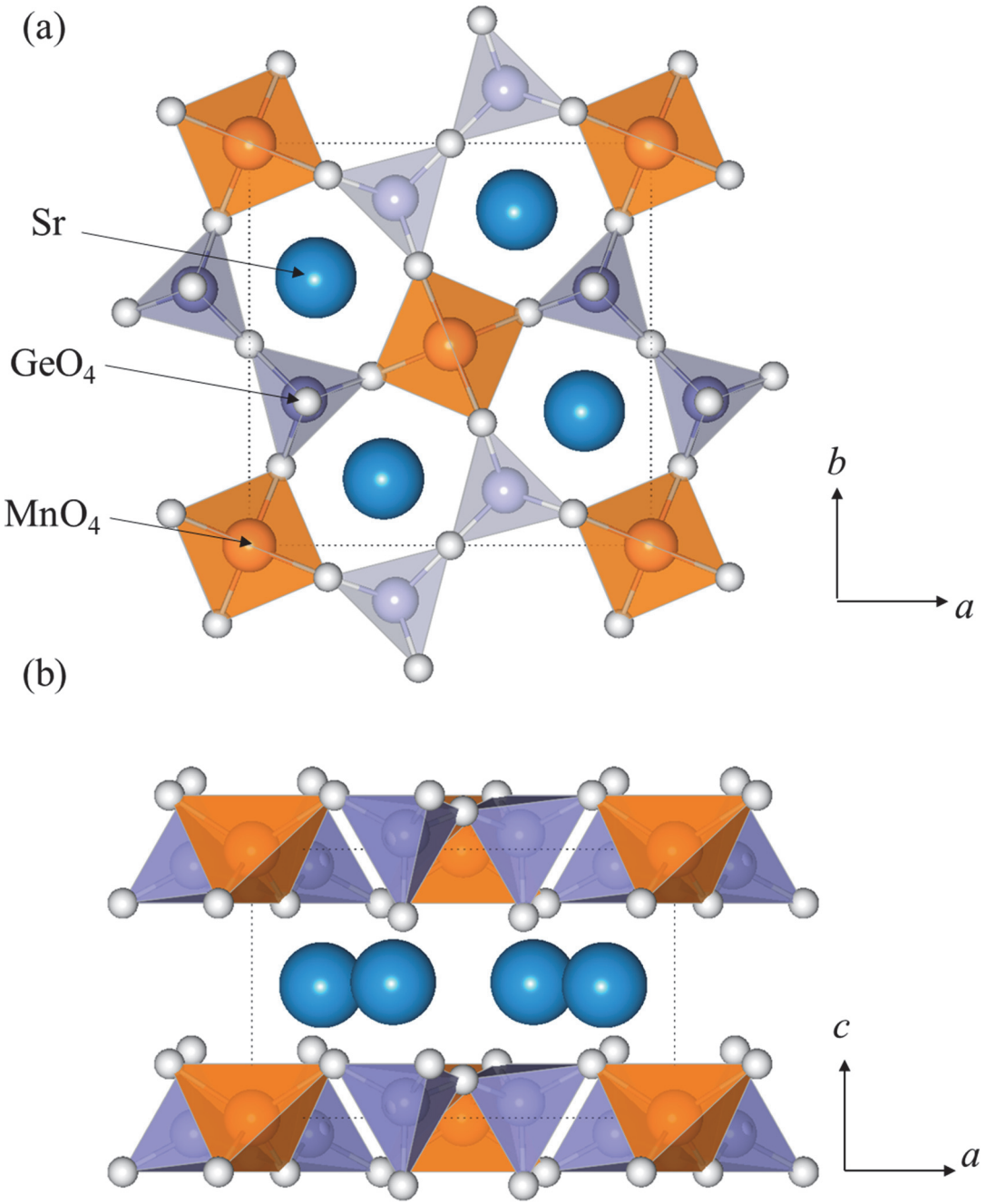


Figure 3.1 The schematic crystal structure of melilite-type oxides $Sr_2MGe_2O_7$ ($M$ = Mn, Co). (a) viewed from the $c$-axis, (b) projection of the structure in the $ab$-plane.

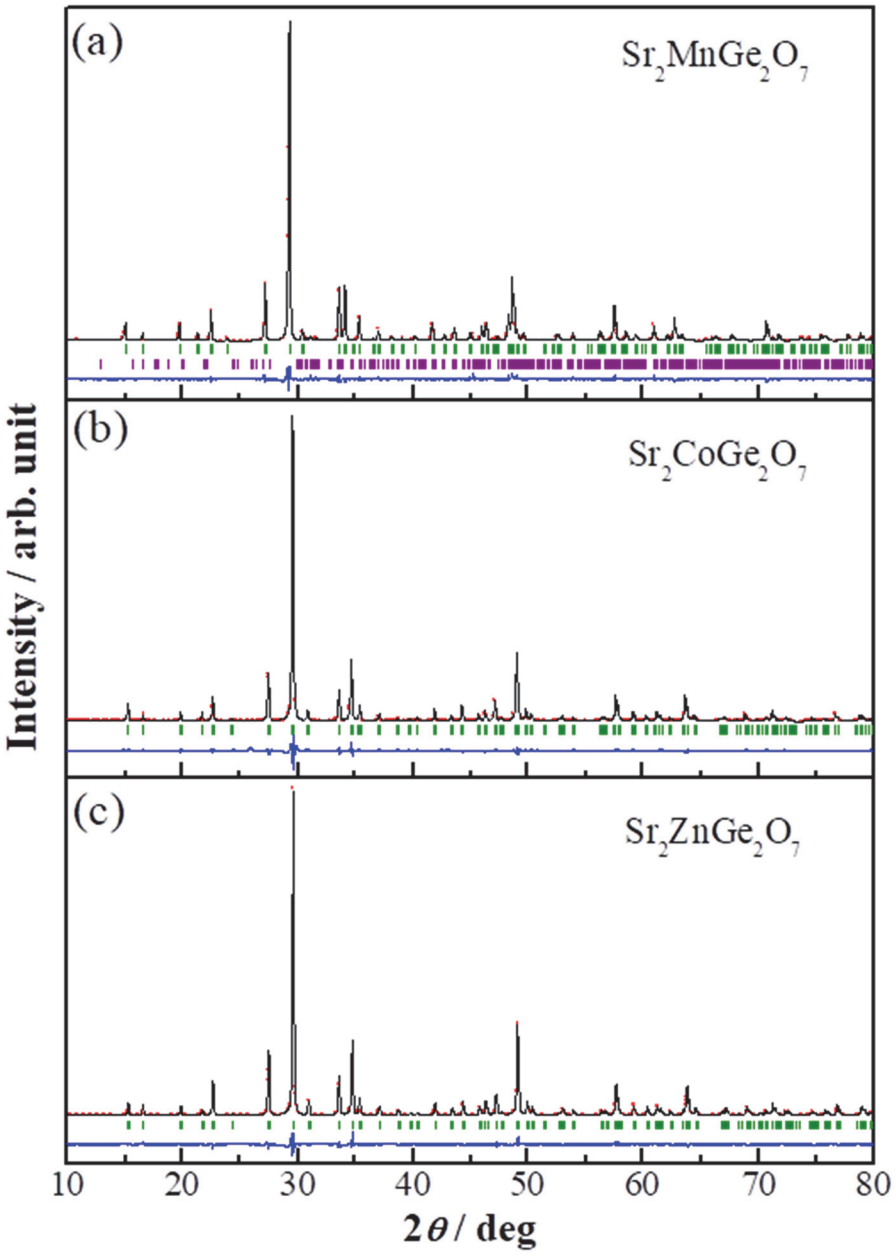


Figure 3.2 Powder X-ray diffraction profiles for (a) $Sr_2MnGe_2O_7$ and (b) $Sr_2CoGe_2O_7$. at room temperature. The calculated and observed profiles are shown on the top black solid line and red cross markers, respectively. The vertical marks in the middle show positions calculated for Bragg reflections. The lower trace is a plot of the difference between calculated and observed intensities. For (a), the second vertical marks show an impurity phase α-Sr2GeO4 (~ 1 %).

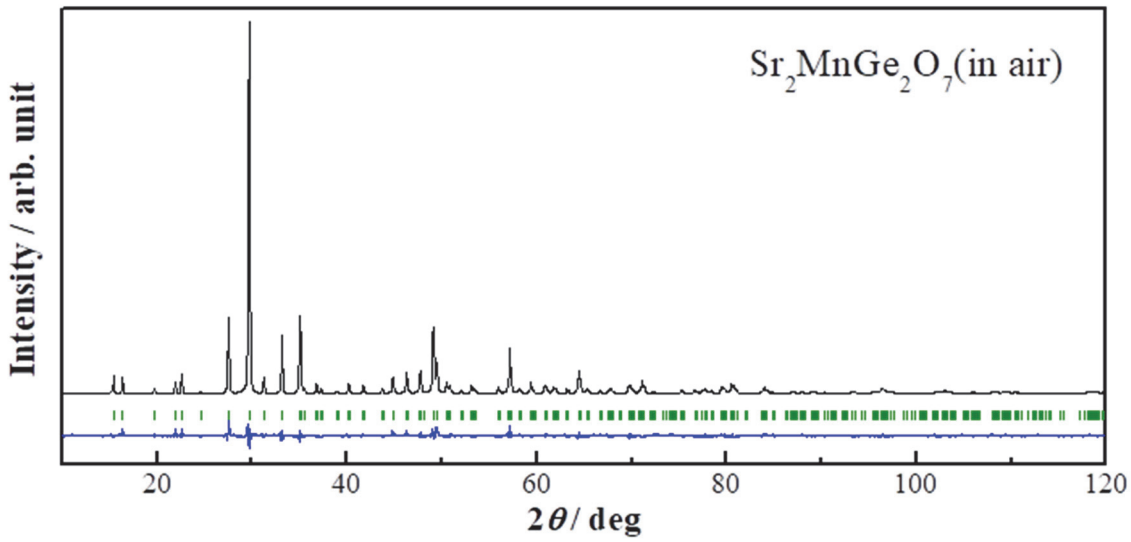


Figure 3.3 Powder X-ray diffraction profiles for $Sr_2MnGe_2O_7$ (in air) at room temperature.

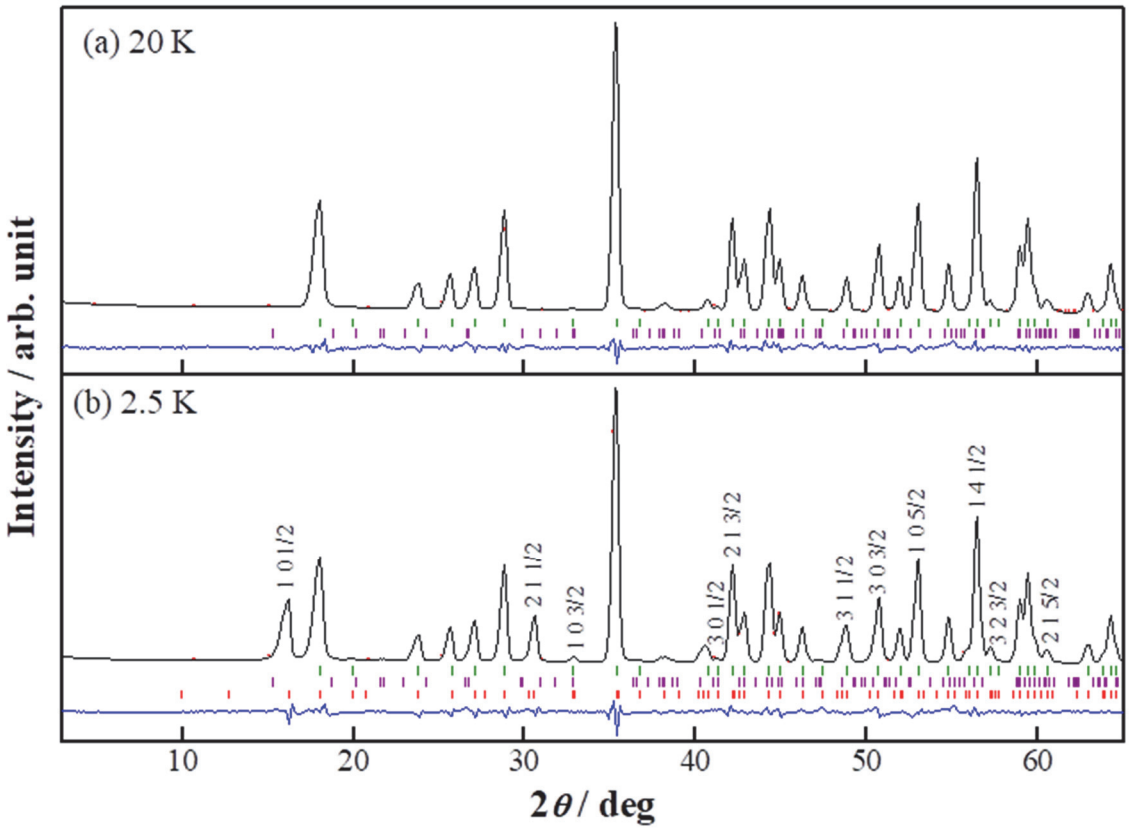


Figure 3.4 Powder neutron diffraction profiles for $Sr_2MnGe_2O_7$ at (a) 20 K and (b) 2.5 K. The calculated and observed profiles are shown on the top black solid line and red markers, respectively. In (a), the vertical marks in the middle show positions calculated for Bragg reflections of $Sr_2MnGe_2O_7$. The second vertical markers show positions for an impurity of $\alpha$-$Sr_2GeO_4$. In (b), the third vertical marks show the magnetic Bragg reflections for $Sr_2MnGe_2O_7$. The lower trace is a plot of the difference between calculated and observed intensities.

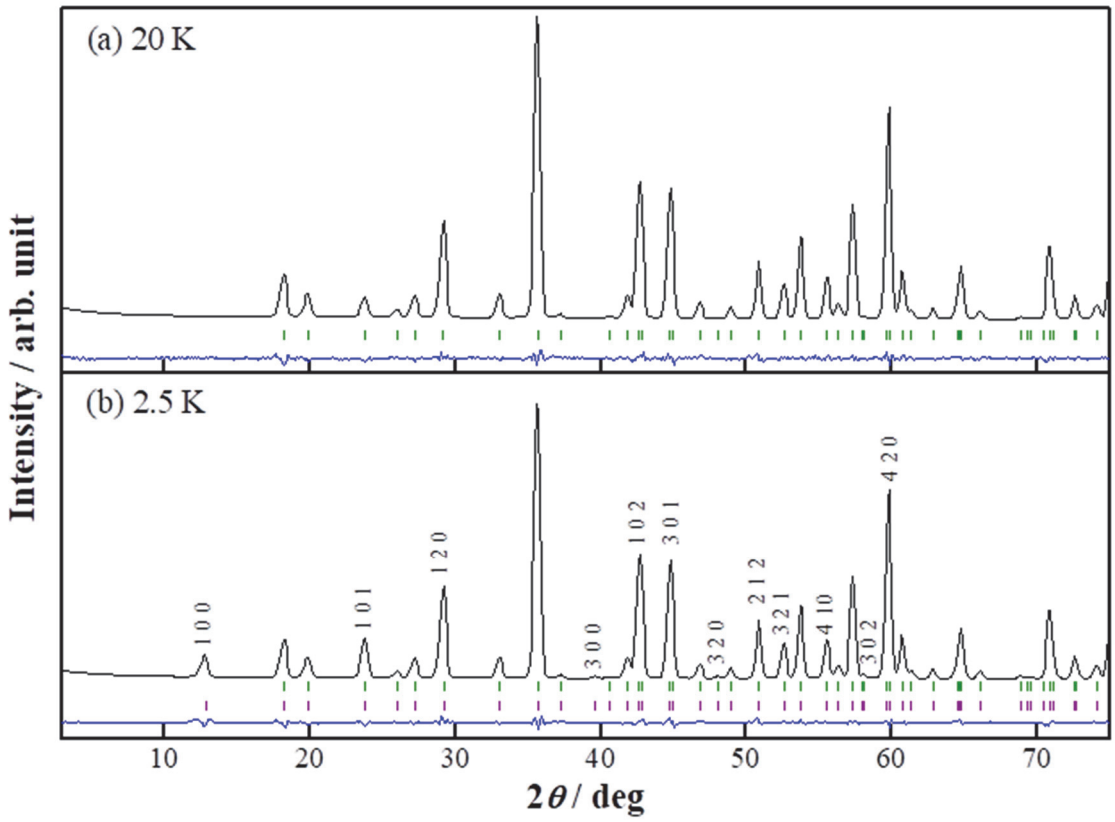


Figure 3.5 Powder neutron diffraction profiles for $Sr_2CoGe_2O_7$ at (a) 20 K, (b)2.5 K. The calculated and observed profiles are shown on the top black solid line and red cross markers, respectively. In (b), the second vertical marks show the magnetic Bragg reflections for $Sr_2CoGe_2O_7$. The lower trace is a plot of the difference between calculated and observed intensities.

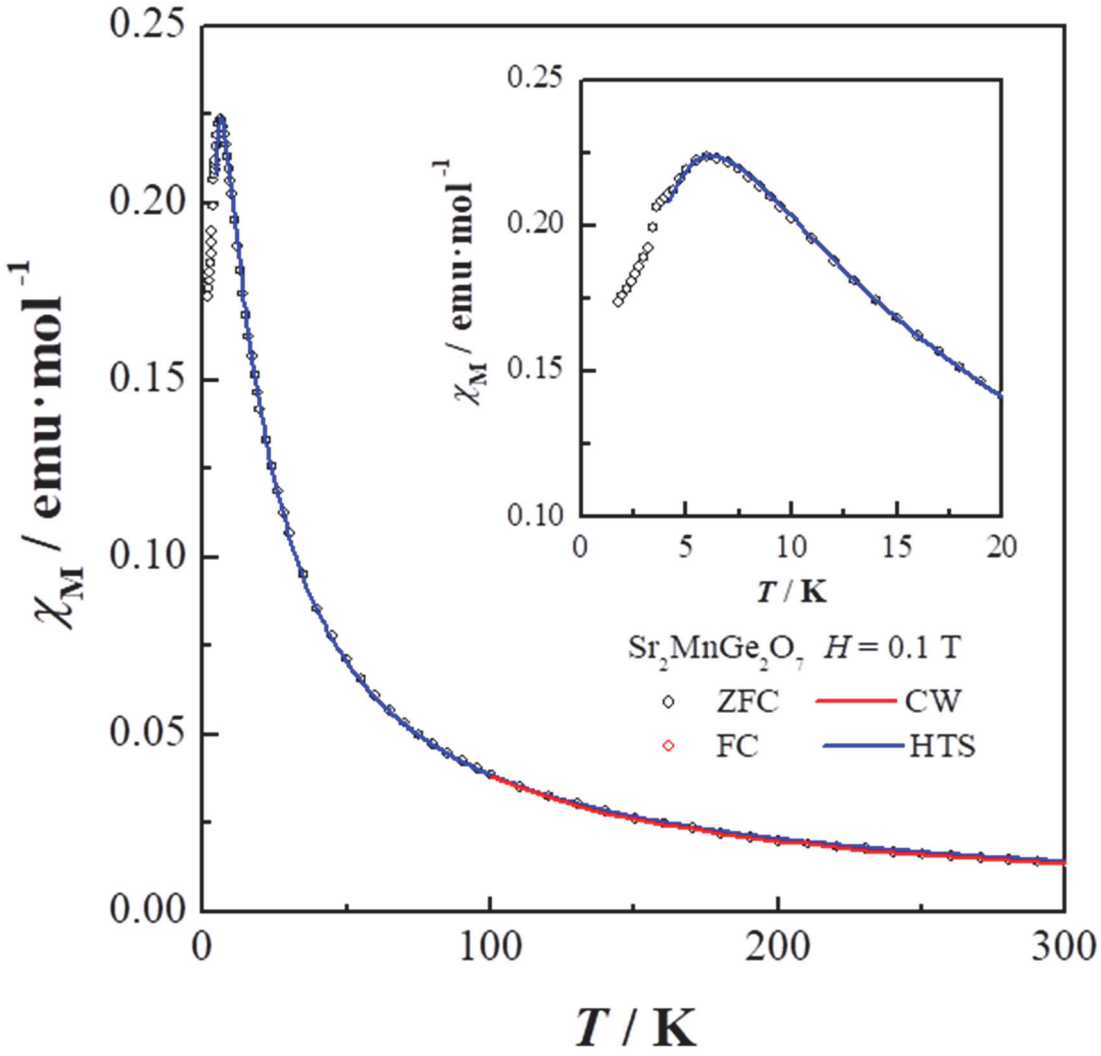


Figure 3.6 Temperature dependence of the magnetic susceptibility of $Sr_2MnGe_2O_7$. The red and blue solid line are fitting result by the Curie-Weiss law (CW), and the high temperature series (HTS) expansion for a square-planar lattice, respectively.

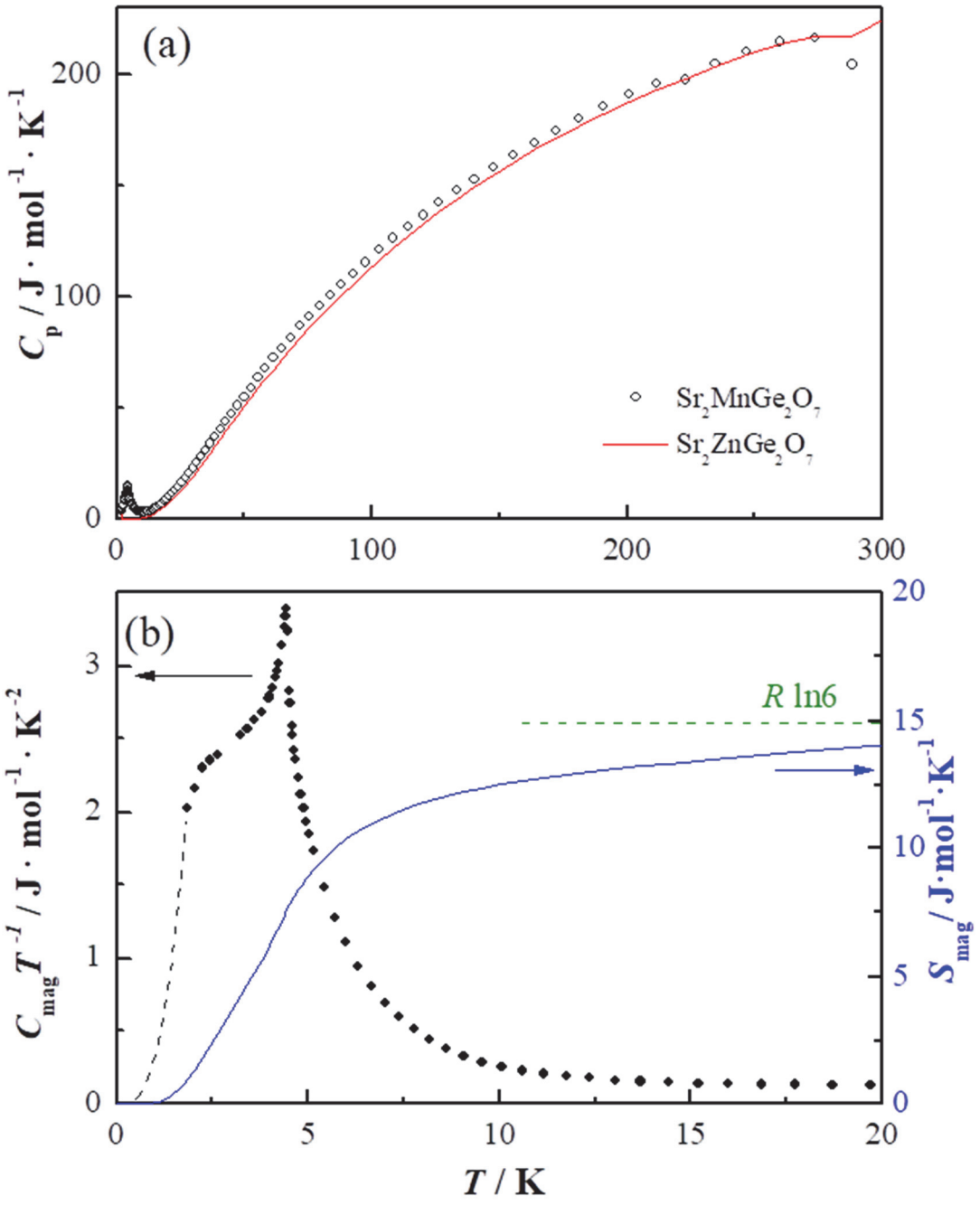


Figure 3.7 Temperature dependence of (a) specific heat ($C_P$), and (b) magnetic specific heat divided by temperature ($C_{mag}T^{-1}$) and magnetic entropy ($S_{mag}$) for $Sr_2MnGe_2O_7$.

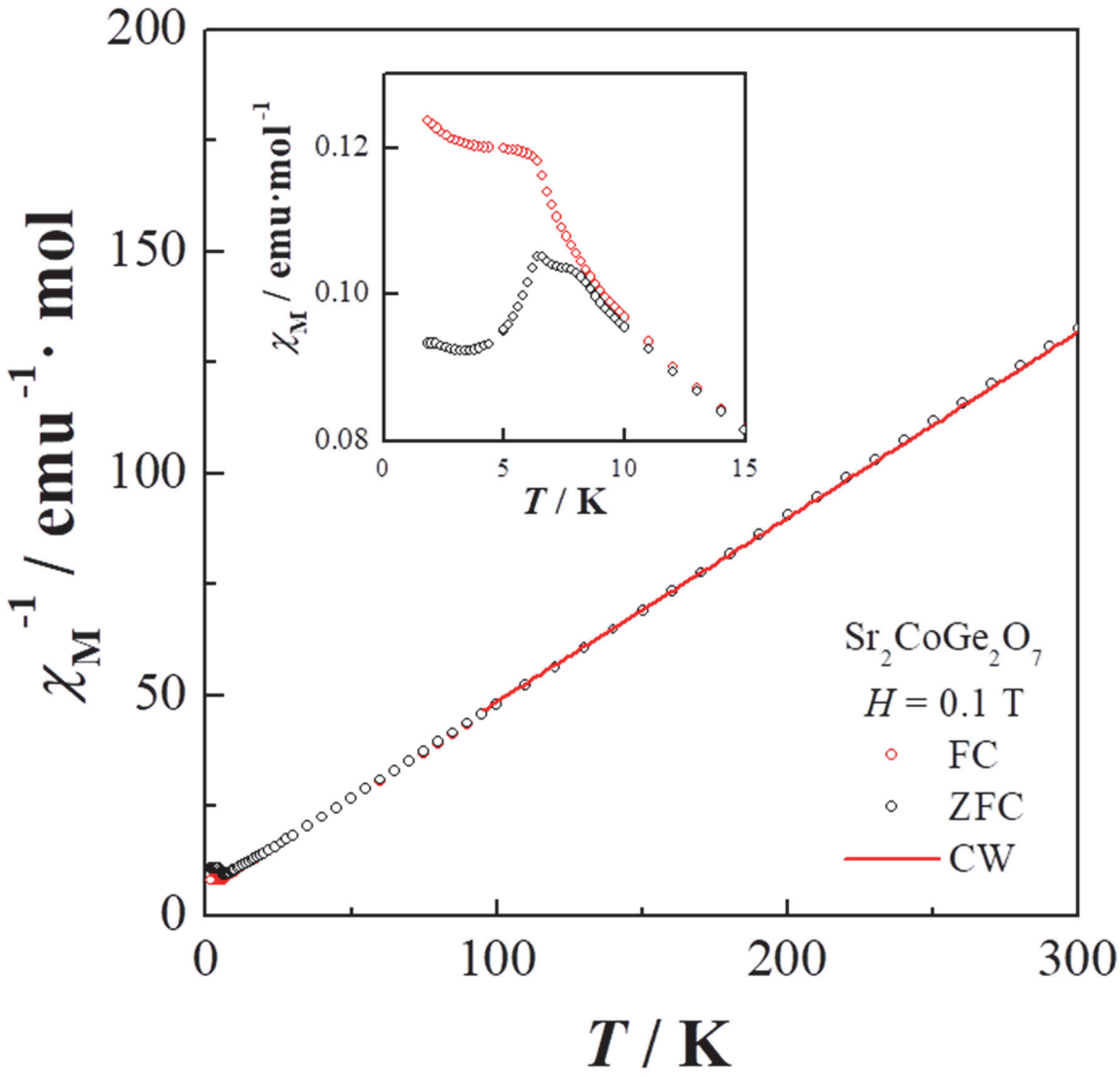


Figure 3.8 Temperature dependence of the reciprocal magnetic susceptibility of $Sr_2CoGe_2O_7$. The red solid line is a fitting result by the Curie-Weiss law (CW). The inset shows the susceptibility *v.s.* temperature curve at low temperatures.

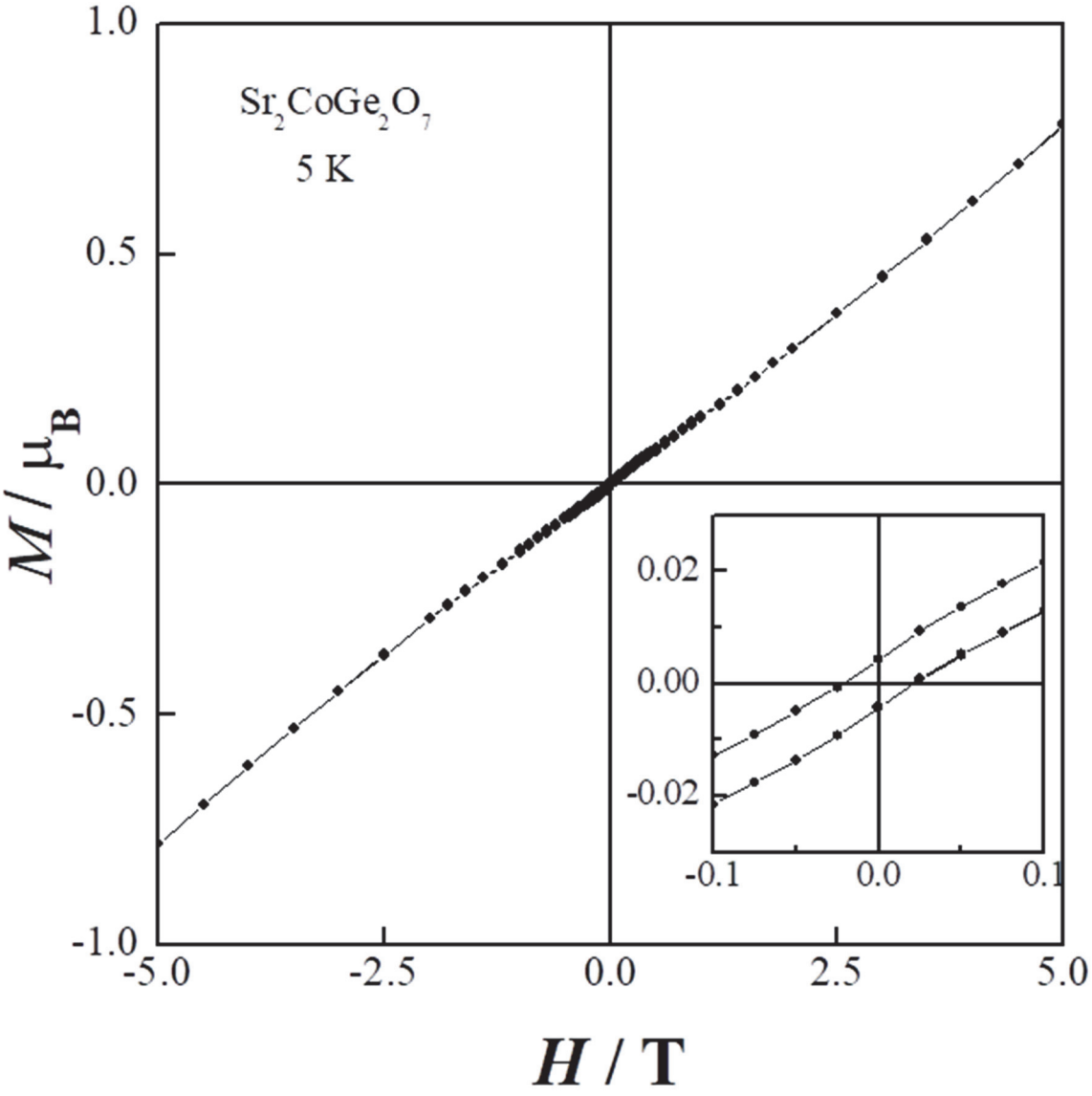


Figure 3.9 Field dependence of the magnetization for $Sr_2CoGe_2O_7$ at 5 K.

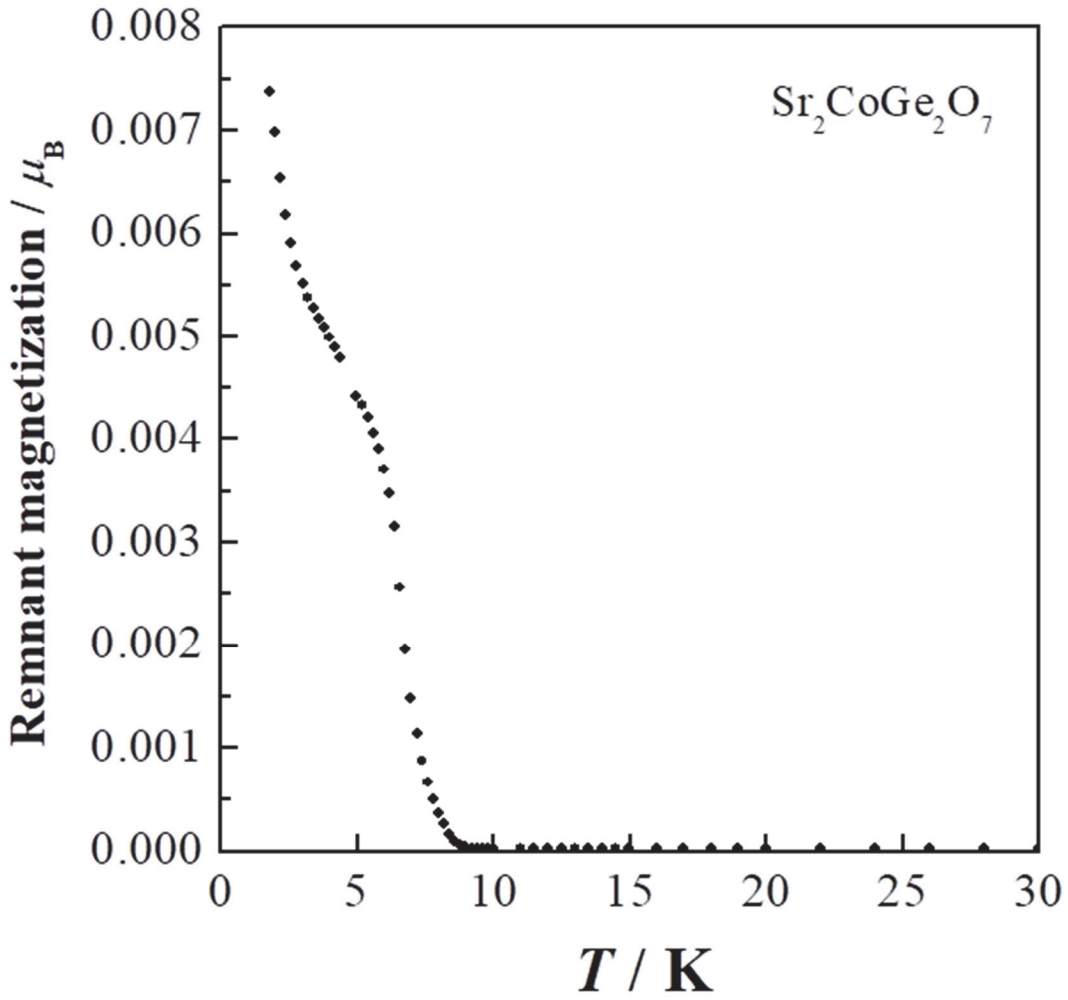


Figure 3.10 Temperature dependence of the remnant magnetization for $Sr_2CoGe_2O_7$.

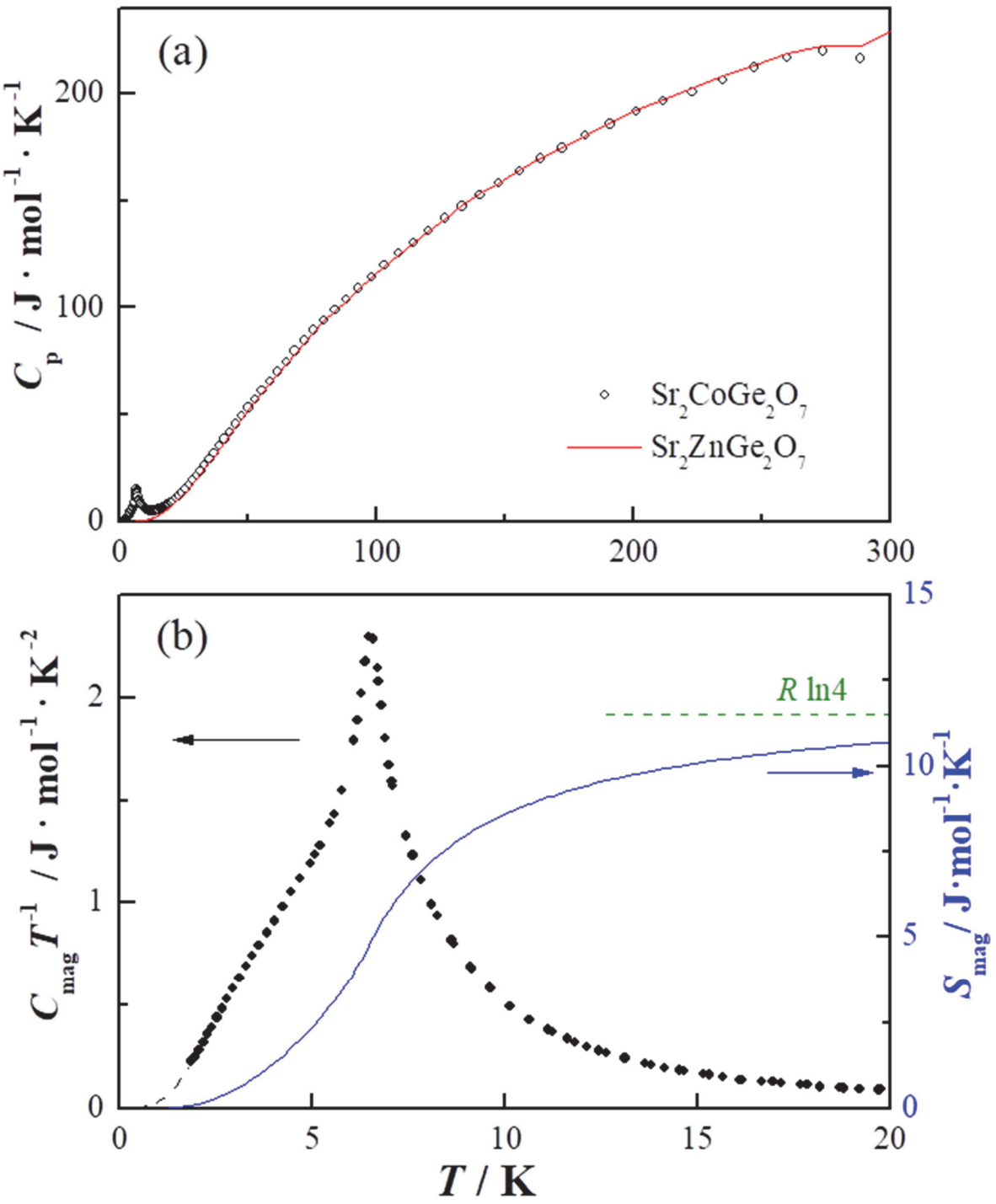


Figure 3.11 Temperature dependence of (a) specific heat ($C_P$), and (b) magnetic specific heat divided by temperature ($C_{mag}T^{-1}$) and magnetic entropy ($S_{mag}$) for $Sr_2CoGe_2O_7$.

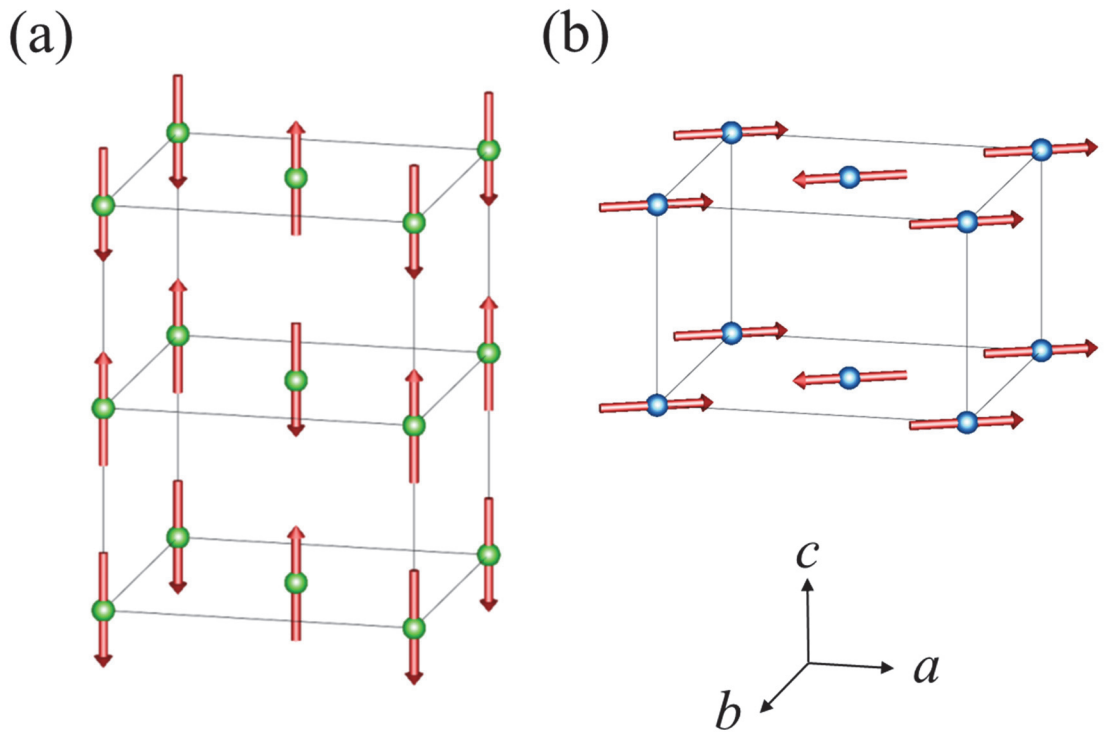


Figure 3.12 The magnetic structure of (a)$Sr_2MnGe_2O_7$ and (b)$Sr_2CoGe_2O_7$. Diamagnetic ions are omitted.

## 3.6 References

(1) De Joungh, L. J. *Magnetic Properties of Layered Transition Metal Compouds*; Kluwer, Ed.; Academic Publishers: Dordrecht, 1990.

(2) Burzo, E. *Melilites and Related Silicates in Landolt-Börnstein, New Series*; Springer: Berlin, 2005.

(3) Kaminskii, A. A.; Bohatý, L.; Becker, P.; Liebertz, J.; Held, P.; Eichler, H. J.; Rhee, H.; Hanuza, J. Tetragonal$Ba_2MgGe_2O_7$- a Novel Multifunctional Optical Crystal with Numerous Manifestations of Nonlinear-Laser Effects: Almost Sesqui-Octave Stokes and Anti-Stokes Combs and Cascaded $\chi$ (3) ↔ $\chi$ (2) Lasing with Involved Sec. *Laser Phys. Lett.* **2008**, *5*, 845–868.

(4) Mill, B. V.; Bailbakova, G. D. New Compounds with Melilite Structure: $Ln_2SiBe_2O_7$ (Ln = Nd-Eu, Tb, Ho-Lu) and $Ln_2GeBe_2O_7$ (Ln = Nd, Eu, Tb, Ho, Tm-Lu). *Russ. J. Inorg. Chem.* **1990**, *35*, 341–343.

(5) Endo, T.; Doi, Y.; Wakeshima, M.; Hinatsu, Y. Crystal Structures and Magnetic Properties of New Europium Melilites $Eu_2MSi_2O_7$ (*M* = Mg, Mn) and Their Strontium Analogues. *Inorg. Chem.* **2010**, *49*, 10809–10814.

(6) Akaki, M.; Tozawa, J.; Akahoshi, D.; Kuwahara, H. Magnetic and Dielectric Properties of $A_2CoSi_2O_7$( A =Ca, Sr, Ba) Crystals. *J. Phys. Conf. Ser.* **2009**, *150*, 042001.

(7) Adams, R. D.; Payen, C.; Datta, T. Syntheses, Structural Analyses, and Unusual Magnetic Properties of $Ba_2CoSi_2O_7$and $BaCo_2Si_2O_7$ . *Inorg. Chem.* **1996**, *35*, 3492–3497.

(8) Kenzelmann, M.; Zheludev, A.; Raymond, S.; Ressouche, E.; Masuda, T.; Böni, P.; Kakurai, K.; Tsukada, I.; Uchinokura, K.; Coldea, R. Spin Waves and Magnetic Ordering in the Quasi-One-Dimensional S=1/2 Antiferromagnet $BaCu_2Si_2O_7$. *Phys. Rev. B* **2001**, *64*, 054422.

(9) Masuda, T.; Kitaoka, S.; Takamizawa, S.; Metoki, N.; Kaneko, K.; Rule, K. C.; Kiefer, K.; Manaka, H.; Nojiri, H. Instability of Magnons in Two-Dimensional Antiferromagnets at High Magnetic Fields. *Phys. Rev. B* **2010**, *81*, 100402.

(10) Zheludev, A.; Sato, T.; Masuda, T.; Uchinokura, K.; Shirane, G.; Roessli, B. Spin Waves and the Origin of Commensurate Magnetism in $Ba_2CoGe_2O_7$. *Phys. Rev. B* **2003**, *68*, 024428.

(11) Sato, T.; Masuda, T.; Uchinokura, K. Magnetic Property of $Ba_2CoGe_2O_7$. *Phys. B Condens. Matter* **2003**, *329–333*, 880–881.

(12) Yi, H. T.; Choi, Y. J.; Lee, S.; Cheong, S.-W. Multiferroicity in the Square-Lattice Antiferromagnet of $Ba_2CoGe_2O_7$. *Appl. Phys. Lett.* **2008**, *92*, 212904.

(13) Murakawa, H.; Onose, Y.; Miyahara, S.; Furukawa, N.; Tokura, Y. Ferroelectricity Induced by Spin-Dependent Metal-Ligand Hybridization in $Ba_2CoGe_2O_7$. *Phys. Rev. Lett.* **2010**, *105*, 137202.

(14) Kézsmárki, I.; Kida, N.; Murakawa, H.; Bordács, S.; Onose, Y.; Tokura, Y. Enhanced Directional Dichroism of Terahertz Light in Resonance with Magnetic Excitations of the Multiferroic $Ba_2CoGe_2O_7$. *Phys. Rev. Lett.* **2011**, *106*, 057403.

(15) Zheludev, A.; Maslov, S.; Shirane, G.; Sasago, Y.; Koide, N.; Uchinokura, K. Field-Induced Commensurate-Incommensurate Phase Transition in a Dzyaloshinskii-Moriya Spiral Antiferromagnet. *Phys. Rev. Lett.* **1997**, *78*, 4857–4860.

(16) Ochi, Y.; Morikawa, H.; Marumo, F.; Nozaki, H. Structures and Magnetic Properties of Rare Earth Compounds in the Melilite Group. *Yogyo Kyokaishi* **1983**, *91*, 229–235.

(17) Petrakovskii, G. A.; Bezmaternykh, L. N.; Gudim, I. A.; Sheptyakov, D.; Bayukov, O. A.; Vorotynov, A. M.; Velikanov, D. A.; Bovina, A. F. Synthesis and Properties of Barium Ferrigermanate $Ba_2Fe_2GeO_7$. *Phys. Solid State* **2005**, *47*, 2114–2118.

(18) Petrakovskiĭ, G. A.; Bezmaternykh, L. N.; Gudim, I. A.; Bayukov, O. A.; Vorotynov, A. M.; Bovina, A. F.; Szymczak, R.; Baran, M.; Ritter, C. Spin Glass State in Crystals of Barium Ferrigermanate $Ba_2Fe_2GeO_7$. *Phys. Solid State* **2006**, *48*, 1906–1908.

(19) Naruse, H.; Tanaka, K.; Morikawa, H.; Marumo, F. Synthesis and Crystal Structure of Strontium Manganese Germanate ($Sr_2MnGe_2O_7$). *Rep.Res.Lab. Eng. Mater., Tokyo Inst. Technol.* **1984**, *9*, 1–9.

(20) Ohoyama, K.; Kanouchi, T.; Nemoto, K.; Ohashi, M.; Kajitani, T.; Yamaguchi, Y. The New Neutron Powder Diffractometer with a Multi-Detector System for High-Efficiency and High-Resolution Measurements. *Jpn. J. Appl. Phys.* **1998**, *37*, 3319.

(21) Izumi, F.; Momma, K. Three-Dimensional Visualization in Powder Diffraction. *Solid State Phenom.* **2007**, *130*, 15–20.

(22) Momma, K.; Izumi, F. VESTA : A Three-Dimensional Visualization System for Electronic and Structural Analysis. *J. Appl. Crystallogr.* **2008**, *41*, 653–658.

(23) Nishi, F. .; Takeuchi, Y. Structure of a High Temperature Modification of $Sr_2GeO_4$. *Eur. Crystallogr. Meet.* **1991**, *13*, 197.

(24) Ochi, Y.; Tanaka, K.; Morikawa, H.; Marumo, F. The Crystal Structure of $Sr_2ZnGe_2O_7$. *J. Miner. Soc. Japan* **1982**, *15*, 331–341.

(25) Brown, I. D.; Altermatt, D. Bond-Valence Parameters Obtained from a Systematic Analysis of the Inorganic Crystal Structure Database. *Acta Crystallogr. Sect. B Struct. Sci.* **1985**, *41*, 244–247.

(26) Brese, N. E.; O'Keeffe, M. Bond-Valence Parameters for Solids. *Acta Crystallogr. Sect. B Struct. Sci.* **1991**, *47*, 192–197.

(27) Carlin, R. L. *Magnetochemistry*; Springer-Verlang: Berlin, 1986.

(28) Rushbrooke, G. S.; Wood, P. . On High Temperature Expansions for the Heisenberg Model. *J. Proc. Phys. Soc., London* **1955**, *68*, 1161–1169.

(29) Rushbrooke, G. S.; Wood, P. J. On the Curie Points and High Temperature Susceptibilities of Heisenberg Model Ferromagnetics. *Mol. Phys.* **1958**, *1*, 257–283.

(30) Stephenson, R. L.; Pirnie, K.; Wood, P. J.; Eve, J. On the High Temperature Susceptibility and Specific Heat of the Heisenberg Ferromagnet for General Spin. *Phys. Lett. A* **1968**, *27*, 2–3.

(31) Yamaji, K.; Konda, J. On the High-Temperature Susceptibilities of the Two-Dimensional Ferromagnetic Heisenberg Spin Systems. *J. Phys. Soc. Japan* **1973**, *35*, 25–32.

(32) Joshua, S. J.; Cracknell, A. P. The Spin-Wave Contribution to the Specific Heat of $NiF_2$. *Phys. Lett. A* **1969**, *28*, 562–563.

(33) Wills, A. S. A New Protocol for the Determination of Magnetic Structures Using Simulated Annealing and Representational Analysis (SARAh). *Phys. B Condens. Matter* **2000**, *276–278*, 680–681.

(34) Carlin, R. L. *Transition Metal Chemistry*; Marcel Dekker, Inc.: New York, 1965.

# Chapter 4

# Crystal Structures and Magnetic Properties of New Europium Melilites $Eu_2MSi_2O_7$ ($M$ = Mg, Mn) and Their Strontium Analogues

## 4.1 Introduction

The melilite-type oxides have the general formula $A_2MM'_2O_7$ ($A$ = larger cations such as alkali earth ions and lanthanides; $M$, $M'$ = smaller divalent to tetravalent cations). Many of them crystallize in a tetragonal structure with space group $P\text{-}42_1m$, and this structure can be described as the two-dimensional network consisting of $MO_4$ and $M'O_4$ tetrahedra in the $ab$-plane and larger $A$ ions locate between these networks[1–3]. From this structural feature, magnetic properties of $A_2MM'_2O_7$ compounds ($A$ = Ca, Sr, Ba; $M$ = Mn, Co, Cu; $M'$ = Si, Ge) have been attracted interest. They show anomalous behaviors derived from the two-dimensional arrangement of magnetic $M$ ions. For example, $Ba_2MnGe_2O_7$ behaves as a square lattice Heisenberg antiferromagnet ($T_N$ = 4.0 K)[4], and $Ba_2CuGe_2O_7$ has a spiral spin structure below 3.26 K[5]. Two compounds $A_2CoSi_2O_7$ ($A$ = Ca, Sr) show both antiferromagnetic and dielectric anomalies, and are regarded as new candidates for multiferroic materials[6]. On the other hand, the melilite-type oxides in which the magnetic ion fully occupy the A site are very few. Among them, $A_2GeBe_2O_7$ ($A$ = Pr, Sm, Gd, Dy and Er) are paramagnetic down to 5 K[3,7].

In order to explore furthermore interesting materials, we have paid our attention to the melilites containing magnetic ions in both $A$ (= lanthanides) and $M$ (= transition metals) sites. Such compounds are expected to show magnetic behavior, reflecting both

$d$ - $d$ interactions and $f$ - $d$ interactions. To our best knowledge, however, no investigations were carried out.

In this study, we investigated the syntheses, crystal structures, and magnetic properties of new Eu-containing melilites $Eu_2MSi_2O_7$ ($M$ = Mg, Mn). Because the ionic radius of $Eu^{2+}$ is very close to that of $Sr^{2+}$, it should be possible to prepare such compounds. The results of the powder X-ray diffraction, $^{151}$Mössbauer spectrum, magnetic susceptibility, and specific heat measurements are discussed.

## 4.2 Experimental procedures

### 4.2.1 Synthesis

Polycrystalline samples (0.5 g) of $A_2MSi_2O_7$($A$ = Sr, Eu; $M$ = Mg, Mn) were prepared by the standard solid-state reaction. For starting materials, SrO, $Eu_2O_3$, MgO, MnO, $SiO_2$ and Si were used. Before use, $Eu_2O_3$ and MgO were heated at 900ºC overnight. The SrO was prepared by the decarbonation of $SrCO_3$ at 1400ºC for 12 h. These starting materials were weighed out in a stoichiometric ratio and well mixed in an agate mortar. The mixtures were pressed into pellets and wrapped in a molybdenum foil, and then they were sealed in evacuated quartz tubes. These ampoules were heated at 1100ºC for 36 - 48 h.

### 4.2.2 X-ray diffraction analysis

Powder X-ray diffraction (XRD) measurements were performed at room temperature using a Multi-Flex diffractometer (Rigaku) with a Cu Kα X-ray radiation source equipped with a curved graphite-monochromator. The data were collected by step-

scanning in the angle range of $10^{o} \leq 2\theta \leq 120^{o}$ at a step size 0.02º. The XRD data were analyzed by the Rietveld method using the program RIETAN-FP[8], and the crystal structures were drawn by VESTA program[9].

### 4.2.3 $^{151}$Eu Mössbauer spectroscopy measurements

The $^{151}$Eu Mössbauer spectra were measured at room temperature with a Mössbauer VT - 6000 transmission spectrometer (Laboratory Equipment) using a radiation source $^{151}SmF_3$(1.85 GBq). The spectrometer was calibrated with α-iron at room temperature, and the isomer shift (I.S.) was determined relative to the shift of europium trifluoride ($EuF_3$). The γ-ray was detected by a NaI scintillation counter. The powdered sample was wrapped in an aluminum foil (1.5 cm × 1.5 cm) with the density of 15 mg (Eu)/cm$^2$.

### 4.2.4 Magnetic measurements

The temperature dependence of the magnetic susceptibilities were measured with a SQUID magnetometer (Quantum Design, MPMS-5S). The measurements were performed under both zero-field-cooled (ZFC) and field-cooled (FC) conditions over the temperature range 1.8 - 300 K in an applied magnetic field of 0.1 T. The field dependence of the magnetizations was measured with a commercial physical property measurement system (Quantum Design, PPMS) over the magnetic field rage between -9 and 9 T at 1.8 K.

### 4.2.5 Specific heat measurements

The specific heat measurements were performed using a relaxation technique with the PPMS in the temperature range of 1.8 - 300 K. The pelletized sample was mounted on a thin alumina plate with Apiezon N-grease for better thermal contact.

### 4.2.6 Calculation of the quadrupole coupling constant

The calculation of the quadrupole coupling constant was carried out by the WIEN2k program using the full potential linearized augmented plane wave + local orbitals (FP-LAPW + lo) method based on the density functional theory (DFT) with the generalized gradient approximation (GAA)[10].

## 4.3 Results and discussion

### 4.3.1 Crystal structure

The melilite-type oxides $Sr_2MSi_2O_7$ ($M$ = Mg, Mn) and their new analogues $Eu_2MSi_2O_7$ ($M$ = Mg, Mn) were successfully prepared. They were obtained as white ($A$ = Sr) or light-green (Eu) colored polycrystalline samples. The trial to synthesize other $Eu_2MSi_2O_7$ compounds ($M$ = Fe, Co, Ni, Cu) was ended in failure, because the $M^{2+}$ ion was reduced to the metal by the introduction of the $Eu^{2+}$ ion (the major products were $M$ metal and apatite-type oxides $Eu_5Si_3O_{13}$).

The XRD profiles for $A_2MnSi_2O_7$ and $A_2MgSi_2O_7$ ($A$ = Sr, Eu) are shown in Figure 4.1 and Figure 4.2. The observed peaks were indexed on a tetragonal unit cell ($a \sim 8$Å, $c \sim 5$Å) with the space group $P\text{-}42_1m$, which is typical for the melilite-type

compounds[1-2]. Among the compounds prepared in this study, only the $Sr_2MnSi_2O_7$ contains a small amount of $SrSiO_3$ (~ 1%) as an impurity. The XRD data were analyzed by the Rietveld method using the structural parameters of $Sr_2MgSi_2O_7$ as a starting model[11]. The calculated profiles are also plotted in Figure 4.1 and Figure 4.2. The refined structural parameters and reliability factors are summarized in Table 4.1 and Table 4.2.

The schematic crystal structure of the title compounds is illustrated in Figure 4.3 and some selected interatomic distances of *A*-O, *M*-O and Si-O are listed in Table 4.3. In this structure, both the *M* and Si ions are coordinated by four oxygen ions, forming $MO_4$ and $SiO_4$ tetrahedra, respectively. These $MO_4$ and $SiO_4$ tetrahedra are linked by sharing corner-oxygen ions, and thus they build a two-dimensional layer consisted of five-membered rings in the *ab*-plane. Beneath these rings, the *A* ions locate in the eight-coordinated sites, forming another layer. These two kinds of layers are alternately stacked along the *c*-axis. In the $AO_8$ polyhedron, there are six kinds of *A*-O distances between 2.54 Å and 2.83 Å, and its shape is highly distorted. Reflecting almost the same ionic radii between $Sr^{2+}$ (1.26 Å) and $Eu^{2+}$ (1.25 Å)[12], these six distances are very close among four compounds in Table 3. The bond valence sums (BVS) are calculated from the interatomic distances, and they are also listed in Table 4.3[13,14]. These values indicate that the *A* and *M* ions are in the divalent state and the Si ion is in the tetravalent state.

### 4.3.2 $^{151}$Eu Mössbauer spectrum

Figure 4.4 shows the $^{151}$Eu Mössbauer spectra for $Eu_2MgSi_2O_7$ and $Eu_2MnSi_2O_7$ at room temperature. In both spectra, an absorption peak appears at *ca.*-13 mm / s, indicating the presence of the divalent Eu ions. On the other hand, no absorption peak was observed at 0.5 ~ 1 mm / s corresponding to the trivalent Eu ion[15]. Therefore, the Eu ions in both compounds are in the divalent state. The observed peak is strongly

asymmetric because of the quadrupole interaction. The quadrupole Hamiltonian is given by

$$H_Q = \frac{e^2qQ}{4I(2I-1)}\left(3I_z^2 - I(I+1) + \eta\left(I_x^2 + I_y^2\right)\right) \qquad (4.1)$$

where $I$ is the nuclear spin, $Q$ is the quadrupole moment, $eq = V_{ZZ}$, and $\eta = (V_{XX} - V_{YY}) / V_{ZZ}$ ($V_{ii}$ is the electric field gradient tensor). The 12 possible transitions (eight allowed transitions and four forbidden transitions) due to a quadrupole interaction were taken into account; the observed data were fitted with the sum of these Lorenzian lines. In order to derive these Lorenzian equations, the results by Shenoy and Dunlap were used and the ratio of the excited and ground state quadrupole moments ($R_Q = Q_e / Q_g$) was taken as 1.312[16,17]. The fitting curves are shown in Figure 4.4 and determined fitting parameters are listed in Table 4.4.

The large Q.S.(-13 ~ -15 mm/s) and non-zero $\eta$ (~ 0.3) values indicate that the Eu ion is in a greatly distorted coordination environment in these compounds. In fact, this ion is located in the distorted $EuO_8$ polyhedron with various Eu-O lengths Table 4.3. The Q.S. and $\eta$ values are also calculated by the electronic structure calculation using the structural parameters for $Eu_2MgSi_2O_7$. They ($Q.S._{cal}$ = -11.1 mm / s, $\eta_{cal}$ = 0.46) are in good agreement with the experimental data, which corresponds to the observed ones. Such a large Q.S. value has been found in $EuZrO_3$ perovskite containing divalent Eu ion (Q.S. = -12.64 mm / s and $\eta$ = 0.46)[18].

## 4.3.3 Magnetic properties

### 4.3.3.1 $Sr_2MnSi_2O_7$

Figure 4.5 shows the temperature dependence of the reciprocal magnetic susceptibility for $Sr_2MnSi_2O_7$. The data were fitted by the Curie-Weiss law between 100 and 300 K, using an equation

$$\chi_M = \frac{C}{(T-\theta)} + \chi_{TIP}, \tag{4.2}$$

where $C$, $\theta$, and $\chi_{TIP}$ mean the Curie constant, Weiss constant, and temperature independent paramagnetic susceptibility, respectively. The effective magnetic moment ($\mu_{eff}$) and Weiss constant were determined to be 5.78(3) $\mu_B/f.u.$ and -6.0(3) K, respectively. The value of $\mu_{eff}$ is close to the magnetic moment of 5.92 $\mu_B$ for the $Mn^{2+}$ ion in a high-spin configuration ($3d^5$, S = 5/2). The negative $\theta$ value indicates that the predominant magnetic interaction between Mn ions is antiferromagnetic, and actually an antiferromagnetic transition is observed at ~ 4 K (see the inset of Fig. 5).

Figure 4.6 shows the temperature dependence of the specific heat for $Sr_2MnSi_2O_7$. The data show a λ-type anomaly at 3.4 K, indicating the occurrence of the long-range antiferromagnetic ordering of $Mn^{2+}$ ions. The magnetic entropy ($S_{mag}$) due to the magnetic ordering was calculated from the specific heat data. To evaluate the lattice specific heat ($C_{lat}$) of $Sr_2MnSi_2O_7$, specific heat data for the nonmagnetic $Sr_2MgSi_2O_7$ were used. However, the specific heat of $Sr_2MgSi_2O_7$ showed a poor fit to the $C_p$ of $Sr_2MnSi_2O_7$ above the magnetic transition temperature. Then, the $C_{lat}$ of $Sr_2MnSi_2O_7$ was obtained from the sum of the Debye and Einstein models

$$C_{lat} = 9R\left(\frac{T}{\theta_D}\right)^3 \int_0^{\theta_D/T} \frac{(\theta_D/T)^4 e^{\frac{\theta_D}{T}}}{\left(e^{\frac{\theta_D}{T}}-1\right)^2} d(\theta_D/T) + R\sum_{i=1}^{3} \frac{(\theta_{E_i}/T)^2 e^{\frac{\theta_{E_i}}{T}}}{\left(e^{\frac{\theta_{E_i}}{T}}-1\right)^2}, \tag{4.3}$$

where $\theta_D$ is the Debye temperature, and $\theta_{E1}$ ~ $\theta_{E3}$ are the Einstein temperatures[19]. The calculated $C_{lat}$ values are shown as a solid line in Figure 4.6(a). The magnetic specific heat ($C_{mag}$) was obtained by subtracting the lattice specific heat ($C_{lat}$) from $C_p$. Then, the magnetic specific heat was determined by using the equation $S_{mag} = \int_0^T C_{mag}/TdT$. The magnetic specific heat below 1.8 K was extrapolated by the relation $C_{mag} \propto T^3$ from the spin-wave model for an antiferromagnet[20]. The temperature dependence of the magnetic

specific heat divided by temperature ($C_{mag}/T$) and magnetic entropy ($S_{mag}$) are plotted in Figure 4.6 (b). The $S_{mag}$ value reaches 12.5 J mol$^{-1}$ K$^{-1}$ at 100 K, which is close to the theoretical value $R\ln(2S+1) = R\ln6 = 14.90$ J mol$^{-1}$ K$^{-1}$ ($R$ = gas constant). This result shows that the observed magnetic transition is due to the antiferromagnetic ordering of the $Mn^{2+}$ ion in a high-spin configuration ($S = 5/2$).

4.3.3.2 $Eu_2MgSi_2O_7$

Figure 4.7 shows the temperature dependence of the reciprocal magnetic susceptibility for $Eu_2MgSi_2O_7$, in which only A site ions ($Eu^{2+}$) are magnetic. The susceptibility above 100 K was fitted by the Curie-Weiss law (Eq. (4.2)). The effective magnetic moment and Weiss constant were determined to be 11.02(4) $\mu_B$/*f.u.* and -1.2(4) K, respectively. The $\mu_{eff}$ value is in good agreement with the spin-only value (11.23 $\mu_B$) for two $Eu^{2+}$ ions ($S = 7/2$). The small negative Weiss constant may indicate the existence of the antiferromagnetic interaction between Eu ions; however, no magnetic transition is observed down to 1.8 K. The temperature dependence of the specific heat for $Eu_2MgSi_2O_7$ is plotted in Figure 4.8. Below ~10 K, the specific heat turns into increasing with decreasing temperature, which shows the onset of magnetic ordering of the Eu ions. Figure 4.9 shows the field dependence of the magnetization for $Eu_2MgSi_2O_7$ measured at 1.8 K. The magnetization ($M$) increases with magnetic field ($H$) and shows a saturation behavior. The value of the saturation magnetization (13.2 $\mu_B$) is reasonable for two Eu ions (7 $\mu_B \times 2$). The observed $M$-$H$ curve is below the Brillouin curve. Therefore, we fitted the data using a modified Brillouin function [21]:

$$M = gSB_S\left(\frac{gS\mu_B H}{k_B(T - T_0)}\right) \tag{4.4}$$

where parameter $T_0$ accounts phenomenologically for the magnetic interaction between $Eu^{2+}$ ions. The fitting curve is shown in Figure 4.9. The negative value of $T_0$ (-1.0 K)

agrees with the Weiss constant (-1.2 K) and it indicates that the ground state of $Eu_2MgSi_2O_7$ is antiferromagnetic.

4.3.3.3 $Eu_2MnSi_2O_7$

Figure 4.10 shows the temperature dependence of the reciprocal magnetic susceptibility for $Eu_2MnSi_2O_7$. In this compound, both the *A* and *M* sites are occupied by magnetic ions, *i.e.*, $Eu^{2+}$ ($4f^7$) and $Mn^{2+}$ ($3d^5$), respectively. The effective magnetic moment determined from the data above 100 K is 12.32(1) $\mu_B$/*f.u.*, which is in good agreement with the calculated value $\mu_{eff} = \sqrt{2 \times \mu^2_{Eu^{2+}} + \mu^2_{Mn^{2+}}}$ = 12.69 $\mu_B$ from the paramagnetic moments of $Eu^{2+}$ ($S = 7/2$) and $Mn^{2+}$ ($S = 5/2$) ions. The negative Weiss constant (-29.5(2) K) suggests the presence of the antiferromagnetic interaction. However, this compound shows a ferromagnetic-like anomaly below12 K.

In order to obtain furthermore information about this magnetic behavior, specific heat measurements were carried out. The specific heat $C_p$ data (Figure 4.11(a)) show a λ-type anomaly at 10.7 K, indicating the occurrence of the long-range magnetic ordering. The magnetic specific heat $C_{mag}$ is calculated by subtracting the lattice specific heat $C_{lat}$ (Eq.(4.3)) from the $C_p$ data. In a similar way to the case for $Sr_2MnSi_2O_7$, the $C_{lat}$ data were estimated from the sum of the Debye and Einstein models. The total magnetic entropy change (Fig. 11(b)) is 43.5 J $mol^{-1}$ $K^{-1}$ at 100 K, which is close to the value 49.48 J $mol^{-1}$ $K^{-1}$ expected from the sum of $2R\ln 8$ for $Eu^{2+}$ and $R\ln 6$ for $Mn^{2+}$. Therefore, this magnetic transition is due to the magnetic ordering of both Eu and Mn ions.

The negative Weiss constant may indicate that the observed magnetic transition is attributed to a ferrimagnetic ordering rather than a ferromagnetic one. According to the molecular field theory, the temperature dependence of the reciprocal magnetic susceptibility for a ferrimagnet is represented by

$$\frac{1}{\chi - \chi_{TIP}} = \frac{T}{C} + \frac{1}{\chi_0} - \frac{\sigma}{T - \theta}, \quad (4.5)$$

where the parameters $\chi_0$, $\theta$, and $\sigma$ are related to the molecular field magnetic coefficients[22]. For $Eu_2MnSi_2O_7$, the Curie temperature

$T_C$ (= $(\theta - C/\chi_0 + \sqrt{(\theta - C/\chi_0)^2 + 4C(\theta/\chi_0 + \sigma)})/2$) and the Curie constant $C$ (= $C_{Eu} + C_{Mn}$)

are determined to be 10.69(1) K and 18.99(4) emu K $mol^{-1}$, respectively, by fitting Eq. (4.5) to the $\chi_M^{-1}$–$T$ curve as shown in Figure 4.10. The $T_C$ value agrees with the temperature at which magnetic susceptibility and specific heat measurements show an anomaly (10.7 K).

The field dependence of the magnetization for $Eu_2MnSi_2O_7$ measured at 1.8K is also shown in Figure 4.9. The magnetization increases quickly with magnetic field and shows a saturation behavior. The saturation magnetization ~ 9.0 $\mu_B$ is much smaller than the value 19 $\mu_B$ expected from the fully ferromagnetic ordering of both $Eu^{2+}$ (7 $\mu_B \times 2$) and $Mn^{2+}$ sublattices (5 $\mu_B$) and rather close to 9 $\mu_B$ for a ferrimagnetic ordering between sublattices.

4.3.3.4 Magnetic interaction in $A_2MSi_2O_7$ ($A$ = Sr, Eu; $M$ = Mg, Mn)

From the magnetic measurements of $Sr_2MnSi_2O_7$, an antiferromagnetic ordering of $Mn^{2+}$ ions is observed at 3.4 K. The interatomic distances of Mn ions are 5.75 Å (= $a/\sqrt{2}$) in the *ab*-plane and 5.16 Å (= $c$) along the *c*-axis (see Figure 4.1 and Figure 4.2). Recently, the exchange integral $|J|$ values for two interaction pathways in the analogous compound $Ba_2MnGe_2O_7$ ($T_N$ = 4.0 K) were determined by the inelastic neutron scattering experiment: 27.8 $\mu$eV (the Mn - Mn distance is 6.01 Å) and 1.0 $\mu$eV (5.53 Å), respectively[4]. Thus, it is expected that the antiferromagnetic interaction between Mn - Mn ions in the *ab*-plane is predominant also in $Sr_2MnSi_2O_7$. On the other hand, the experimental results on $Eu_2MgSi_2O_7$ indicate that the magnetic interaction between *A*

sites ($Eu^{2+}$ ions) is also antiferromagnetic. Nevertheless, $Eu_2MnSi_2O_7$ shows a ferrimagnetic transition at 10.7 K. The data of specific heat and magnetization measurements are well explained by the antiparallel arrangement of the Eu and Mn sublattices, *i.e.*, the ferromagnetic $Eu^{2+}$ (14 $\mu_B$) layer and ferromagnetic $Mn^{2+}$ (5 $\mu_B$) layer, in contrary to the expected antiferromagnetic Mn-Mn and Eu-Eu interactions, are alternately stacked along the *c*-axis. In this structure, the interatomic distance between Eu and Mn ions is 3.97 ~ 4.00 Å, which is shorter than those of Mn - Mn ions (5.74 Å) and Eu - Eu ions (4.29 Å). This result indicates that an antiferromagnetic interaction between Eu and Mn ions is predominant in this compound.

## 4.4 Summary

We here report synthesis, crystal structures and magnetic properties of quaternary compounds $A_2MSi_2O_7$($A$ = Sr, Eu, $M$ = Mg, Mn). They crystallize in a tetragonal melilite-type structure with space group $P\text{-}42_1m$. The $^{151}$Eu Mössbauer spectrum measurements show that the Eu ions are in the divalent state in these compounds. $Sr_2MnSi_2O_7$ shows an antiferromagnetic transition at 3.4 K. On the other hand, $Eu_2MnSi_2O_7$ shows a ferrimagnetic transition at 10.7 K.

## 4.5 Tables and figures

Table 4.1 Structural parameters for $A_2MnSi_2O_7$ ($A$ = Sr, Eu).

| Atom | Site | $X$ | $y$ | $Z$ | $B$(Å$^2$) |
|---|---|---|---|---|---|
| $Sr_2MnSi_2O_7$; Space group $P\bar{4}2_1m$ (No. 113), $Z$ = 2, $a$ = 8.1315(1) Å, $c$ = 5.1589(1) Å, $R_{wp}$ = 9.22 %, $R_p$ = 6.80 %, $R_e$ = 2.99 %, $R_I$ = 1.90 % | | | | | |
| Sr | 4*e* | 0.3333(1) | 0.1667 | 0.5068(2) | 0.82(1) |
| Mn | 2*a* | 0 | 0 | 0 | 0.51(4) |
| Si | 4*e* | 0.1361(2) | 0.3639 | 0.9399(4) | 0.50(1) |
| O1 | 2*c* | 1/2 | 0 | 0.1420(1) | 0.92(7) |
| O2 | 4*e* | 0.1420(5) | 0.3580 | 0.2454(9) | 0.92 |
| O3 | 8*f* | 0.0767(4) | 0.2007(5) | 0.7939(8) | 0.92 |
| $Eu_2MnSi_2O_7$ ; Space group $P\bar{4}2_1m$ (No. 113), $Z$ = 2, $a$ = 8.1390(2) Å, $c$ = 5.1635(1) Å, $R_{wp}$ = 9.87 %, $R_p$ = 7.05 %, $R_e$ = 7.52 %, $R_I$ = 2.28 % | | | | | |
| Eu | 4*e* | 0.3342(1) | 0.1658 | 0.5055(2) | 0.37(2) |
| Mn | 2*a* | 0 | 0 | 0 | 0.54(6) |
| Si | 4*e* | 0.1366(3) | 0.3634 | 0.9422(7) | 0.30(1) |
| O1 | 2*c* | 1/2 | 0 | 0.1421(1) | 0.30(1) |
| O2 | 4*e* | 0.1432(7) | 0.3568 | 0.2501(1) | 0.30 |
| O3 | 8*f* | 0.0791(6) | 0.1946(7) | 0.7980(1) | 0.30 |

Table 4.2 Structural parameters for $A_2MgSi_2O_7$ ($A$ = Sr, Eu).

| Atom | Site | $x$ | $y$ | $z$ | $B$(Å$^2$) |
|---|---|---|---|---|---|
| $Sr_2MgSi_2O_7$ ; Space group $P\bar{4}2_1m$ (No. 113), $Z$ = 2, $a$ = 8.0107(2) Å, $c$ = 5.1636(1) Å, $R_{wp}$ = 6.90 %, $R_p$ = 4.96 %, $R_e$ = 3.03 %, $R_I$ = 2.29 % | | | | | |
| Sr | 4*e* | 0.3341(3) | 0.1659 | 0.5074(2) | 0.78(2) |
| Mg | 2*a* | 0 | 0 | 0 | 0.50(1) |
| Si | 4*e* | 0.1354(2) | 0.3646 | 0.9459(5) | 0.53(6) |
| O1 | 2*c* | 1/2 | 0 | 0.1576(5) | 1.00(1) |
| O2 | 4*e* | 0.1385(5) | 0.3616 | 0.2505(9) | 1.00 |
| O3 | 8*f* | 0.0788(4) | 0.1948(4) | 0.8112(7) | 1.00 |
| $Eu_2MgSi_2O_7$ ; Space group $P\bar{4}2_1m$ (No. 113), $Z$ = 2, $a$ = 8.0138(2) Å, $c$ = 5.1711(1) Å, $R_{wp}$ = 9.73 %, $R_p$ = 6.70 %, $R_e$ = 6.32 %, $R_I$ = 2.36 % | | | | | |
| Eu | 4*e* | 0.3353(1) | 0.1647 | 0.5059(3) | 0.54(2) |
| Mg | 2*a* | 0 | 0 | 0 | 0.30(1) |
| Si | 4*e* | 0.1367(3) | 0.3633 | 0.9439(8) | 0.30(1) |
| O1 | 2*c* | 1/2 | 0 | 0.1470(2) | 0.20(1) |
| O2 | 4*e* | 0.1408(7) | 0.3592 | 0.2610(1) | 0.20 |
| O3 | 8*f* | 0.0818(6) | 0.1923(6) | 0.8080(1) | 0.20 |

Table 4.3 Selected interatomic distances (Å) and bond valence sums determined by X-ray diffraction measurements.

| | $Sr_2MgSi_2O_7$ | $Sr_2MnSi_2O_7$ | $Eu_2MgSi_2O_7$ | $Eu_2MnSi_2O_7$ |
|---|---|---|---|---|
| A-O2 | 2.582(5) | 2.580(5) | 2.542(7) | 2.565(7) |
| A-O3×2 | 2.588(4) | 2.573(4) | 2.572(6) | 2.579(6) |
| A-O1 | 2.606(1) | 2.686(5) | 2.634(7) | 2.679(7) |
| A-O2'×2 | 2.749(4) | 2.825(4) | 2.736(5) | 2.820(6) |
| A-O3'×2 | 2.792(4) | 2.736(4) | 2.802(5) | 2.780(5) |
| BVS ($A^{2+}$) | 1.80 | 1.76 | 1.77 | 1.87 |
| M-O3 | 1.945(3) | 2.045(54) | 1.947(5) | 2.002(5) |
| BVS ($M^{2+}$) | 2.05 | 2.01 | 2.01 | 2.26 |
| Si-O2 | 1.573(5) | 1.577(5) | 1.640(8) | 1.590(8) |
| Si-O3×2 | 1.594(3) | 1.600(4) | 1.602(5) | 1.630(5) |
| Si-O1 | 1.624(3) | 1.622(3) | 1.619(4) | 1.631(4) |
| BVS ($Si^{4+}$) | 4.29 | 4.25 | 4.07 | 4.03 |

Table 4.4 Mössbauer parameters for $Eu_2MSi_2O_7$ (M = Mg, Mn).

| Compound | I.S. ($mm/s^{-1}$) | Q.S. ($mm/s^{-1}$) | $\eta$ | $\Gamma$($mm/s^{-1}$) |
|---|---|---|---|---|
| $Eu_2MgSi_2O_7$ | -12.81(1) | -13.65(2) | 0.26(3) | 2.82(4) |
| $Eu_2MnSi_2O_7$ | -12.84(5) | -14.91(4) | 0.29(4) | 2.19(4) |

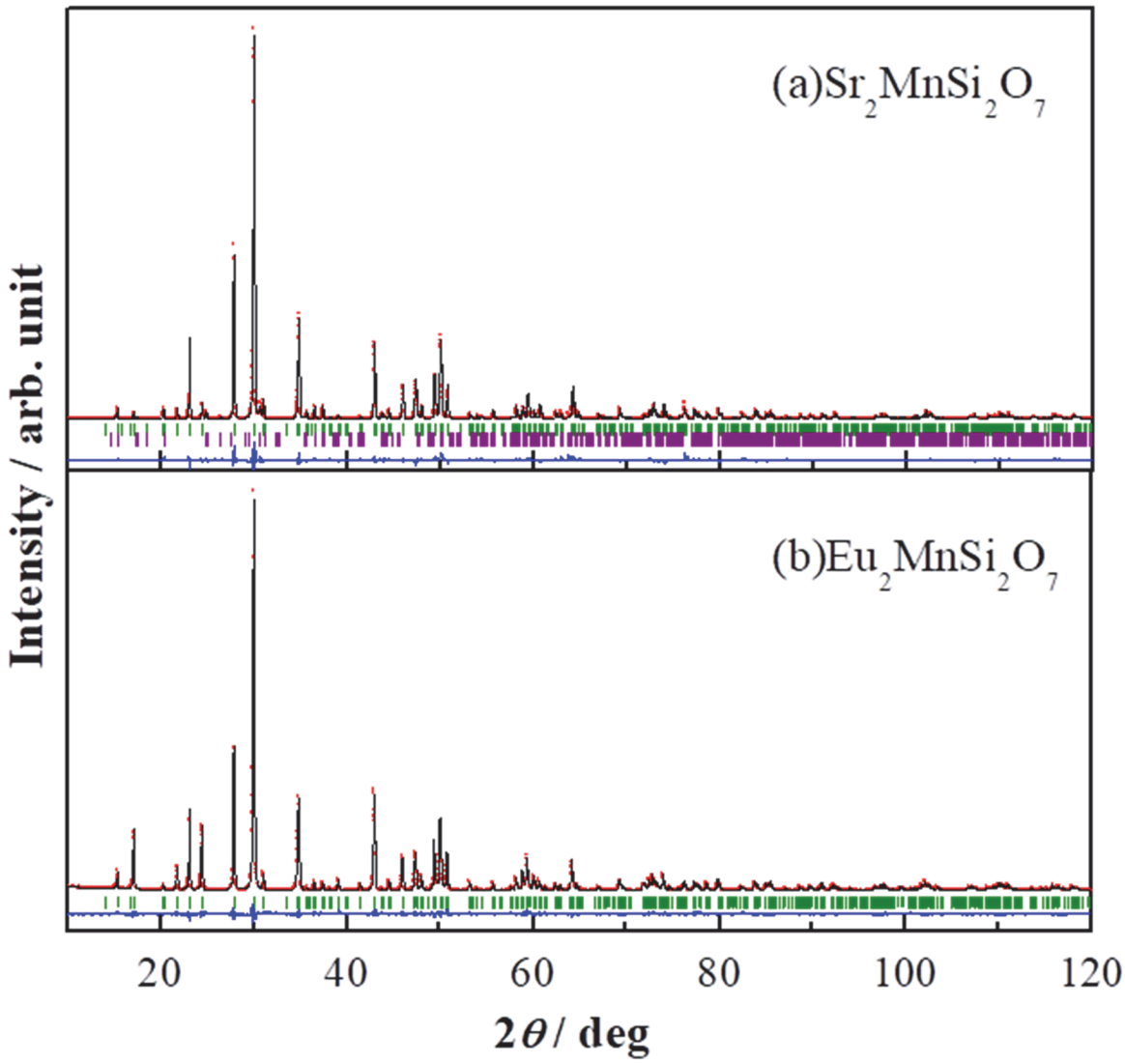


Figure 4.1 Powder X-ray diffraction profiles for (a) $Sr_2MnSi_2O_7$ and (b) $Eu_2MnSi_2O_7$. The calculated and observed profiles are shown on the top black solid line and red cross markers, respectively. The vertical marks in the middle show positions calculated for Bragg reflections. The lower trace is a plot of the difference between calculated and observed intensities. For (a), the second vertical marks show an impurity phase ($SrSiO_3$).

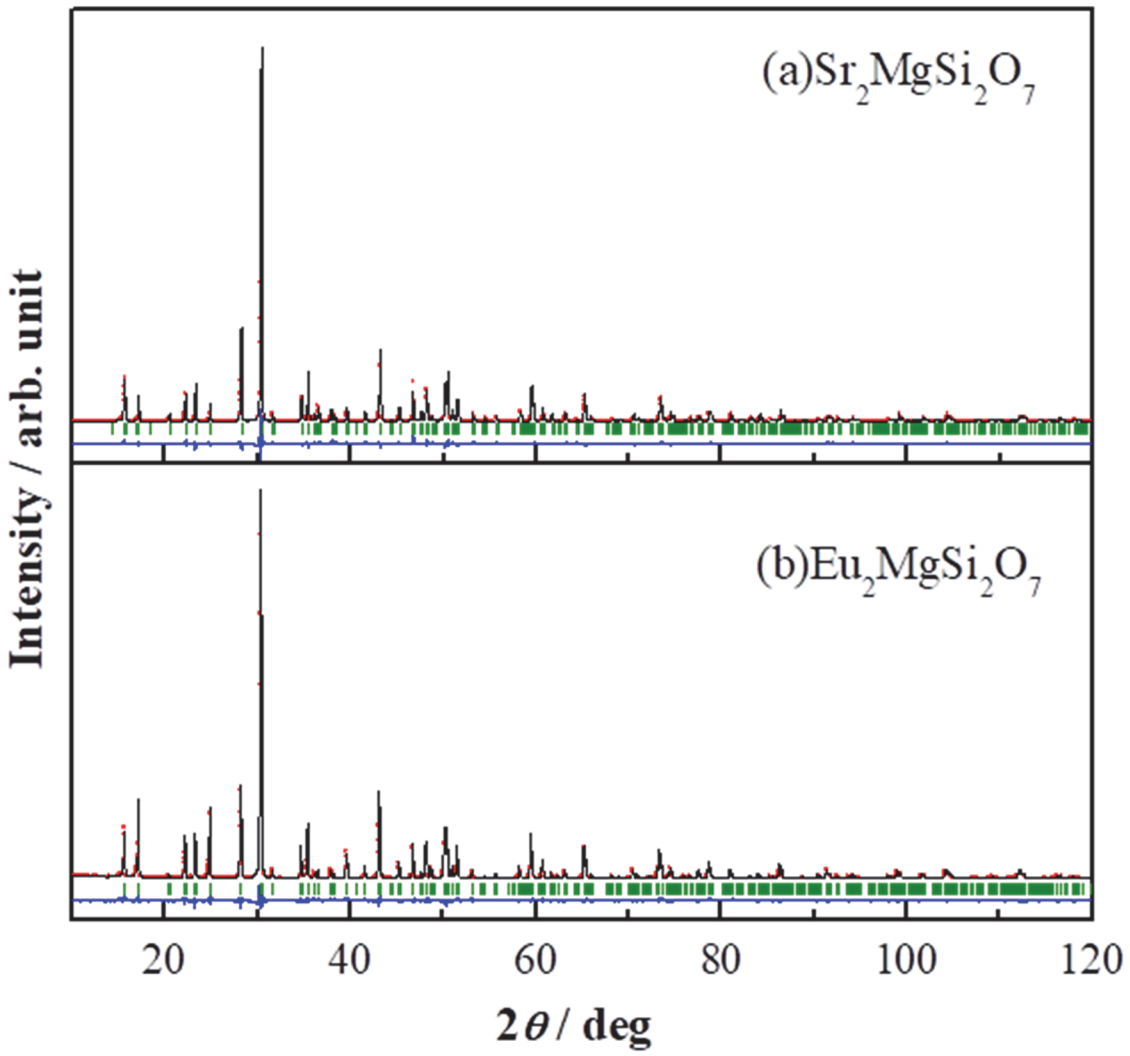


Figure 4.2 Powder X-ray diffraction profiles for (a) $Sr_2MgSi_2O_7$ and (b) $Eu_2MgSi_2O_7$. The calculated and observed profiles are shown on the top black solid line and red dot markers, respectively. The vertical marks in the middle show positions calculated for Bragg reflections. The lower trace is a plot of the difference between calculated and observed intensities.

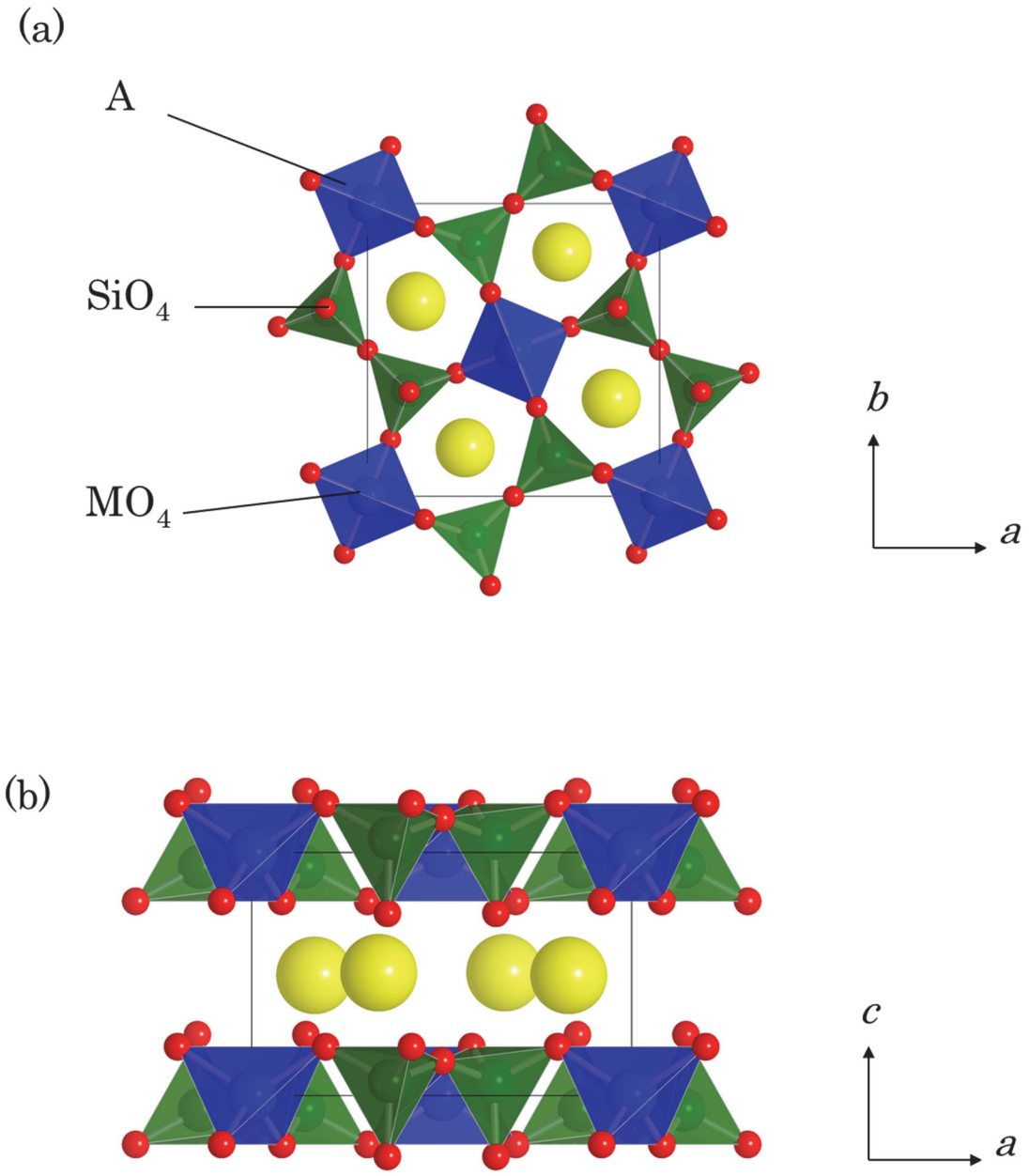


Figure 4.3 The schematic crystal structure of melilite-type oxides $A_2MSi_2O_7$ (A = Sr, Eu; M = Mg, Mn). (a) viewed from the *c*-axis, (b) projection of the structure in the *ac*-plane.

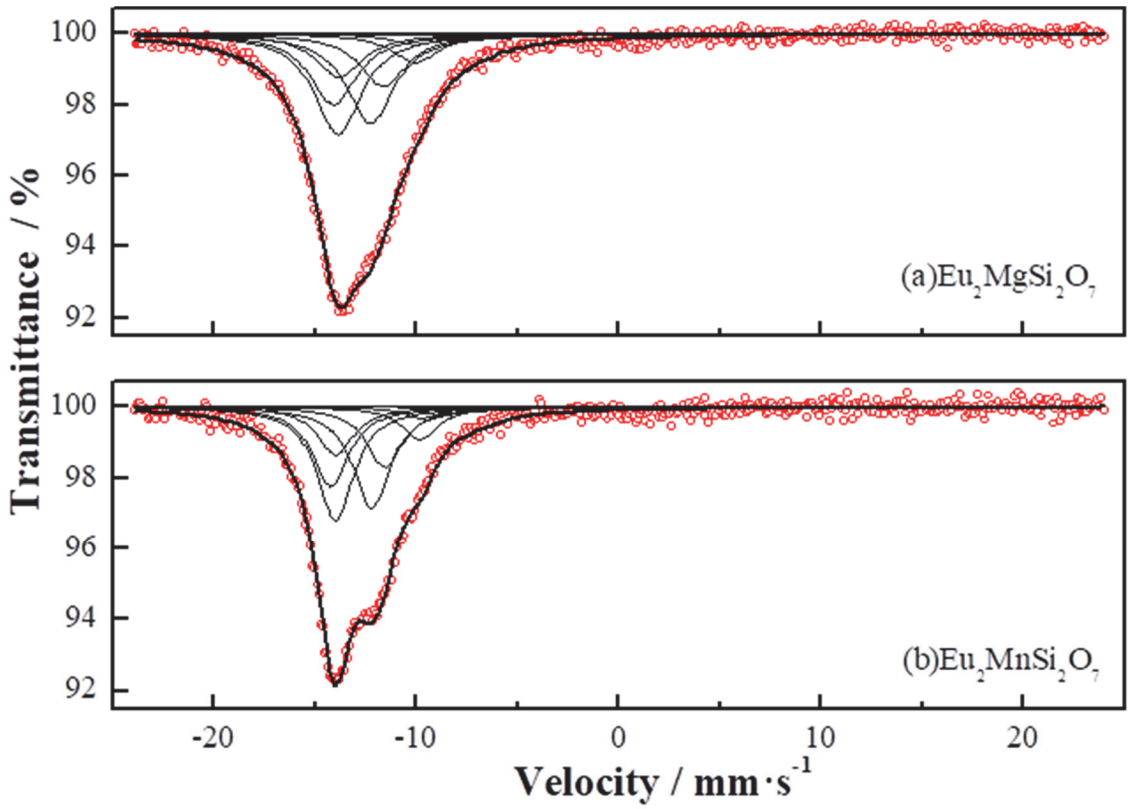


Figure 4.4 Mössbauer spectra for (a) $Eu_2MgSi_2O_7$ and (b) $Eu_2MnSi_2O_7$. The observed spectra are shown on the red circles.

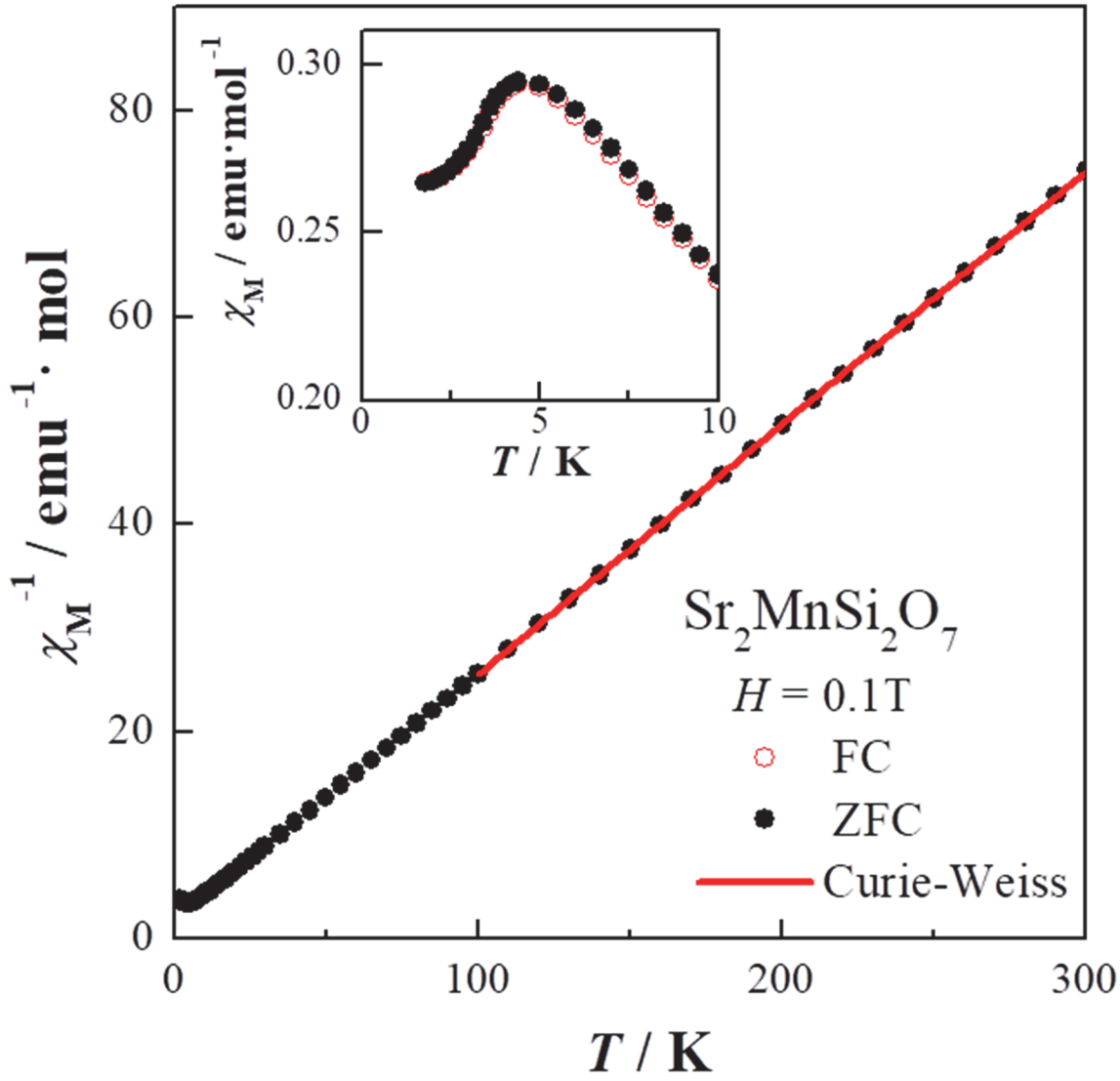


Figure 4.5 Temperature dependence of the reciprocal magnetic susceptibility of $Sr_2MnSi_2O_7$. The red-solid line is a fitting result by the Curie-Weiss law. The inset shows the susceptibility *v.s.* temperature curve at low temperatures.

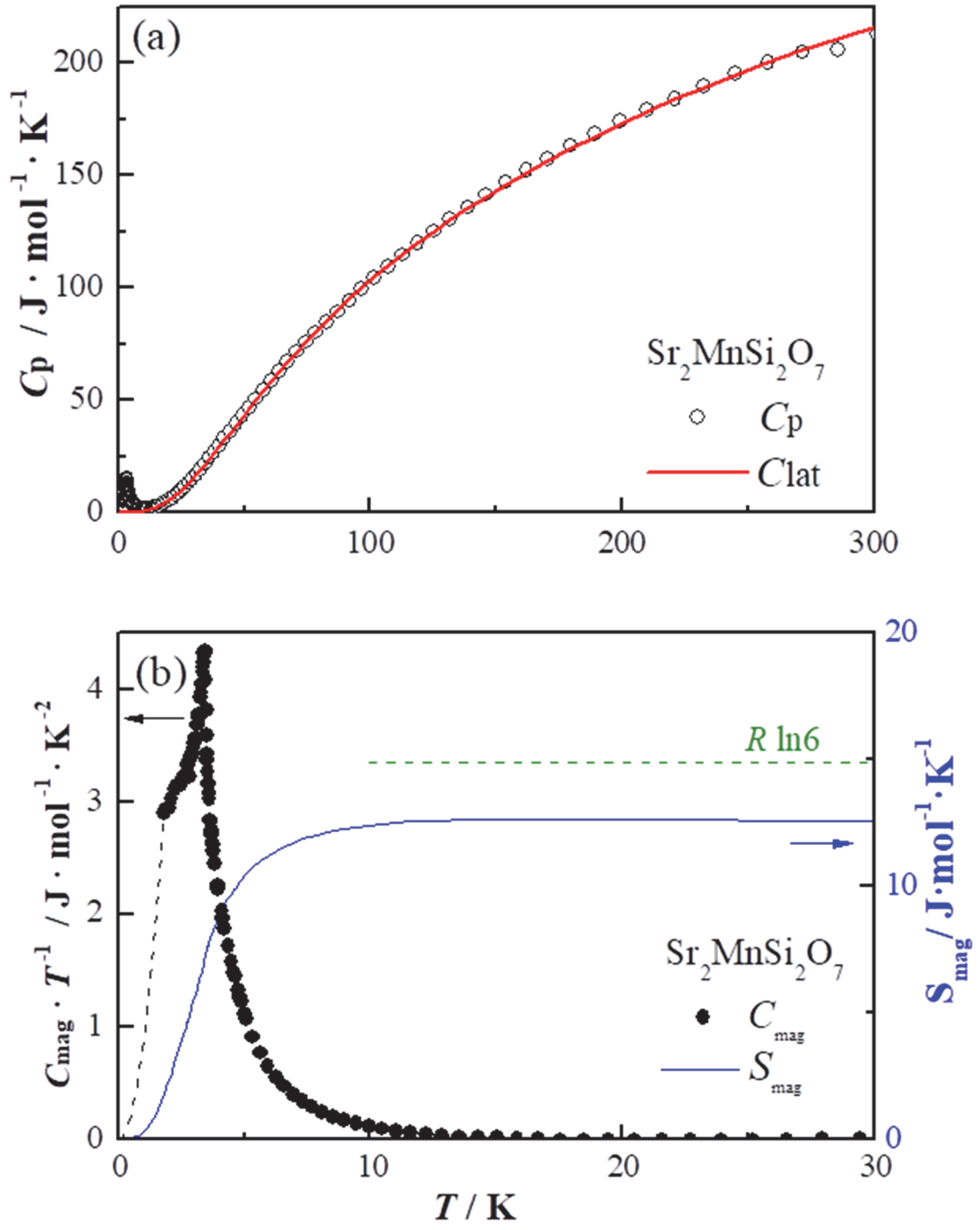


Figure 4.6 (a) Temperature dependence of specific heat ($C_P$), and (b) magnetic specific heat divided by temperature ($C_{mag}T^{-1}$) and magnetic entropy ($S_{mag}$) for $Sr_2MnSi_2O_7$.

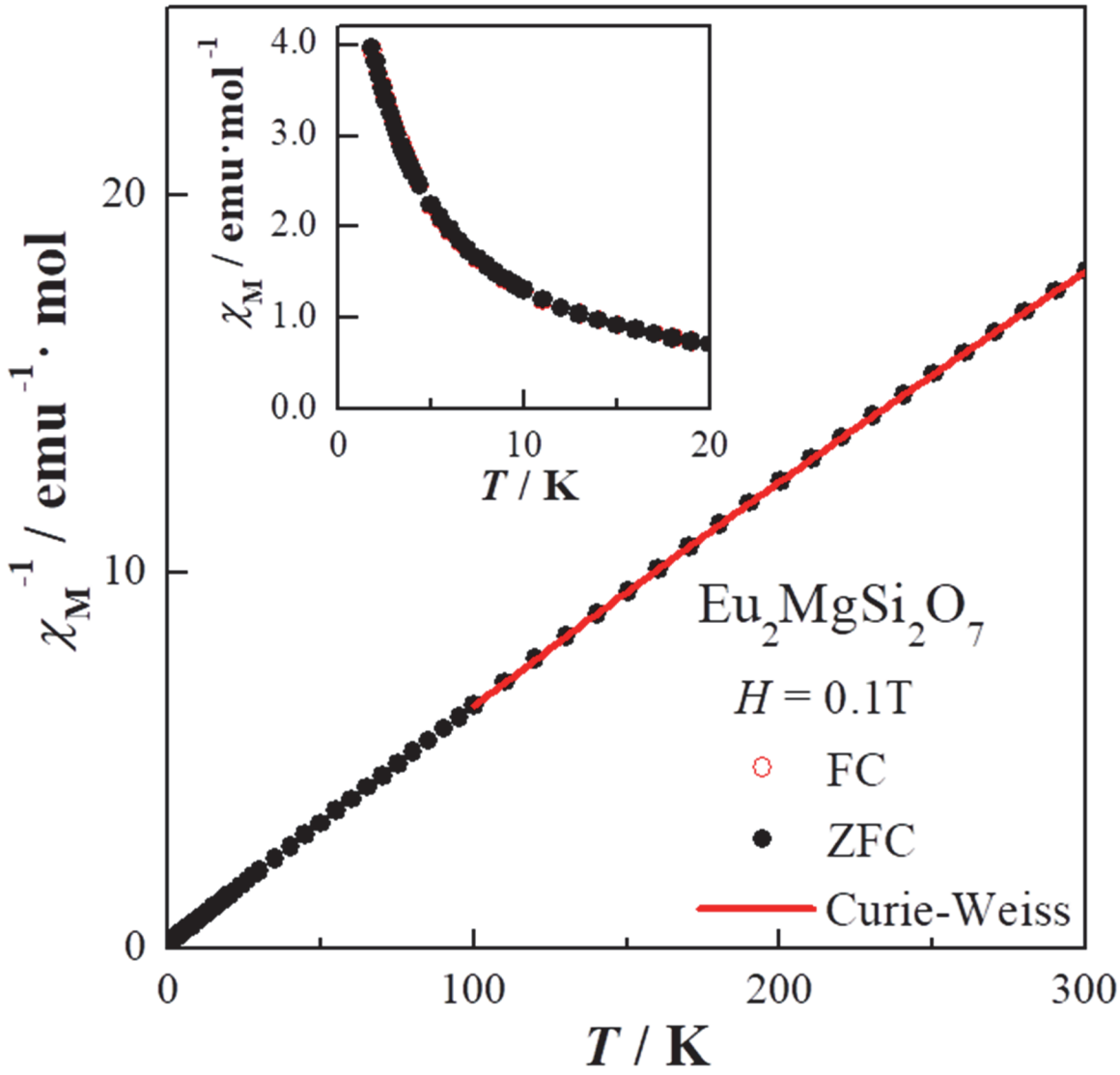


Figure 4.7 Temperature dependence of the reciprocal magnetic susceptibility of $Eu_2MgSi_2O_7$. The red-solid line is a fitting result by the Curie-Weiss law. The inset shows the susceptibility *v.s.* temperature curve at low temperatures.

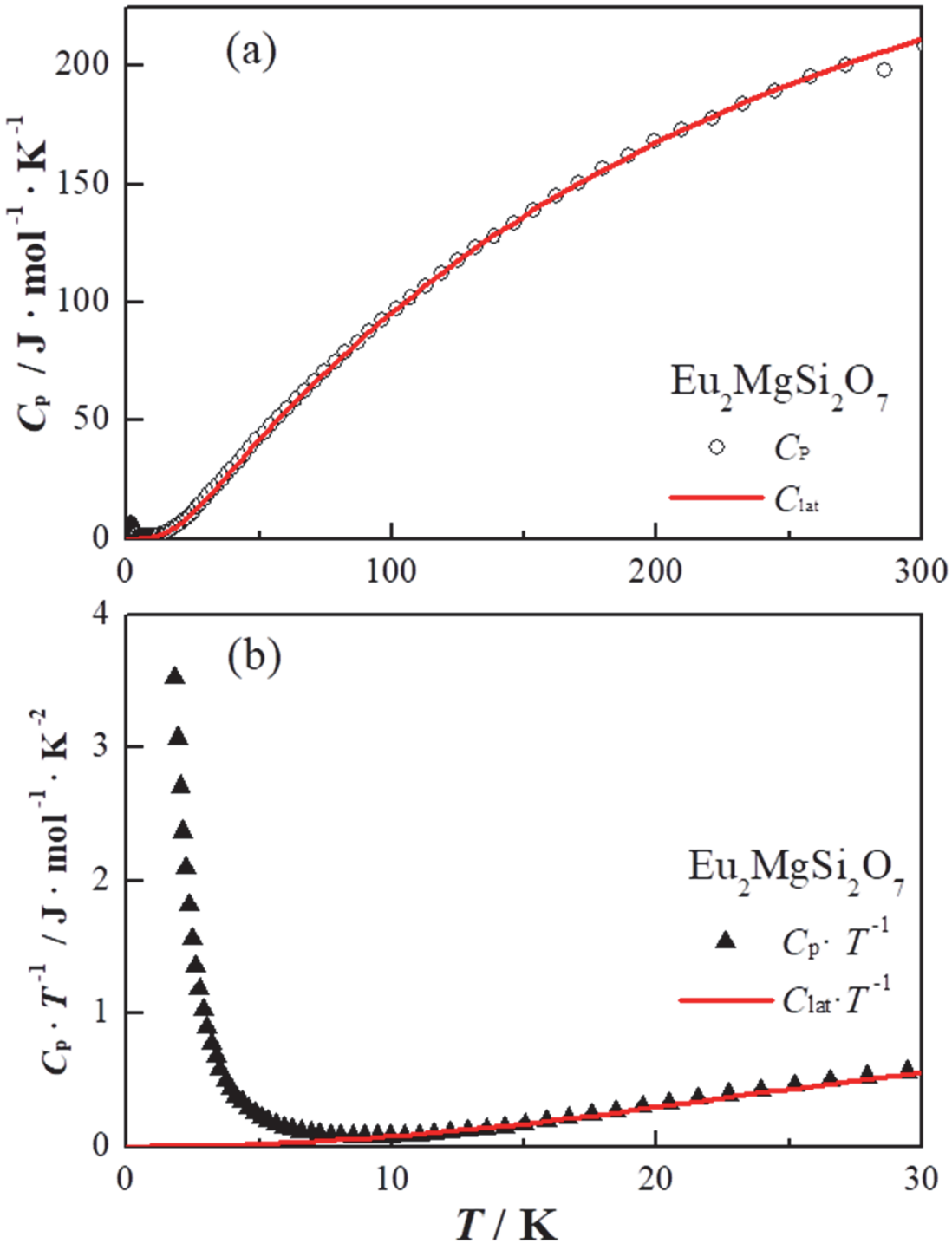


Figure 4.8 (a) Temperature dependence of specific heat ($C_P$) and (b) specific heat divided by temperature ($C_{mag}T^{-1}$) at low temperature range for $Eu_2MgSi_2O_7$.

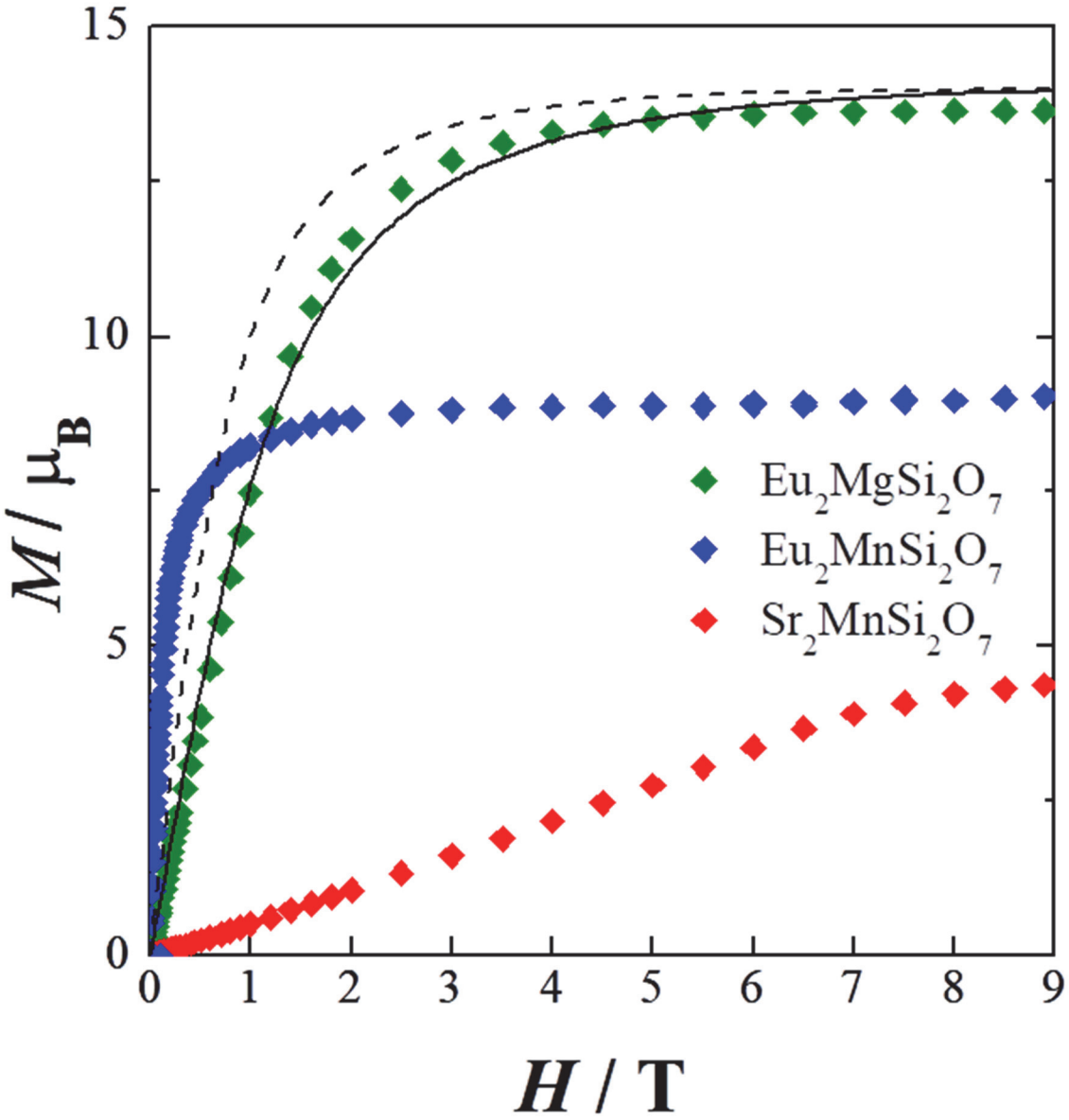


Figure 4.9 Field dependence of the magnetization curve of $A_2MSi_2O_7$ compounds measured at 1.8 K. The black dashed and solid lines are the normal and modified Brillouin functions with S = 7/2. (see text) There are no hysteresis loops in all the data.

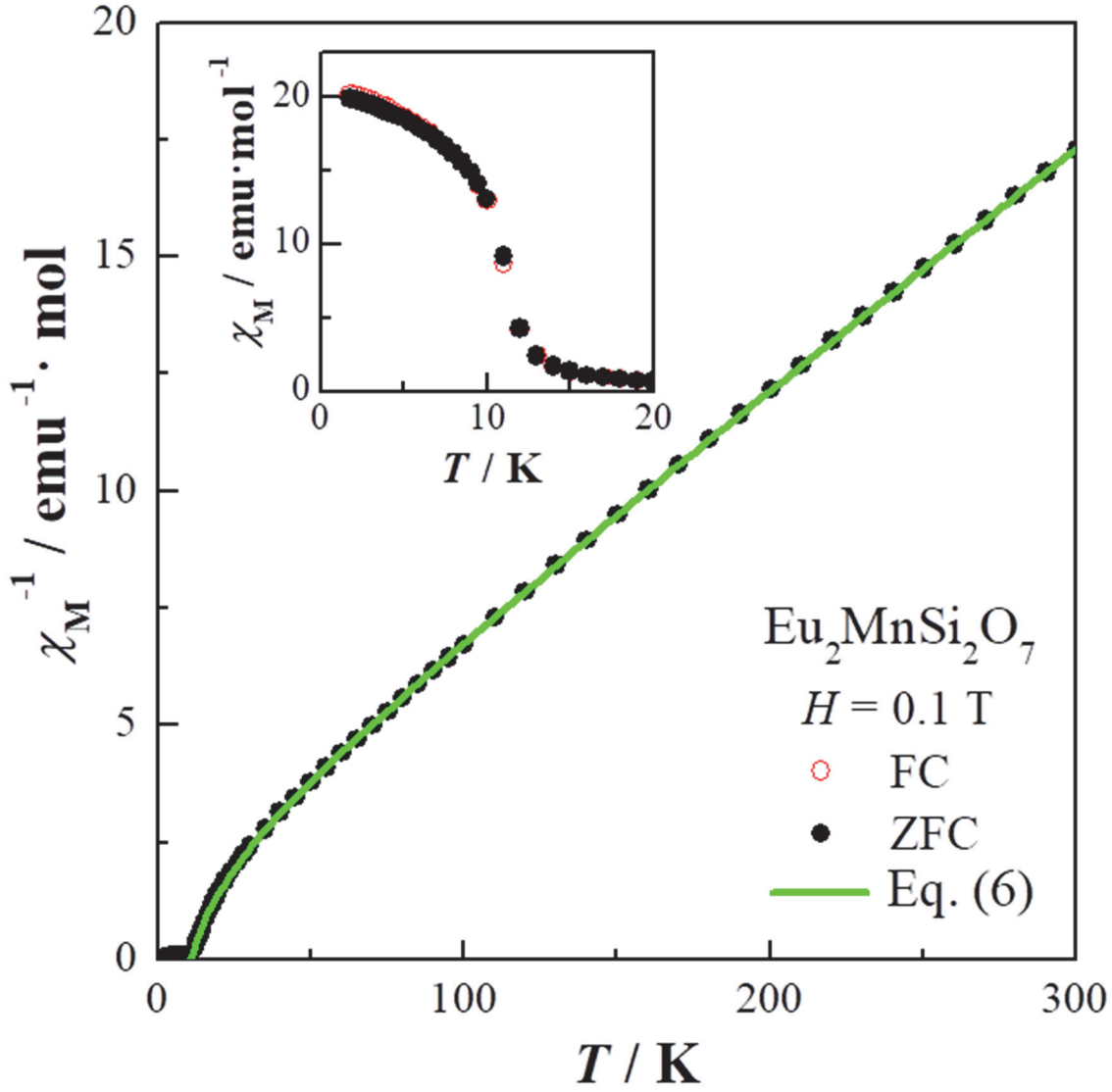


Figure 4.10 Temperature dependence of the reciprocal magnetic susceptibility of $Eu_2MnSi_2O_7$. The green-solid line is a fitting curve by Eq. (4.5) (see text.). The inset shows the susceptibility *v.s.* temperature curve at low temperatures.

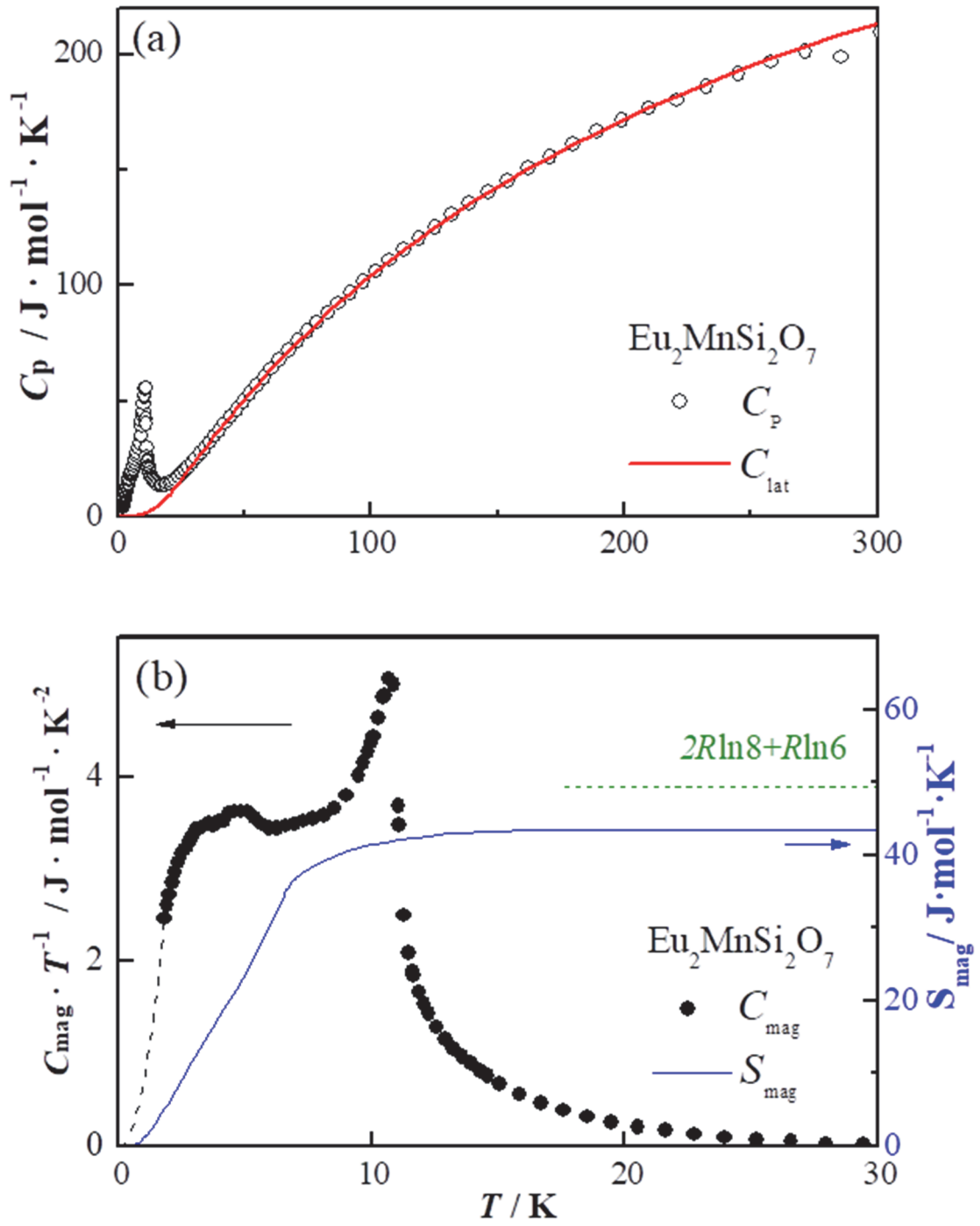


Figure 4.11 (a) Temperature dependence of specific heats divided by temperature ($C_pT^{-1}$) and (b) the magnetic specific heat divided by temperature ($C_{mag}T^{-1}$) and magnetic entropy ($S_{mag}$) for $Eu_2MnSi_2O_7$.

## 4.6 References

(1) Burzo, E. Melilites and Related Silicates in Landolt-Börnstein, New Series; Springer: Berlin, 2005.

(2) Kaminskii, A. A.; Bohatý, L.; Becker, P.; Liebertz, J.; Held, P.; Eichler, H. J.; Rhee, H.; Hanuza, J. Tetragonal $Ba_2MgGe_2O_7$- a Novel Multifunctional Optical Crystal with Numerous Manifestations of Nonlinear-Laser Effects: Almost Sesqui-Octave Stokes and Anti-Stokes Combs and Cascaded $\chi$ (3) ↔ $\chi$ (2) Lasing with Involved Sec. *Laser Phys. Lett*. **2008**, 5, 845–868.

(3) Mill, B. V.; Bailbakova, G. D., New compounds with melilite structure: $Ln_2SiBe_2O_7$ (*Ln* = Nd-Eu, Tb, Ho-Lu) and $Ln_2GeBe_2O_7$ (*Ln* = Nd, Eu, Tb, Ho, Tm-Lu). *Russ. J. Inorg. Chem*. 1990, 35, 341–343.

(4) Masuda, T.; Kitaoka, S.; Takamizawa, S.; Metoki, N.; Kaneko, K.; Rule, K. C.; Kiefer, K.; Manaka, H.; Nojiri, H. Instability of Magnons in Two-Dimensional Antiferromagnets at High Magnetic Fields. *Phys. Rev. B,* **2010**, 81, 100402.

(5) Zheludev; Shirane; Sasago; Kiode; Uchinokura. Spiral Phase and Spin Waves in the Quasi-Two-Dimensional Antiferromagnet $Ba_2CuGe_2O_7$. *Phys. Rev. B,* **1996**, 54, 15163–15170.

(6) Akaki, M.; Tozawa, J.; Akahoshi, D.; Kuwahara, H. Magnetic and Dielectric Properties of $A_2CoSi_2O_7$ (*A* =Ca, Sr, Ba) Crystals. *J. Phys. Conf. Ser.* **2009**, 150, 042001.

(7) Ochi, Y.; Morikawa, H.; Marumo, F.; Nozaki, H. Structures and Magnetic Properties of Rare Earth Compounds in the Melilite Group. *Yogyo Kyokaishi,* **1983**, 91, 229–235.

(8) Izumi, F.; Momma, K. Three-Dimensional Visualization in Powder Diffraction. *Solid State Phenom.* **2007**, 130, 15–20.

(9) Momma, K.; Izumi, F. VESTA : A Three-Dimensional Visualization System for Electronic and Structural Analysis. *J. Appl. Crystallogr*. **2008**, 41, 653–658.

(10) Blaha, P.; Schwarz, K.; Madsen, G.; Kvasnicak, D.; Luitz, J. WIEN2k, An Augmented Plane Wave Plus Local Orbitals Program for Calculating Crystal Properties.; 2001.

(11) Kimata, M. The Structural Properties of Synthetic Sr-Akermanite , $Sr_2MgSi_2O_7$. *Zeitschrift für Krist*. **1983**, 304, 295–304.

(12) Shannon, R. D. Revised Effective Ionic Radii and Systematic Studies of Interatomic Distances in Halides and Chalcogenides. *Acta Crystallogr. Sect. A,* **1976**, 32, 751–767.

(13) Brown, I. D.; Altermatt, D. Bond-Valence Parameters Obtained from a Systematic Analysis of the Inorganic Crystal Structure Database. *Acta Crystallogr. Sect. B Struct. Sci,* **1985**, 41, 244–247.

(14) Brese, N. E.; O'Keeffe, M. Bond-Valence Parameters for Solids. *Acta Crystallogr. Sect. B Struct. Sci,* **1991**, 47, 192–197.

(15) Long, G. J.; Grandjean, F. Mössbauer Spectroscopy Applied to Inorganic Chemistry Vol.3; Plenum Press: New York, 1986.

(16) Shenoy, G. K.; Dunlap, B. D. Method for the Analysis of Pure Quadrupole Spectra in Nuclear Gamma-Ray Resonance. *Nucl. Instruments Methods*, **1969**, 71, 285–291.

(17) Robinson, J. W. Handbook of Spectroscopy Vol 3; CRC: Boca Raton FL, 1981.

(18) Zong, Y.; Fujita, K.; Akamatsu, H.; Murai, S.; Tanaka, K. Antiferromagnetism of Perovskite $EuZrO_3$. *J. Solid State Chem.* **2010**, 183, 168–172.

(19) Grimvall, G. Thermophysical Properties of Materials (Selected Topics in Solid State Physics, No 18); North-Holland: New York, 1986.

(20) Joshua, S. J.; Cracknell, A. P. The Spin-Wave Contribution to the Specific Heat of $NiF_2$. *Phys. Lett. A* **1969**, 28, 562–563.

(21) Zielinski; Rigaux; Lemaître; Mycielski; Deportes. Exchange Interactions and Magnetism of $Co^{2+}$ in $Zn_{1-x}Co_xTe$. *Phys. Rev. B.* **1996**, 53, 674–685.

(22) Néel, M. Louis. Propriétés Magnétiques Des Ferrites ; Ferrimagnétisme et Antiferromagnétisme. *Ann. Phys*. **1948**, 12, 137–198.

# Chapter 5

# Magnetic Properties of Melilite-Type Oxysulfide $Sr_2MnGe_2S_6O$: Magnetic Interactions Enhanced by Anion Substitution

## 5.1 Introduction

The Melilite-type compounds are represented by a general formula $A_2MM'_2X_7$ ($A$ = larger cations such as alkali earth and lanthanide ions; $M$, $M'$ = smaller divalent to tetravalent ions; $X$ = N, O, F, S)[1,2], and have recently received broad attention due to their interesting optical[3], oxygen-conducting[4], magnetic[5], and dielectric properties[6]. The schematic crystal structure of melilite-type compounds is illustrated in Figure 5.1. In this structure, the $M$ and $M'$ ions occupy tetrahedral sites and these tetrahedra form a two-dimensional (2D) network in the *ab*-plane, and larger $A$ ions are located between the networks.

Recently, the melilite-type compounds attract great deal of interests because of their low-dimensional magnetic and multiferroic behaviors. Their magnetic properties are summarized in Table 5.1. [5–24] Among them, the $A_2MM'_2O_7$ ($A$ = Sr, Ba; $M$ = Mn, Co, Cu; $M'$ = Si, Ge), in which only the $M$ ion is magnetic and the others are diamagnetic, are extensively studied. In the melilite-type structure, it is considered that the intra-layer interaction between $M$ ions is much stronger than the inter-layer one [13–15]. Therefore, some compounds show the 2D antiferromagnetic (AFM) behavior due to the square-planer arrangement of the magnetic $M$ ions in *ab*-plane. In addition, at lower temperatures an AFM transition ($M$ = Mn) [13–15], multiferroic behavior derived from AFM and ferroelectric transitions under the magnetic field (Co)[5,6,13,15–19], and spiral AFM ordering

and incommensurate-commensurate magnetic transition (Cu)[15,20–23] have been observed. To explore further interesting materials, we have paid our attention to the anion substation. The anion substituted compounds such as the $LaO_{1-x}F_xFeAs$ (superconducting behavior)[25] and $Sr_2MnO_2Cu_{1.5}S_2$ (the unusual magnetic structure)[26] often show novel electronic and magnetic properties. In the case of melilite-type compounds, the anion substitution should strongly affect the super-super exchange *M-X-X-M* interaction, and may bring about further variation of magnetic phase transition. For this purpose, we select the $S^{2-}$ ion with the same valence and more covalent bonding nature against the $O^{2-}$ ion. About the melilite-oxysulfide compounds, the crystal structure and optical properties of $ALnGa_3S_6O$(*A* = Ca, Sr, *Ln* = La, Gd) [27–30], $A_2ZnGe_2S_6O$ (*A* = Sr, La)[31 32] have been reported. However, no previous investigations were carried out for compounds containing magnetic ions and their physical properties.

In this study, we investigated the synthesis, crystal structures, and magnetic properties of new melilite-oxysulfides $Sr_2MnGe_2S_6O$. For comparison, the analogues compounds $Sr_2ZnGe_2S_6O$[32] and $Sr_2MnGe_2O_7$[13] were also prepared. The results of the powder X-ray diffraction, XPS measurements, magnetic susceptibility, specific heat and DFT calculation are discussed. This is the first report for the magnetic ions introduced into melilite-oxysulfides system.

## 5.2 Experimental procedures

### 5.2.1 Synthesis

Polycrystalline samples (0.5g) of $Sr_2MGe_2S_6O$ (*M* = Mn and Zn) were prepared by the standard solid-state reaction. As starting materials, SrS, MnO, ZnO and $GeS_2$ were used. They were weighed out in a stoichiometric ratio, and well mixed in an agate mortar in a glove box under an Ar atmosphere. The mixture was pressed into pellets and then

sealed in an evacuated quartz tube. To avoid a reaction with the quartz tube, the pellet was set into a small inner crucible made by carbon. These ampoules were heated at 800 °C for 12 h. For comparison, the melilite-type oxide $Sr_2MnGe_2O_7$ with a stoichiometric chemical composition (white colored) was also prepared by the same synthesis method as reported elsewhere[13]. It is to be noted that if this oxide is prepared in air, the blue ~ black colored $Sr_2MnGe_2O_{7+\delta}$ containing excess oxygen ion is obtained [13, 33].

## 5.2.2 Crystal Structure Analysis

Powder X-ray diffraction (XRD) measurements were performed at room temperature using a Multi-Flex diffractometer (Rigaku) with a Cu Kα X-ray radiation source equipped with a curved graphite monochromator. The data were collected by step-scanning in the angle range of $10° \leq 2\theta \leq 120°$ at a step size of 0.02°. The XRD data were analyzed be the Rietveld method using the program RIETAN-FP [34], and the crystal structures were drawn by using the VESTA program package [35].

## 5.2.3 Characterization

The X-ray photoelectron spectrum was measured with an X-ray photoelectron spectrometer (XPS) JPS-9200 (JEOL). The monochromatized Al Kα X-ray source with charge neutralizer was used for performing wide and narrow scans. The wide scan and core-level spectra were recorded in steps of 1 and 0.1 eV, respectively. All peaks to be charge corrected to 285.0 eV using C 1s peak.

The UV-vis diffuse reflectance spectra were measured with a V-570 instrument (JASCO) in the wavelength range of 220-1000 nm.

The temperature dependence of the magnetic susceptibilities were measured with a SQUID magnetometer (Quantum Design, MPMS-5S). The measurements were performed under both zero-field-cooled (ZFC) and field-cooled (FC) conditions over the temperature range between 1.8 and 300 K in an applied magnetic field of 0.1 T. The field dependence of the magnetizations was measured over the magnetic field range between -5 and 5 T at 1.8 K in a zero magnetic field.

The specific heat measurements were reformed using a relaxation technique with a commercial physical property measurement system (Quantum Design, PPMS) in the temperature range of 1.8-300 K. The pelletized sample was mounted on a thin alumina plate with Apiezon N-grease for better thermal contact.

### 5.2.4 DFT calculation

Calculations of the electronic structure and the density of states (DOS) were performed using the WIEN2k program package.[36] This program employs the full−potential linearized augmented plane wave + local orbitals (FP−LAPW+lo) method based on density functional theory (DFT). We used the generalized gradient approximation (GGA) + Hubbard *U* parameter for the Mn 3d electrons. The accurate calculation of band gaps were obtained by using the modified Becke-Johnson exchange potential (mBJ)[37]. In the calculations, the convergence parameter was set to be $R_{MT}k_{max}$ = 7.0, and the muffin−tin (MT) spheres are $R_{MT}$(Sr) = 2.50 bohr, $R_{MT}$(Mn) = 2.38 bohr, $R_{MT}$(Ge) = 1.69 bohr, $R_{MT}$(O) = 1.53 bohr, Sand $R_{MT}$(S) = 1.80 bohr. We used 8 × 8 × 12 meshes with 60 *k* points in the first Brillouin zone (B.Z.).

## 5.3 Results and discussion

### 5.3.1 Crystal structure analysis

The new melilite-type oxysulfide $Sr_2MnGe_2S_6O$ and its Zn analogue $Sr_2ZnGe_2S_6O$ were successfully prepared. They were obtained as gray and white colored polycrystalline samples. The X-ray diffraction (XRD) profiles are shown in Figure 2. The observed peaks were indexed on a tetragonal unit cell ($a$ = 9.5206(2) Å, $c$ = 6.2002(1) Å for $M$ = Mn; $a$ = 9.4311(2) Å, $c$ = 6.1845(1) Å for $M$ = Zn) with the space group $P\text{-}42_1m$, which is typical for the melilite-type compounds[1, 2].

For the structural refinement by the Rietveld analysis, We used a structural model of $Sr_2ZnGe_2S_6O$ determined by Teske[32] as a starting model. In melilite-type compounds $A_2MM'_2X_7$, it is known that there are three cation sites ($A$, $M$, and $M'$). For the $Sr_2MGeS_6O$ compounds, the best results was obtained for the cation arrangement of $A$ = Sr, $M$ = Mn, Zn and $M'$ = Ge which is the same as related oxide-melilites $Sr_2MGe_2O_7$ ($M$ = Mn and Zn)[13]. Thus, the magnetic Mn ions are located at the corner and base-center positions of the unit cell and form a square planer lattice in $ab$ plane. On the other hand, concerning about anions, there exist three crystallographic sites: $X$(1), $X$(2) and $X$(3) (Figure 5.1). We have tried to analyze the data by using four models with different occupations of S and O ions (see Table 5.2 and Table 5.3).

As a result, the best fitting was obtained when the O ions occupy the $X$(1) site and S ions occupy both $X$(2) and $X$(3) sites in an ordered manner. This anion ordering is corresponding to the report for the $Sr_2ZnGe_2S_6O$[32]. The calculated profiles are plotted in Figure 5.2, and the refined structural parameters and reliability factors are summarized in Table 5.4. The coordination environments of three cation sites were shown in Figure 5.3, and the selected interatomic distances and the calculated values of the bond valence sums (BVS) [38, 39] are listed in Table 5.5.

The Mn ion is surrounded by four equivalent S(2) ions, and a $MnS_4$ tetrahedron is formed. The bond length of Mn-S is 2.412(3) Å, which is comparable to the bond length calculated from the Shannon's ionic radii 2.50 Å for $Mn^{2+}$-$S^{2-}$ [40]. On the other hand, the Ge ion is coordinated by four ions: O(1), S(2) and two equivalent S(3), and they formed a distorted $GeS_3O$ tetrahedron. The bond lengths in this tetrahedron are $l_{Ge\text{-}O}$ = 1.810(5) Å, and $l_{Ge\text{-}S}$ = 2.148(4) ~2.204(3) Å. These lengths are very close to from the values of the Shannon's ionic radii 1.77 Å for $Ge^{4+}$-$O^{2-}$ and 2.23 Å for $Ge^{4+}$-$S^{2-}$, respectively. For Sr ion, the $SrS_7O$ polyhedron is formed by O(1), three S(2) and four S(3) ions which is a highly distorted square antiprism. The BVS of cation ions indicates that the oxidation state in a divalent (for Sr and Mn ions) and tetravalent (for Ge ions), which was represented the title compound as $Sr^{2+}{}_2Mn^{2+}Ge^{4+}{}_2S^{2-}{}_6O^{2-}$.

## 5.3.2 XPS analysis

The XPS measurements were carried out to elucidate the electronic states of Mn and Ge ions. Figure 5.4 and Figure 5.5 show the XPS narrow scan spectra for Mn 2p and Ge 2p core levels of $Sr_2MnGe_2S_6O$ and analogues oxide $Sr_2MnGe_2O_7$. The spectra of Mn 2p exhibit strong spin-orbit split features at around 640 eV ($j$ = 3/2) and 653 eV ($j$ = 1/2) which originate from the $2p^53d^6\underline{L}$ final states, where $\underline{L}$ denotes a hole in the O 2p (S 3p) band. The satellites on the high-binding-energy side at ~4.5 eV correspond to the $2p^53d^5$ final states, and their positions and intensities depend on $\Delta$ (charge transfer energy), $U$ (d-d coulombic repulsion energy), and $T$ (ligand p-metal d hybridization strength).[41] By fitting peaks with a Voigt function to these spectra, we obtained the binding energies (BE) and area intensities (see Figure 5). The weighted averages of BE of the main $j$ = 3/2 peaks are estimated to be 640.5 eV for $Sr_2MnGe_2O_7$ and 640.3eV for $Sr_2MnGe_2S_6O$, and these values are consistent with those of other divalent manganese oxides and sulfides.[42 43] For $Sr_2MnGe_2S_6O$, the ratio ($I_s/I_m$ = 0.46) of the intensities of the satellite and main peaks for $j$ = 3/2 increases, and the energy difference ($E_s$ - $E_m$= 4.1 eV) between the satellite and

main peaks decreases in comparison with those ($I_s/I_m$ = 0.31 and $E_s$ - $E_m$= 4.9 eV) for $Sr_2MnGe_2O_7$. This result suggests that $U$ of Mn and $\Delta$ between Mn and S for $Sr_2MnGe_2S_6O$ are smaller than $U$ of Mn and $\Delta$ between Mn and O for $Sr_2MnGe_2O_7$.[41] The decrease in $U$ and $\Delta$ for $Sr_2MnGe_2S_6O$ is consistent with the reported values, i.e. both of $U$ and $\Delta$ are about 7 eV for divalent Mn oxides, and $U$ and $\Delta$ are 5~6 eV and 4 eV, respectively, for divalent Mn sulfides[44]. For $Sr_2MnGe_2S_6O$, BE = 1218.4 eV of Ge 2p is slightly lower than BE = 1218.7 of $Sr_2MnGe_2O_7$. Although the formal oxidation states of the Ge ions are +4 for both of $Sr_2MnGe_2O_7$ and $Sr_2MnGe_2S_6O$, the shift of BE reveals that the partial substitution of S for O decreases slightly the effective oxidation number of Ge, due to a change in bonding character from ionic to covalent[45].

### 5.3.3 Magnetic properties

Figure 5.6 shows the temperature dependence of the reciprocal magnetic susceptibility for $Sr_2MnGe_2S_6O$. The data were fitted by the Curie-Weiss law between 100 and 300 K, using an equation:

$$\chi_M = \frac{C}{T-\theta} + \chi_{TIP} \qquad (5.1)$$

where $C$, $\theta$, and $\chi_{TIP}$ mean the Curie constant, Weiss constant, and temperature-independent paramagnetic susceptibility, respectively. The effective magnetic moment was determined to be 6.03(1) $\mu_B$/Mn, which is close to the spin-only value 5.92 $\mu_B$ expected for the $Mn^{2+}$ ($3d^5$) ion in a high-spin state ($S$ = 5/2). The Weiss constant $\theta$ is -34.3 (1) K, and this negative $\theta$ value indicates that the predominant magnetic interaction between $Mn^{2+}$ ions is antiferromagnetic.

At low temperatures, the magnetic susceptibility shows a broad maximum around 18 K. Such a broad maximum feature is often found in the low-dimensional magnets[46, 47]. In term of the magnetic interaction, the $Sr_2MnGe_2S_6O$ has two super-

superexchange Mn-S(3)-S(3)-Mn pathways for the intralayer ($J$) and interlayer ($J'$) interactions as shown in Figure1. In the case of related oxides $A_2MnGe_2O_7$ ($A$ = Sr, Ba), it is known that the intralayer interaction is much stronger than the interlayer one from the results of the magnetic susceptibility[13] and inelastic neutron scattering experiments[14] . If this fact is common in the oxysulfide $Sr_2MnGe_2S_6O$, the arrangement of $Mn^{2+}$ ions in this compound can also be regarded as the 2D square-planar lattice. Therefore, we tried to fit the observed magnetic susceptibility by using a model for this lattice. For that purpose, the high-temperature series (HTS) expansion of the square-planar lattice for the Heisenberg model was used,

$$\chi_{\mathrm{s.p}} = \frac{N_{\mathrm{A}} g^2 \mu_{\mathrm{B}}^2 S(S+1)}{3k_{\mathrm{B}}T} \sum a_{\mathrm{n}} \left(J / k_{\mathrm{B}}T\right)^n \tag{5.2}$$

where $N_A$, $g$, $\mu_B$, $k_B$ and $J$ are the Avogadro constant, $g$ factor, Boltzmann constant, Bohr magneton, exchange integral (intralayer), respectively. We use the coefficients $a_n$ (n= 1-8) given in previous results[48–51]. The fitting equation was obtained by applying the Padé approximation ([4, 4] Padé) to eq (5.2). Additionally, to consider the interlayer interaction, the observed magnetic susceptibility (15 K – 300 K) was fitted by using eq (5.3):

$$\chi = \frac{\chi_{\mathrm{s.p}}}{1 - \left( \frac{2z'J'}{N_{\mathrm{A}} g^2 \mu_{\mathrm{B}}^2 S(S+1)} \right) \chi_{\mathrm{s.p}}} \tag{5.3}$$

where $z'$ and $J'$ are the number of magnetic nearest-neighbors ($z'$ = 2) and exchange integral (interlayer). Finally, we calculated the $g$ factor, $J$ and $J'$ as fitting parameters. The calculation result is shown in Figure 5.6 as a solid blue line, and it is in good agreement with the experimental data. The $g$ factor of the $Mn^{2+}$ ion, the values of $J$, and $J'$ are determined to be 1.99(1), -1.03(1) K, and -0.35(3) K, respectively. The effective magnetic moment $\mu_{\mathrm{eff}}$ and the Weiss constant $\theta$ were calculated to be 5.89 $\mu_B$ and -28.1 K respectively, from the equations $\mu_{\mathrm{eff}} = g[S(S+1)]^{1/2}$ and $\theta = \sum_i 2zJ_iS(S+1)/3k_B$ where $z$

= 4 (the number of magnetic nearest-neighbors for intralayer interaction). These values are comparable to those estimated from the Curie-Weiss law (6.03 $\mu_B$ and -34.3 K). This fitting indicates that the $Sr_2MnGe_2S_6O$ shows a two-dimensional behavior despite the shorter Mn-Mn distance along the *c* axis (6.20 Å) compared with that in the *ab* plane (6.73 Å). The magnitude of *J* and *J'* values are larger than those of analogous oxides: $Ba_2MnGe_2O_7$ ($J$ = -0.323 K, $J'$ = -0.0012 K, $J'/J$ = 0.0037)[52] and $Sr_2MnGe_2O_7$ ($J$ = -0.34 K, $J'$ = -0.07 K, $J'/J$ = 0.205)[8]. This result indicates that the magnetic interactions are enhanced due to substituting the $S^{2-}$ ion for $O^{2-}$ ion; while the lager $J'/J$ ratio (0.340) in oxysulfide shows thath the two-dimensionality is weaker than that in oxides.

Figure 5.7(b), (c) show the temperature dependence of the specific heat for $Sr_2MnGe_2S_6O$. The data show a λ-type anomaly at 15.5 K ($T_N$) indicating the occurrence of the long-range AFM ordering of $Mn^{2+}$ ions. This $T_N$ is much higher than that of oxide analogues $Sr_2MnGe_2O_7$ (4.4 K)[13]. This fact also supports the enhancement in the magnetic interaction by substitution sulfide ion for oxide ion.

The magnetic entropy ($S_{mag}$) due to the magnetic ordering was calculated by using $S_{mag} = \int_0^T C_{mag} / TdT$ , in which the magnetic specific heat ($C_{mag}$) was estimated by subtracting the lattice and electronic specific heat from the experimental specific heat of $Sr_2MnGe_2S_6O$. For the lattice and electronic contributions, we used the specific heat of a nonmagnetic and isostructural compound $Sr_2ZnGe_2S_6O$. The magnetic specific heat below 1.8 K was extrapolated by the relation $C_{mag} \propto T^3$ from the spin-wave model for an antiferromagnet[53]. The temperature dependence of the magnetic specific heat divided by temperature ($C_{mag} / T$) and magnetic entropy ($S_{mag}$) are plotted in Figure 5.7(c). The $S_{mag}$ value reaches 13.16 J $mol^{-1}$ $K^{-1}$ at 50 K, which is close to the theoretical value $R$ ln(2$S$+1) = $R$ ln 6 = 14.90 J $mol^{-1}$ $K^{-1}$ ($R$ = gas constant). This result shows that the observed magnetic transition is due to the long-range AFM ordering of the $Mn^{2+}$ ion in a high-spin configuration with $S$ = 5/2.

Figure 5.8 shows the field dependence of the magnetization for $Sr_2MnGe_2S_6O$ measured at 1.8 K. The magnetization of $Sr_2MnGe_2S_6O$ increases linearly and corresponding to that this compound has an AFM ordered ground state.

## 5.3.4 DFT calculation

Figure 5.9 shows the UV-vis diffuse reflectance spectra of $Sr_2MnGe_2S_6O$ and related oxide $Sr_2MnGe_2O_7$. The absorption values were calculated from the reflectance data using the Kubelka Munk function given by

$$F(R_\infty) = \frac{(1-R_\infty)^2}{2R_\infty}, \tag{5.4}$$

where $R_\infty$ is the reflectance[54]. The energy of the optical band gap was determined using the Tauc plot[55]. The optical band gaps were determined to be 3.2 eV for $Sr_2MnGe_2S_6O$ and 3.5 eV for $Sr_2MnGe_2O_7$ as shown in Figure 5.9. In this compound, the photon energy ($h\nu$) is proportional to $(F(R_\infty)h\nu)^2$ near the bottom of the conduction band. This band gap is close to the optical band gaps (~3.1 eV) of the manganese sulfides α-, β- and γ-MnS[56,57].

In order to discuss chemical bonding, we carried out the DFT calculation. Figure 5.10 displays the total densities of states (DOS) and the partial DOS of total electrons of Sr, Mn, Ge, O, and S for (a)related oxide $Sr_2MnGe_2O_7$ and (b)$Sr_2MnGe_2S_6O$. In the DFT calculations of insulators with strongly correlated electrons, the energy of the band gap is very sensitive to the Hubbard $U$ parameter. Thus, we have attempted to estimate the band gap ($E_g$) by varying the $U$ parameter from 4 eV to 8 eV. However, the values of $E_g$ are almost constant (~2.6 eV for $Sr_2MnGe_2O_7$ and ~2.2 eV for $Sr_2MnGe_2S_6O$) due to the contribution of Ge 3s and 3d orbitals, that are independent of $U$, to the conduction band, and we cannot determine the $U$ parameter. Thus we have adopted 7 eV for $Sr_2MnGe_2O_7$ and 4 eV for $Sr_2MnGe_2S_6O$ as an effective Coulomb interaction $U_{eff}$ of Mn. The final

accurate band gaps were obtained by using the mBJ calculations. The occupied and unoccupied bands form a band gap of 3.4 eV for $Sr_2MnGe_2O_7$ and 2.4 eV for $Sr_2MnGe_2S_6O$ around the Fermi level. This value for $Sr_2MnGe_2S_6O$ is smaller than the optical band gap of the UV-vis spectra, and this underestimation is generally shown in the band gaps obtained by the DFT calculation. The valence band of $Sr_2MnGe_2S_6O$ demonstrates a strong hybridization between the Mn d and S(3) 3p orbitals in the broad range from -4.5 eV to 0 eV, while the top of the valence band in the narrow range between -1.3 eV to 0 eV mainly consists of the Mn d orbitals for $Sr_2MnGe_2O_7$. The energy levels for $Sr_2MnGe_2O_7$ indicate that this compound is classified in a Mott-Hubbard insulator[44]. Because the spin-up d orbitals are located below the $E_F$ level and the spin-down d orbitals exist above the $E_F$ level, the results reveal that the Mn ions are in the divalent state with the high-spin configuration and that both compounds have the magnetic moments of 4.4 $\mu_B$ per Mn atom.

Figure 5.11 shows the partial DOS of the Mn 3d orbitals of $Sr_2MnGe_2O_7$ and $Sr_2MnGe_2S_6O$. The $d_{xy}$ and $d_{x2-y2}$ orbitals are delocalized at the top of the Mn spin-up states of $Sr_2MnGe_2O_7$. On the other hand, the DOS of $Sr_2MnGe_2S_6O$ indicate that the spin-up $d_{xz}$ and $d_{yz}$ orbitals are located over the whole of S(3) p bands and split up into peaks just below $E_F$ and in the range between -4.5 and -3 eV, forming a bonding/antibonding gap due to the strong p-d bondings. This is caused by the difference in the energy levels of the O 2p and S 3p orbitals. The participation of the $d_{xz}$ and $d_{yz}$ orbitals is derived from the elongation of the $MnS_4$ tetrahedron along the *c*-axis and should play a key role in superexchange and super-superexchange interactions. The 3D AFM ordering temperature (15.5 K) and the interactions $J$ and $J'/J$ for $Sr_2MnGe_2S_6O$ are considerably larger than those of other melilite type oxides. In general, the superexchange interaction strongly depends on the magnetic moment ($S$) and the $U$ and $\Delta$ energies, and the increase of $S$ and the decrease of $\Delta$ enhance the superexchange interaction[44]. For the rock-salt type Mn$X$ ($X$ = O, S, Se, Te) and pyrite type Mn$X_2$ ($X$ = S, Se, Te) compounds with $S$ = 5/2, the 3D AFM temperatures ($T_N$) increase in the order of O, S, Se and Te for

Mn$X$ [58] and S, Se and Te for Mn$X_2$ [59, 60] with increasing covalent character between Mn and ligand. In the case of $Sr_2MnGe_2S_6O$, the strong p-d hybridizations reduce the $\Delta$ energy and enhance the super-superexchange interactions $J$ via the $d_{xz}$ + $d_{yz}$ - S(3) 3p - S(3) 3p - $d_{xz}$ + $d_{yz}$ orbitals as compared with the super-superexchange interactions for other melilite type oxides. The enhancement of the interlayer interaction $J'/J$ should also be derived from the contribution of the $d_{xz}$ + $d_{yz}$, showing the high 3D AFM temperature.

## 5.4 Summery

We here report on results of synthesis, crystal structures and magnetic properties of new melilite-type oxysulfides $Sr_2MnGe_2S_6O$. This compound crystallizes in a tetragonal melilite-type structure with space group $P$-42$_1m$. In this structure, the $S^{2-}$ and $O^{2-}$ ions occupy different crystallographic sites in an ordered manner. The temperature dependence of magnetic susceptibility shows a broad maximum due to a two-dimensional magnetic interaction between Mn ions in the *ab*-plane and an AFM transition at 15.5 K. Observed higher transition temperature and lager $J$ and $J'$ values than those for oxide analogue indicate that the magnetic interactions between $Mn^{2+}$ ions are enhanced by the substitution of $O^{2-}$ for $S^{2-}$.

## 5.5 Tables and figures

Table 5.1 Magnetic properties of melilite type compounds.

| Compounds | Space group | $T_N$(K) | Magnetic properties | Ref |
|---|---|---|---|---|
| $Sr_2MnSi_2O_7$ | $P\text{-}42_1m$ | 3.4 | Antiferromagnet | [7 8,] |
| $Ca_2CoSi_2O_7$ | $P\text{-}42_1m$ | 5.7 | Antiferromagnet, multiferroic behavior | [6,9–11] |
| $Sr_2CoSi_2O_7$ | $P\text{-}42_1m$ | ≈ 7 | Antiferromagnet, multiferroic behavior | [6] |
| $Ba_2CoSi_2O_7$ | $C2/c$ | ≈ 5 | Antiferromagnet, multiferroic behavior | [9,12] |
| $Sr_2MnGe_2O_7$ | $P\text{-}42_1m$ | 4.4 | Antiferromagnet, $k$ = (0, 0, 1/2) | [13] |
| $Sr_2CoGe_2O_7$ | $P\text{-}42_1m$ | 6.5 | Antiferromagnet, $k$ = (0, 0, 0) | [13] |
| $Ba_2MnGe_2O_7$ | $P\text{-}42_1m$ | 4.66 | 2D-AFM, $k$ = (0, 0, 1/2) | [14,15] |
| $Ba_2CoGe_2O_7$ | $P\text{-}42_1m$ | 6.7 | 2D-AFM, $k$ = (0, 0, 0), multiferroic behavior | [6,15–19] |
| $Ba_2CuGe_2O_7$ | $P\text{-}42_1m$ | 3.26 | 2D-spiral AFM, incommensurate - commensurate transition | [15,20–23] |
| $Ln_2GeBe_2O_7$ | $P\text{-}42_1m$ | - | $Ln$ =Y, La, Pr, Sm, Gd, Dy, paramagnet ($T$ > 5 K) | [24] |
| $Eu_2MgSi_2O_7$ | $P\text{-}42_1m$ | - | Paramagnet ($T$ > 1.8 K) | [8] |
| $Eu_2MnSi_2O_7$ | $P\text{-}42_1m$ | 10.7 | Ferrimagnet | [8] |

Table 5.2 The reliability factors of Rietveld analyses for $Sr_2MnGe_2S_6O$ with different O/S ion occupations.

| Model | $R_{wp}$ (%) | $R_B$ (%) | Occupancy of O/S ion and $B$ (Å$^2$) for three anion sites | | |
|---|---|---|---|---|---|
| | | | $X$(1) 2$c$ site | $X$(2) 4$e$ site | $X$(3) 8$f$ site |
| 1 (text) | 9.92 | 2.36 | 1.0 / 0.0, *1.00(31)* | 0.0 / 1.0 *0.99(8)* | 0.0 / 1.0 *0.99(6)* |
| 2 | 12.50 | 4.87 | 0.0 / 1.0, *27(1)* | 0.5 / 0.5 *-2.00(8)* | 0.0 / 1.0 *0.74(7)* |
| 3 | 10.79 | 2.88 | 0.0 / 1.0, *14.2 (2)* | 0.0 / 1.0 *0.75(8)* | 0.25 / 0.75 *-0.22(6)* |
| 4 | 11.05 | 3.39 | 0.144 / 0.856, *16.0(6)* | 0.143 / 0.857 *0.08(8)* | 0.143 / 0.857 *0.22(6)* |

*Note.* Model 1: the O ions occupy only the $X$(1) site. (the final result in the text); model 2: $X$(2) site, model 3: $X$(3) site; model 4: fully disordered arrangement between O and S.

Table 5.3 The reliability factors of Rietveld analyses for $Sr_2ZnGe_2S_6O$ with different O/S ion occupations.

| Model | $R_{wp}$ (%) | $R_B$ (%) | Occupancy of O/S ion and $B$ (Å$^2$) for three anion sites | | |
|---|---|---|---|---|---|
| | | | $X$(1) 2$c$ site | $X$(2) 4$e$ site | $X$(3) 8$f$ site |
| 1 (text) | 9.92 | 2.36 | 1.0 / 0.0, *1.00(31)* | 0.0 / 1.0 *0.99(8)* | 0.0 / 1.0 *0.99(6)* |
| 2 | 9.96 | 2.49 | 0.0 / 1.0, *25.9(7)* | 0.5 / 0.5 *1.9(1)* | 0.0 / 1.0 *0.86(6)* |
| 2 | 9.80 | 2.53 | 0.0 / 1.0, *28.6(7)* | 0.5 / 0.5 *1.07(8)* | 0.0 / 1.0 *1.60(8)* |
| 4 | 10.45 | 2.61 | 0.143 / 0.857, *22.1(7)* | 0.143 / 0.857 *0.41(8)* | 0.143 / 0.857 *0.08(6)* |

*Note.* Model 1: the O ions occupy only the $X$(1) site. (the final result in the text); model 2: $X$(2) site, model 3: $X$(3) site; model 4: fully disordered arrangement between O and S.

Table 5.4 Structural parameters for $Sr_2MGe_2S_6O$ ($M$ = Mn, Zn).

| Atom | Site | $x$ | $y$ | $z$ | $B$ (Å$^2$) |
|---|---|---|---|---|---|
| $Sr_2MnGe_2S_6O$[a] | | | | | |
| Sr | 4*e* | 0.1572(1) | 0.6572 | 0.5069(2) | 1.02(3) |
| Mn | 2*a* | 0 | 0 | 0 | 1.11(7) |
| Ge | 4*e* | 0.6252(1) | 0.1252 | 0.9116(2) | 0.65(4) |
| O(1) | 2*c* | 0 | 1/2 | 0.1946(18) | 1.00(31) |
| S(2) | 4*e* | 0.6352(3) | 0.1352 | 0.2573(5) | 0.99(8) |
| S(3) | 8*f* | 0.0608(3) | 0.1809(3) | 0.2557(4) | 0.99(6) |
| $Sr_2ZnGe_2S_6O$[b] | | | | | |
| Sr | 4*e* | 0.1585(1) | 0.6585 | 0.5009(2) | 1.18(3) |
| Zn | 2*a* | 0 | 0 | 0 | 1.24(6) |
| Ge | 4*e* | 0.6277(1) | 0.1277 | 0.9224(2) | 0.92(4) |
| O(1) | 2*c* | 0 | 1/2 | 0.1969(16) | 0.98(28) |
| S(2) | 4*e* | 0.6350(2) | 0.1350 | 0.2680(4) | 0.98(7) |
| S(3) | 8*f* | 0.0631(2) | 0.1764(2) | 0.2446(4) | 0.98(5) |

*Note* :

[a] Space group $P\text{-}42_1m$ (No. 113), $Z = 2$, $a = 9.5206(2)$ Å, $c = 6.2002(1)$ Å, $V = 561.99(2)$ Å$^3$, $R_{wp} = 9.92$ %, $R_p = 7.11$ %, $R_B = 2.36$ %, $R_F = 1.29$ %.

[c] Space group $P\text{-}42_1m$ (No. 113), $Z = 2$, $a = 9.4311(2)$ Å, $c = 6.1845(1)$ Å, $V = 550.09(2)$ Å$^3$, $R_{wp} = 8.92$ %, $R_p = 5.98$ %, $R_B = 1.53$ %, $R_F = 0.90$ %.

Table 5.5 Selected interatomic distances (Å) and bond valence sums.

| Cation sites | $Sr_2MnGe_2S_6O$ | $Sr_2ZnGe_2S_6O$ | Anion sites | $Sr_2MnGe_2S_6O$ | $Sr_2ZnGe_2S_6O$ |
|---|---|---|---|---|---|
| Sr-O(1) | 2.868(9) | 2.830(7) | O(1)-Ge x2 | 1.809(5) | 1.856(4) |
| Sr-S(3) × 2 | 3.018(3) | 3.050(3) | O(1)-Sr x2 | 2.869(8) | 2.830(6) |
| Sr-S(3)'x2 | 3.071(3) | 3.066(3) | BVS: O(1) | 1.95 | 1.79 |
| Sr-S(2) | 3.151(3) | 3.107(2) | S(2)-Ge | 2.148(3) | 2.139(3) |
| Sr-S(2)' | 3.151(16) | 3.124(1) | S(2)-Sr x2 | 3.151(3) | 3.124(2) |
| Sr-S(2)'' | 3.195(3) | 3.124(3) | S(2)-Sr' | 3.195(4) | 3.107(3) |
| **BVS: Sr** | **1.94** | **1.99** | **BVS: S(2)** | **1.83** | **1.95** |
| *M*-S(2) | 2.412(3) | 2.326(3) | S(3)-Ge | 2.204(3) | 2.203(2) |
| **BVS: *M*** | **2.38** | **2.11** | S(3)-*M* | 2.412(2) | 2.326(2) |
| Ge-O(1) | 1.810(5) | 1.856(4) | S(3)-Sr | 3.018(2) | 3.050(2) |
| Ge-S(2) | 2.148(4) | 2.139(3) | S(3)-Sr | 3.071(3) | 3.066(3) |
| Ge-S(3) x2 | 2.204(3) | 2.203(3) | **BVS: S(3)** | **2.214** | **2.09** |
| **BVS : Ge** | **4.12** | **4.06** | | | |

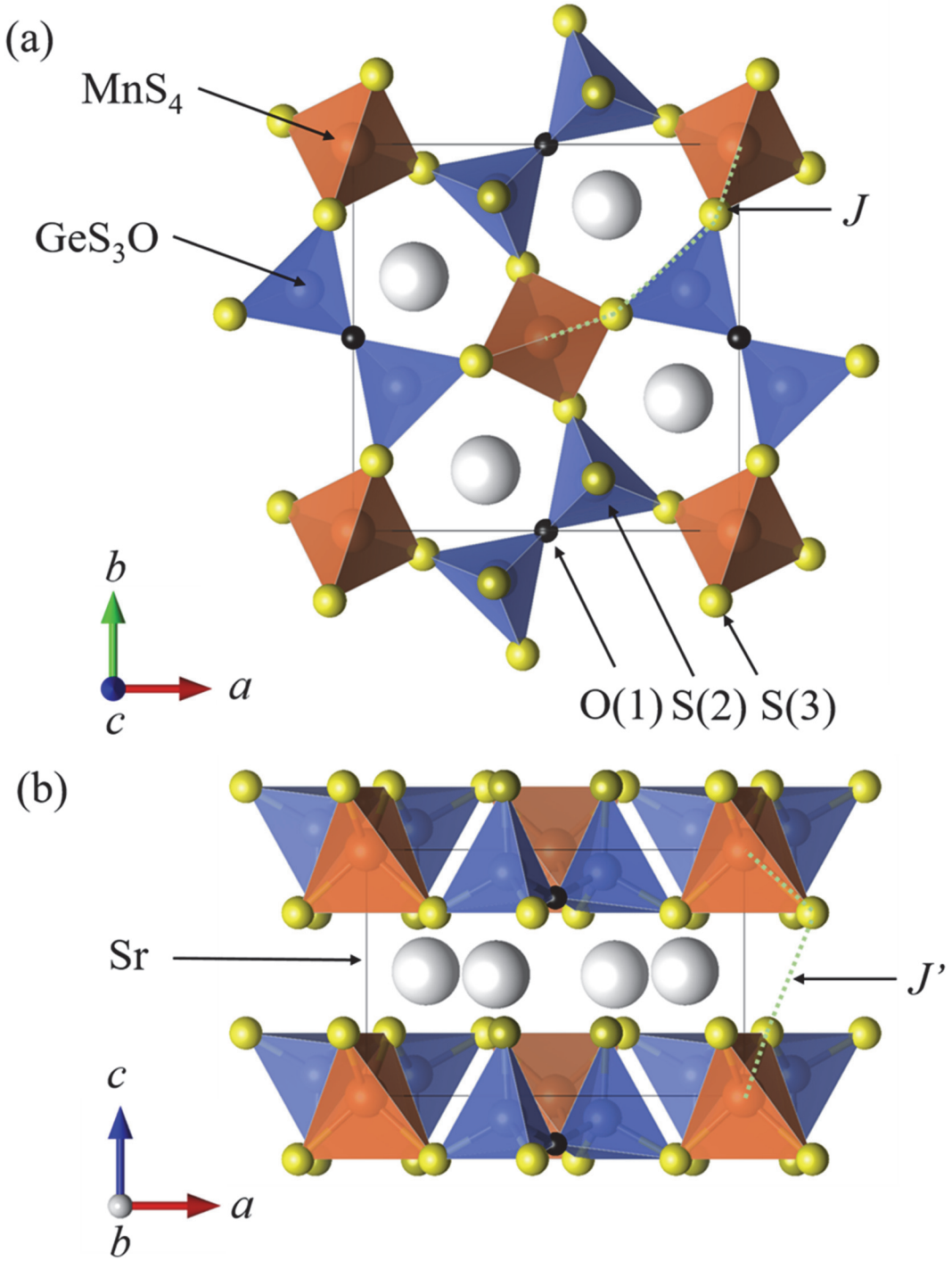


Figure 5.1 Schematic crystal structures of melilite-type compounds $Sr_2MGe_2S_6O$ ($M$ = Mn, Zn): (a) viewed from the c axis, (b) projection of the structure in *ac* plane. The $J$ and $J'$ are super-superexchange pathways (see text).

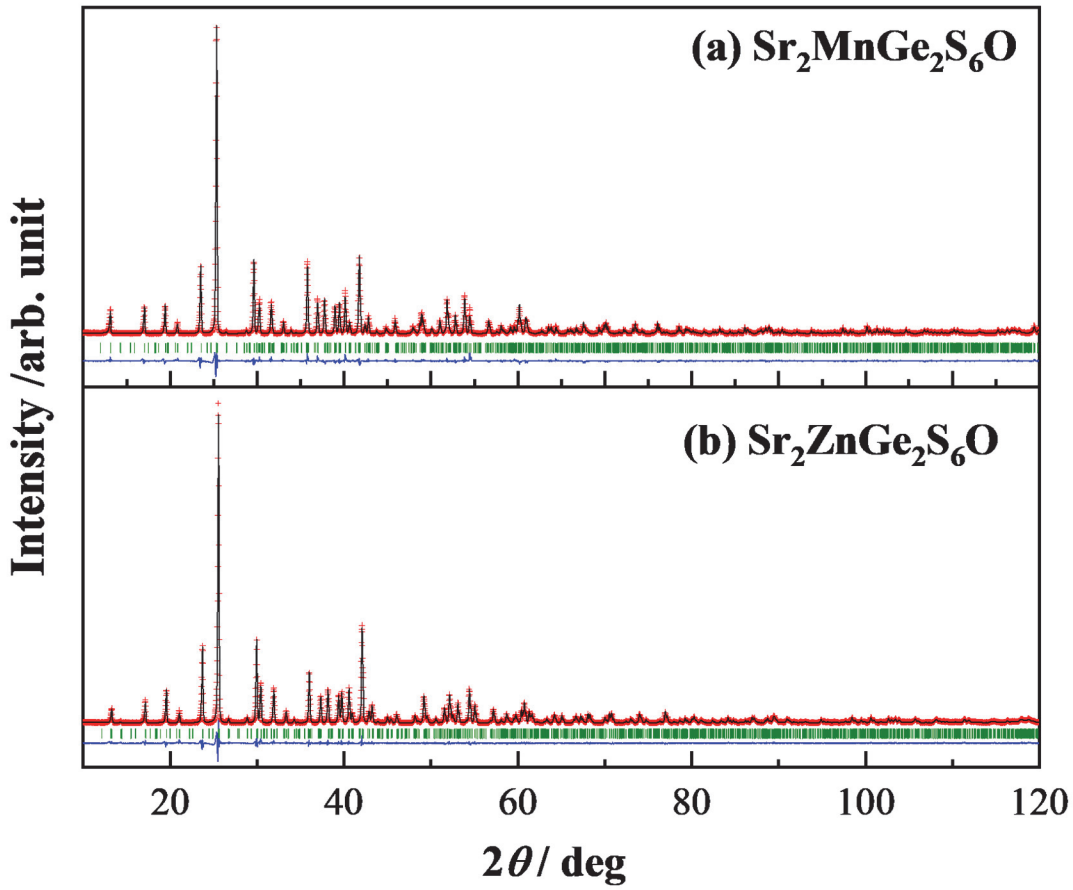


Figure 5.2 Powder XRD profiles for (a) $Sr_2MnGe_2S_6O$, (b) $Sr_2ZnGe_2S_6O$. The calculated and observed profiles are shown as the top black solid line and red markers, respectively. The vertical marks in the middle show positions calculated for Bragg reflection. The lower trace is a plot of the difference between calculated and observed intensities.

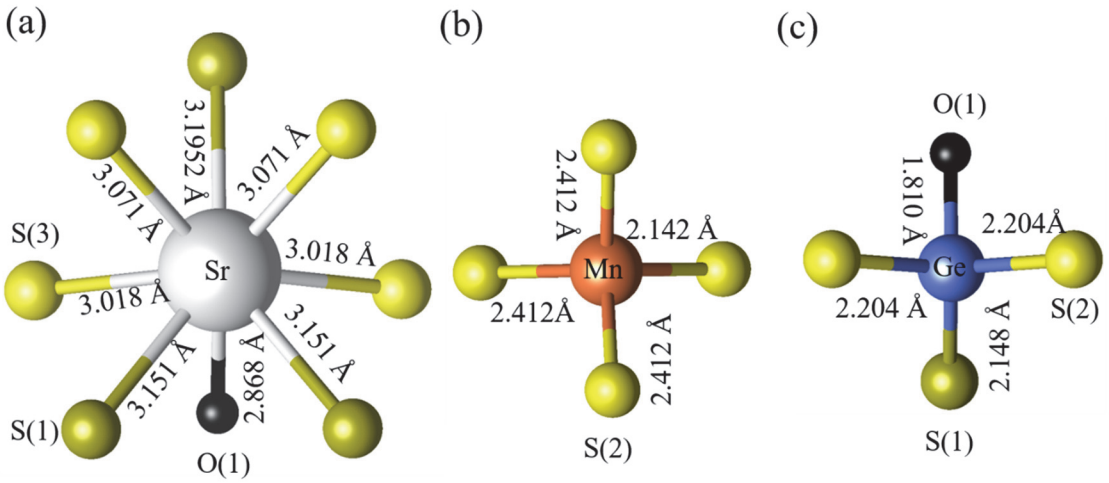


Figure 5.3 Schematic environment of the cation sites coordination for (a)Sr, (b)Mn and (c)Ge sites, respectively.

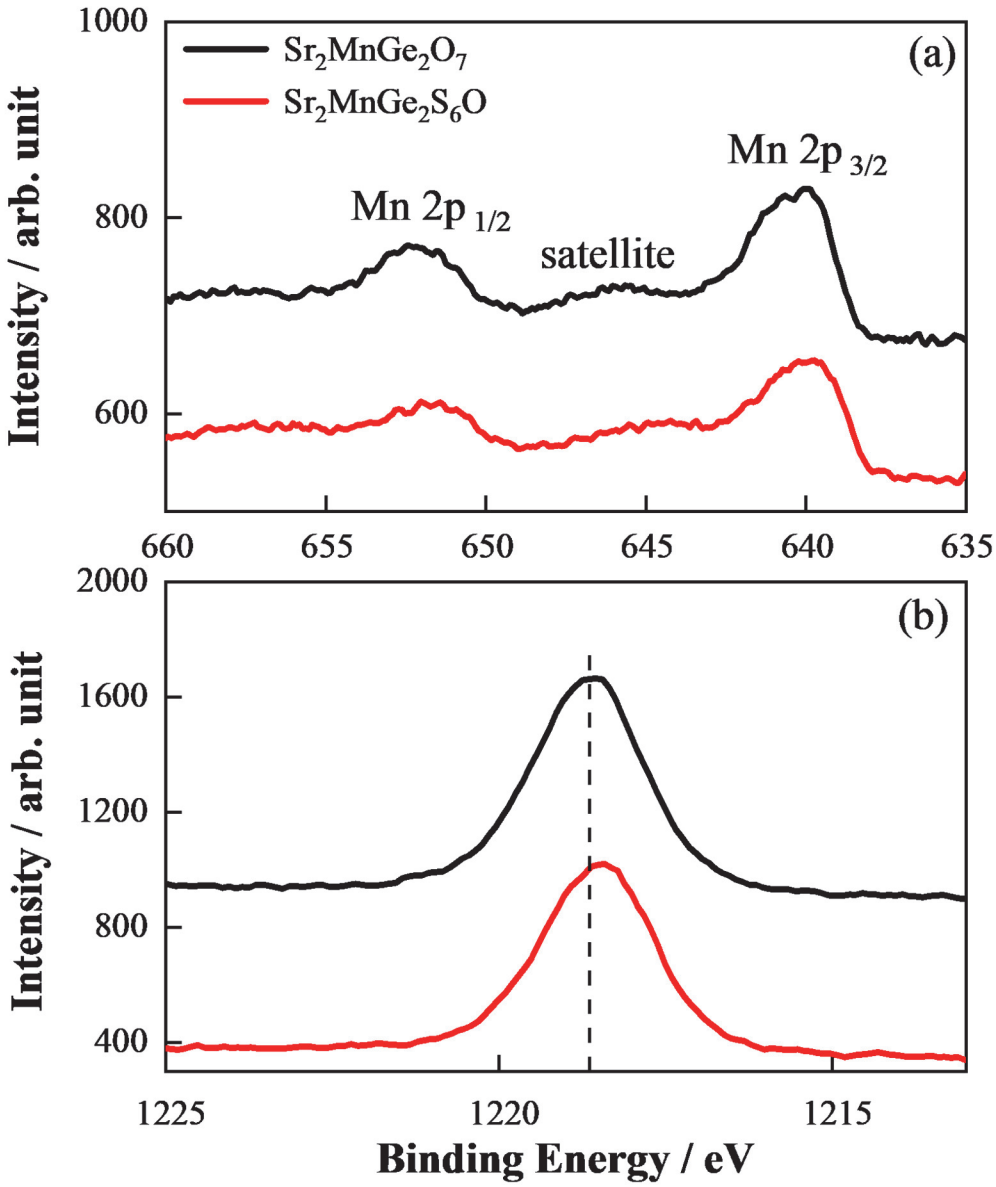


Figure 5.4 XPS spectra of (a)Mn 2p, (b)Ge 5d narrow scan for $Sr_2MnGe_2O_7$ and $Sr_2MnGe_2S_6O$.

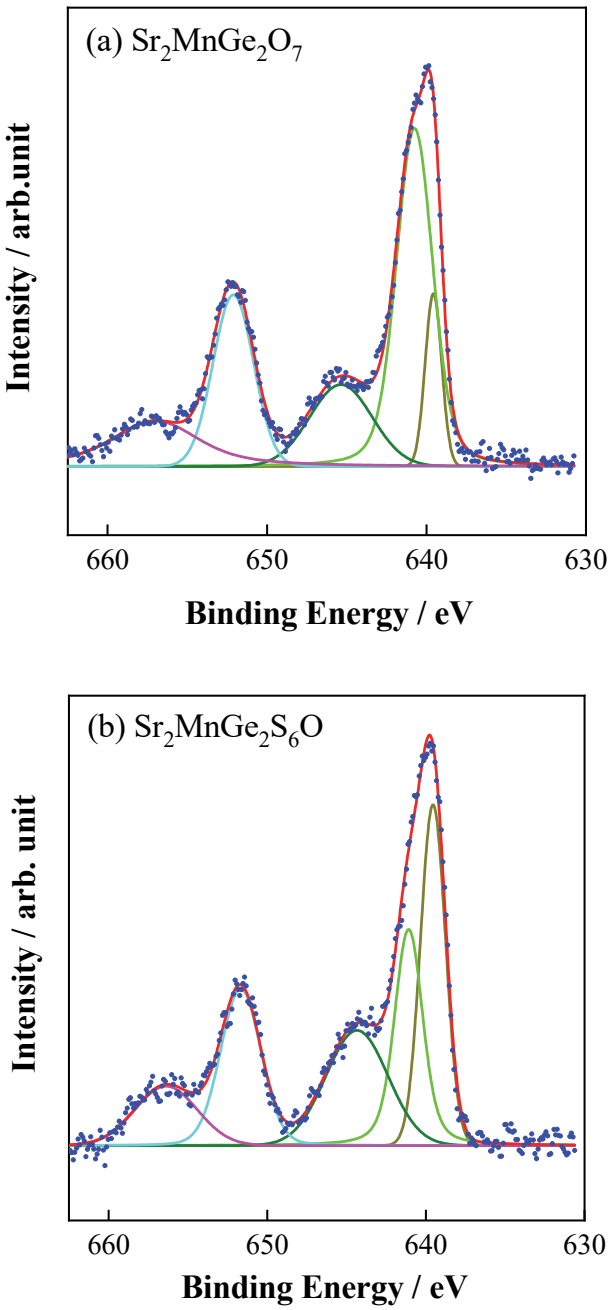


Figure 5.5 Waveform separation of Mn 2p spectra for (a) $Sr_2MnGe_2O_7$ and (b)$Sr_2MnGe_2S_6O$.

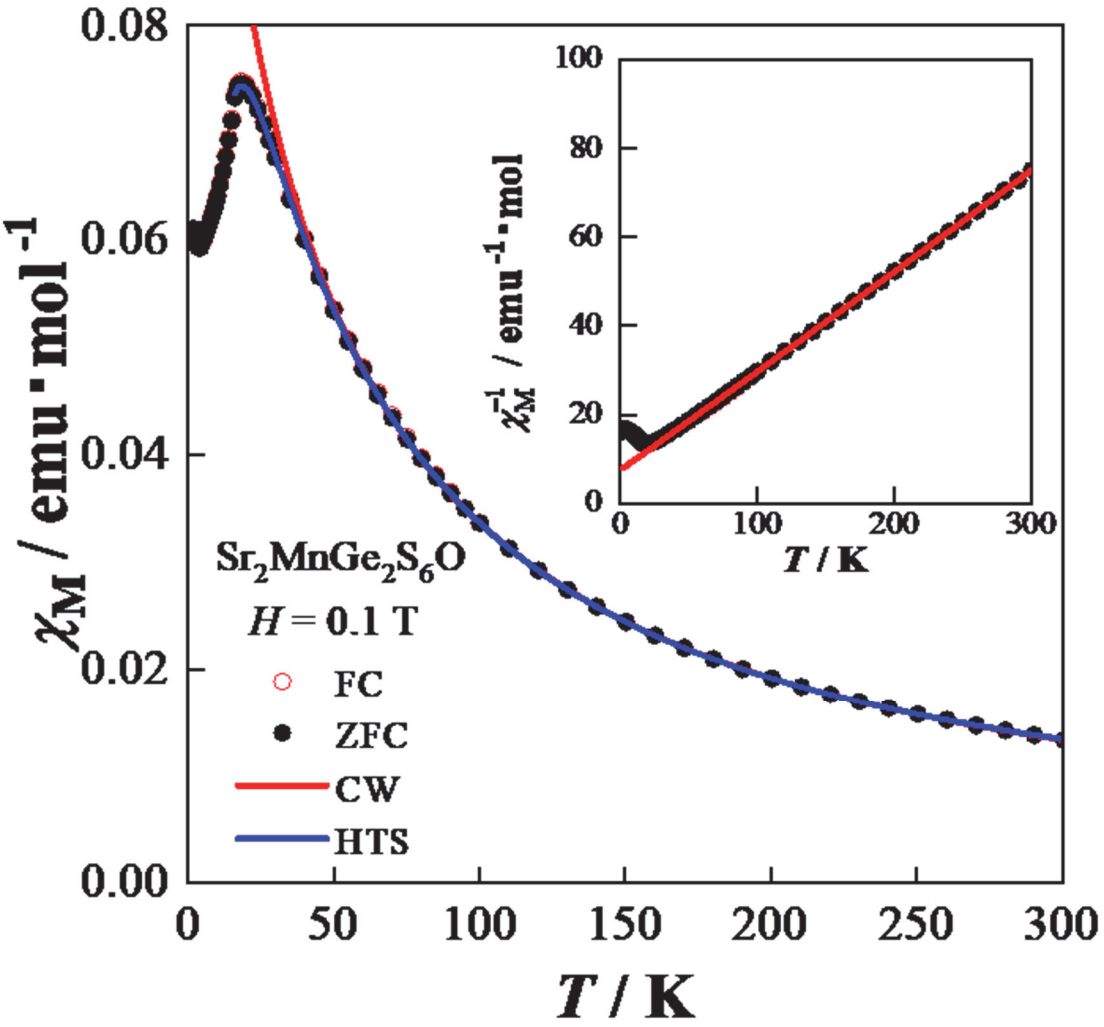


Figure 5.6 Temperature dependence of the magnetic susceptibility of $Sr_2MnGe_2S_6O$. The red and blue solid lines are fitting results by the Curie-Weiss law (CW) and the high-temperature series (HTS) expansion for a square-planar lattice, respectively. The inset shows the reciprocal magnetic susceptibility of $Sr_2MnGe_2S_6O$.

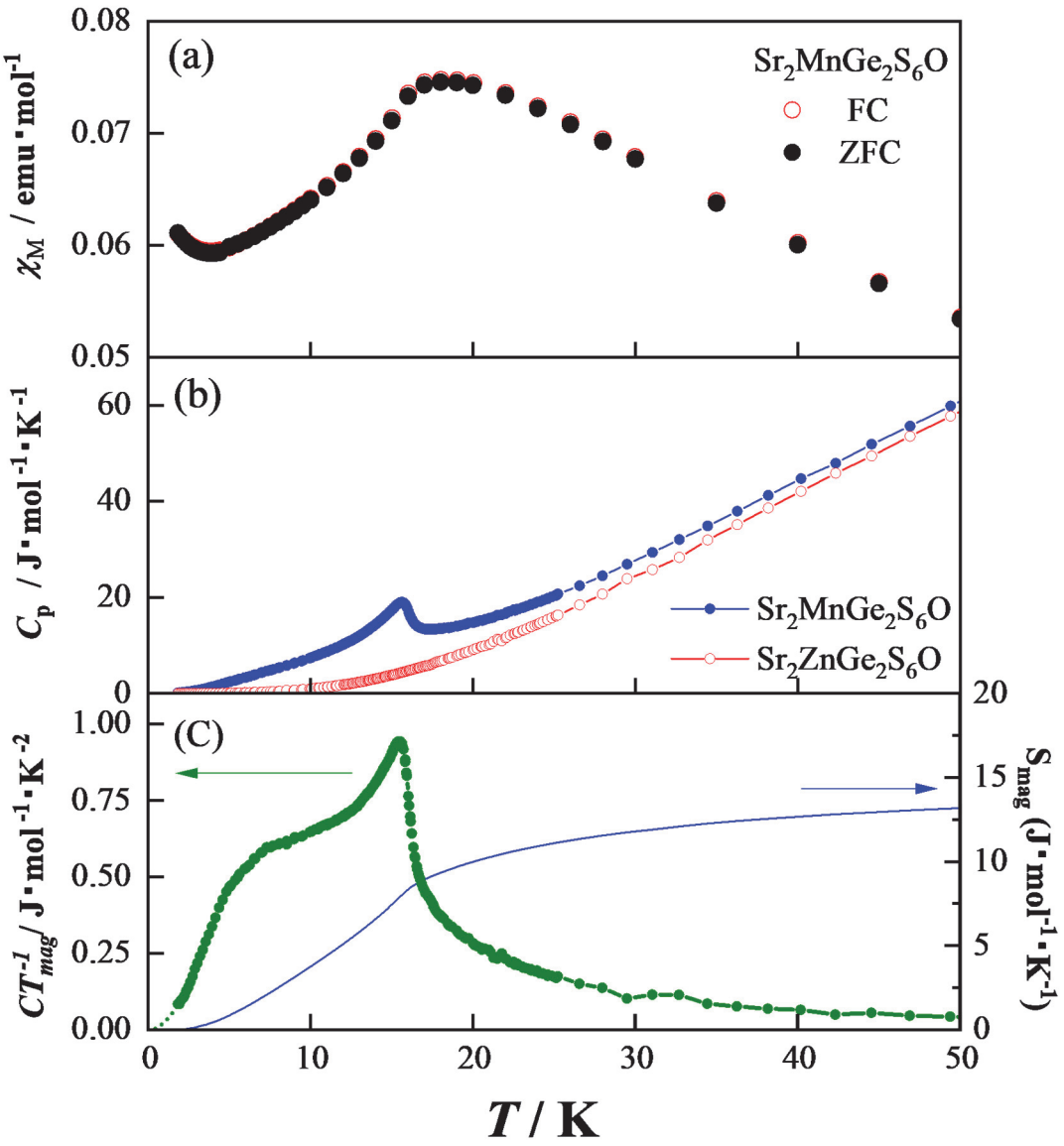


Figure 5.7 Temperature dependence of (a) magnetic susceptibility, (b) specific heat($C_p$), (c) magnetic specific heat divided by temperature ($C_{mag}/T$), and magnetic entropy of $Sr_2MnGe_2S_6O$.

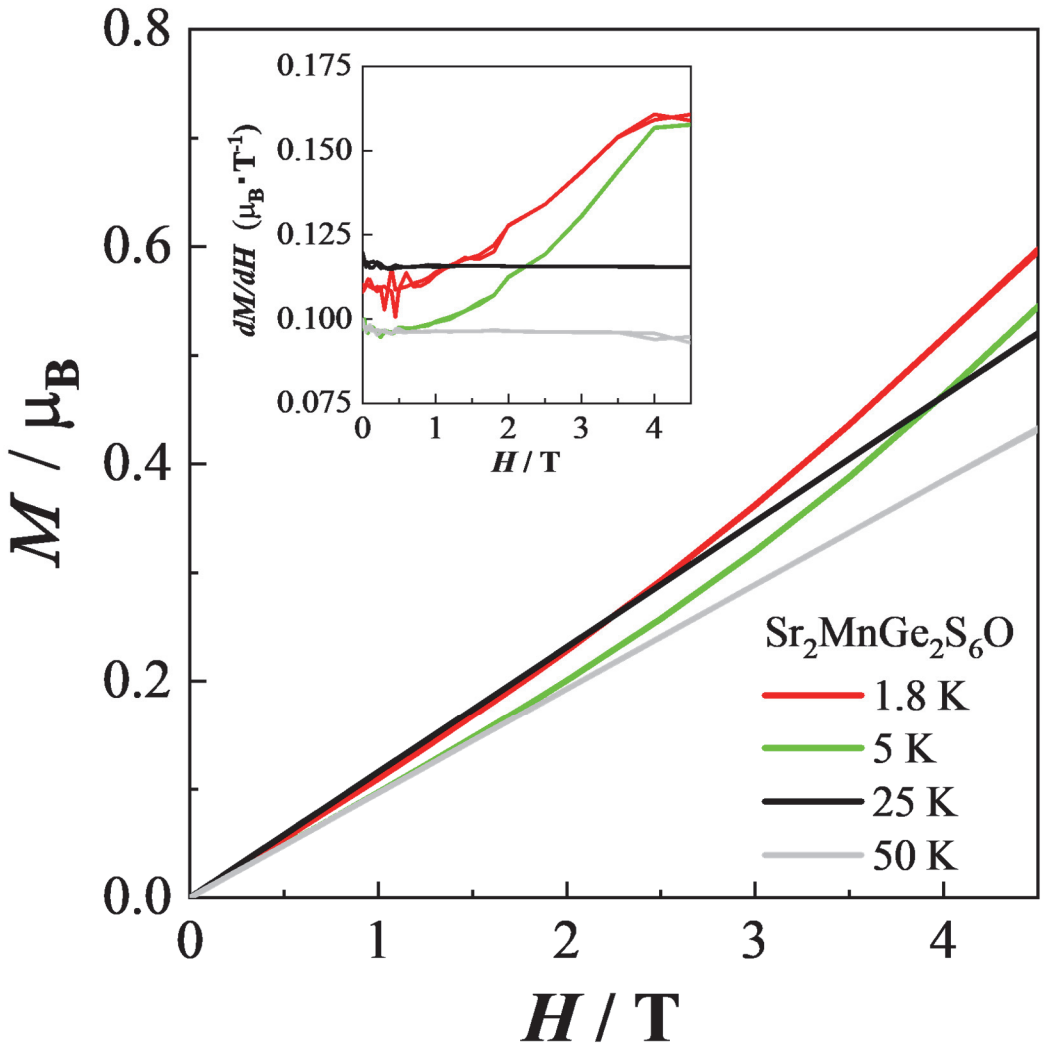


Figure 5.8 Field dependence of the magnetization for $Sr_2MnGe_2S_6O$.

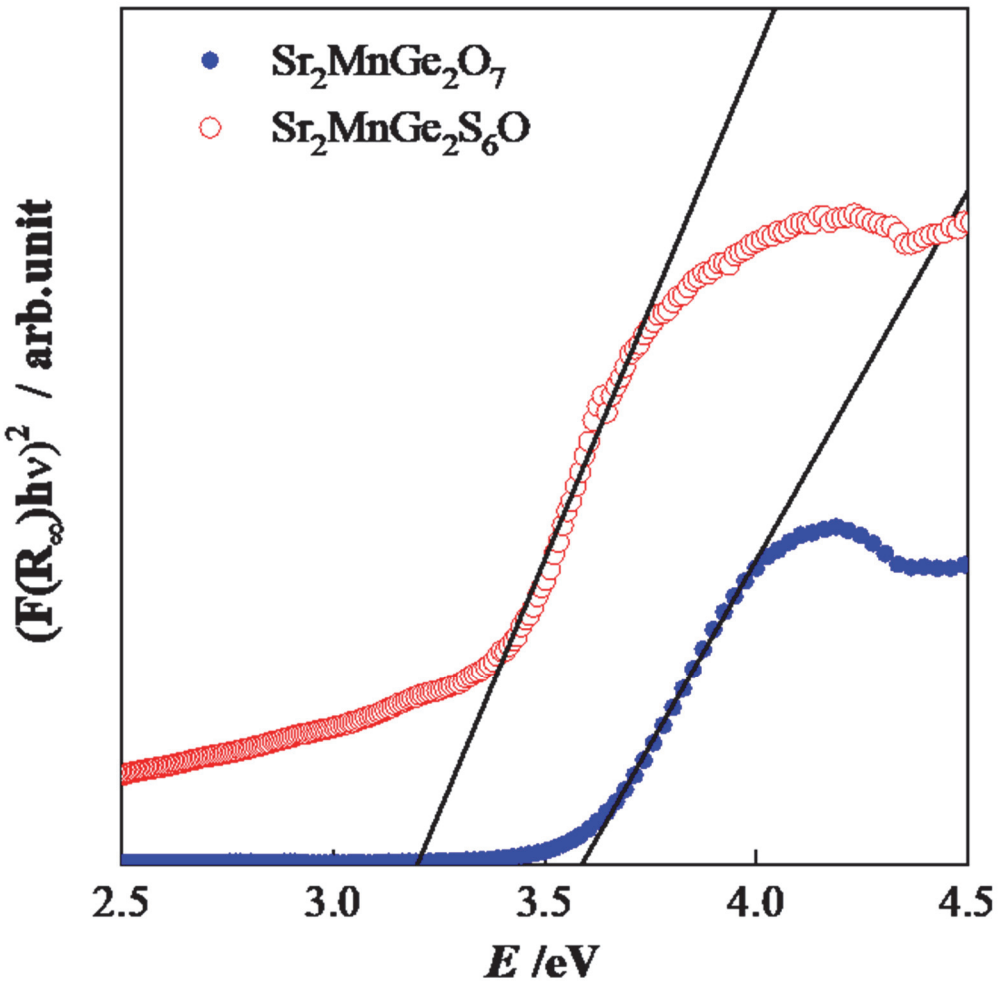


Figure 5.9 Diffuse reflectance spectra of $Sr_2MnGe_2S_6O$ and $Sr_2MnGe_2O_7$. The tauc plot is shown.

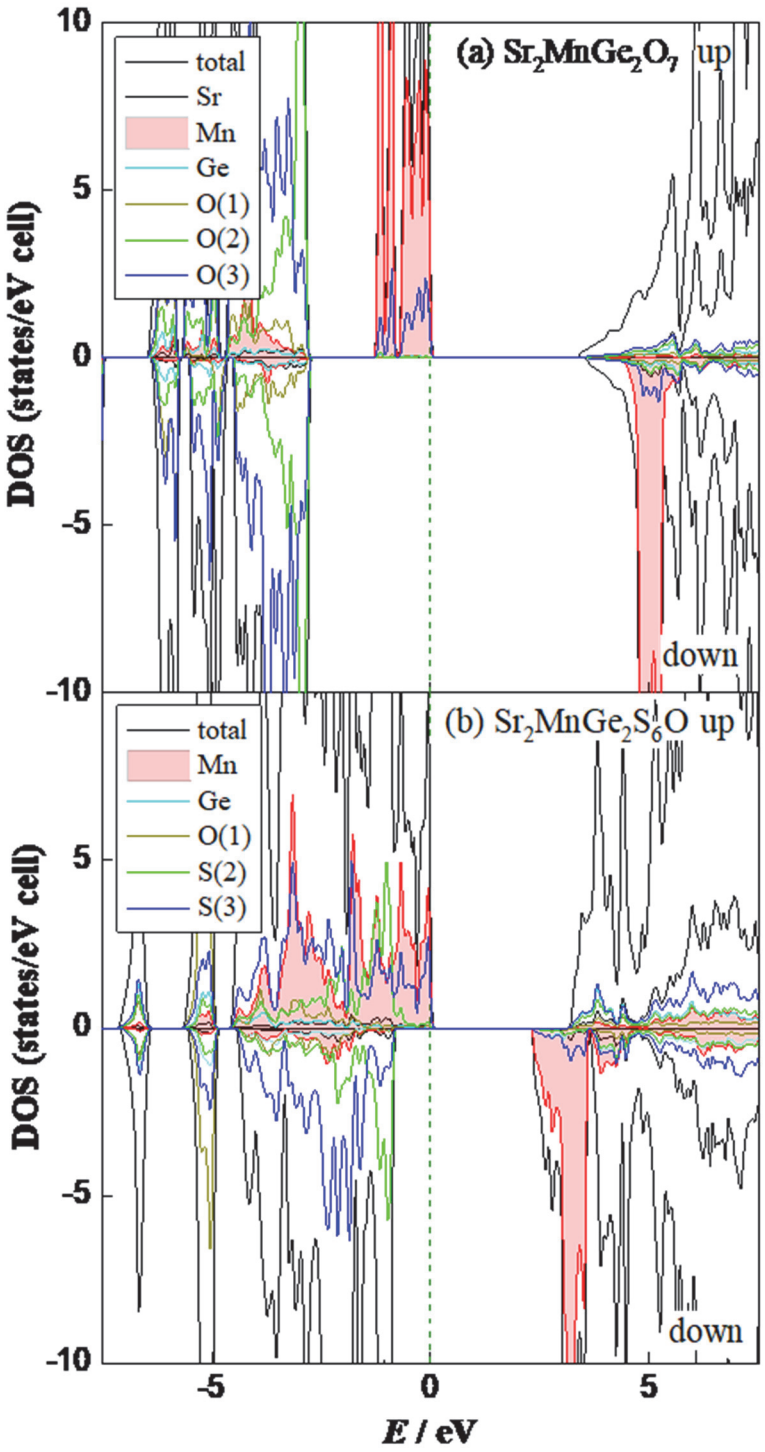


Figure 5.10 Total and partial DOS of total electrons of Sr, Mn, Ge, O and S for (a)$Sr_2MnGe_2O_7$ and (b)$Sr_2MnGe_2S_6O$. The zero energy is placed at the highest occupied state.

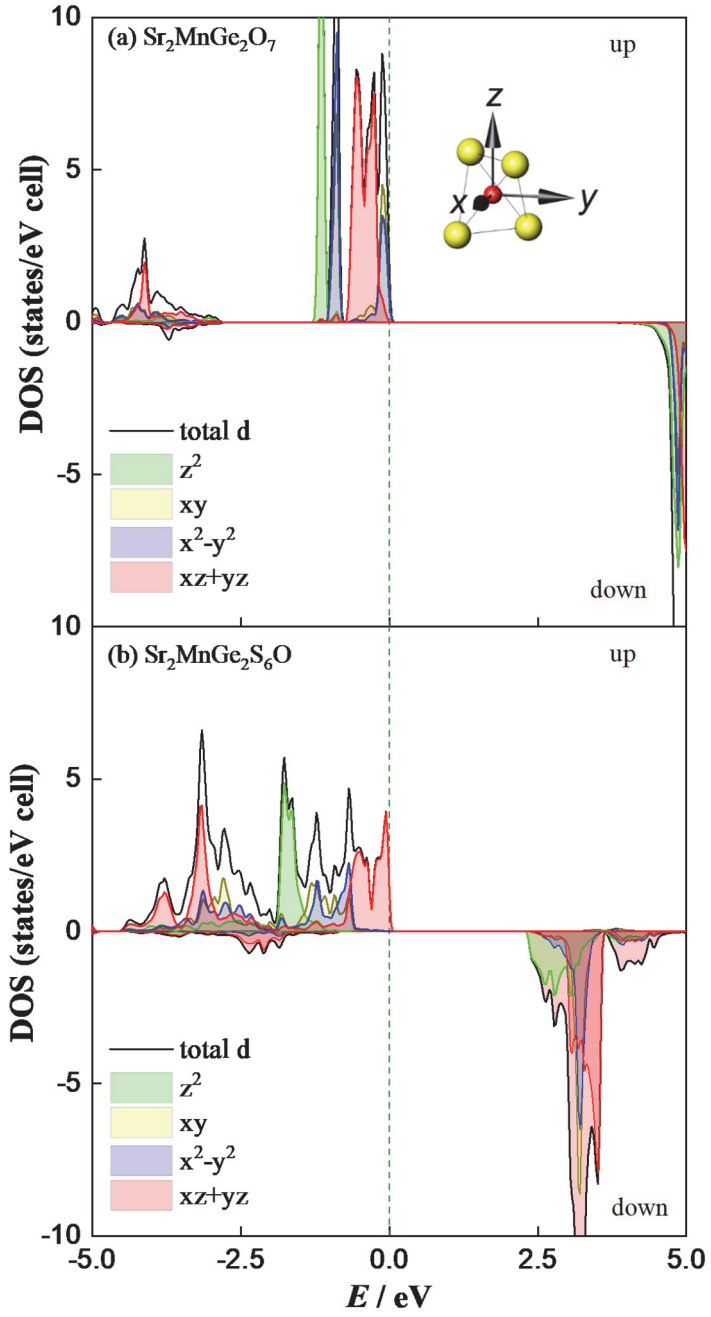


Figure 5.11 Partial DOS of the Mn orbitals for (a)$Sr_2MnGe_2O_7$ and (b)$Sr_2MnGe_2S_6O$.

## 5.6 References

(1) Burzo, E. Melilites and Related Silicates. In *Sorosilicates*; Springer-Verlag: Berlin/Heidelberg, 2009; Vol. 14, pp 29–60.

(2) Kaminskii, A. A.; Bohatý, L.; Becker, P.; Liebertz, J.; Held, P.; Eichler, H. J.; Rhee, H.; Hanuza, J. Tetragonal $Ba_2MgGe_2O_7$ - a Novel Multifunctional Optical Crystal with Numerous Manifestations of Nonlinear-Laser Effects: Almost Sesqui-Octave Stokes and Anti-Stokes Combs and Cascaded $\chi$ (3) ↔ $\chi$ (2) Lasing with Involved Sec. *Laser Phys. Lett.* **2008**, *5*, 845–868.

(3) Liang, C.; You, H.; Fu, Y.; Teng, X.; Liu, K.; He, J. A Novel Tunable Blue-Green-Emitting $CaGdGaAl_2O_7$ :$Ce^{3+}$,$Tb^{3+}$ Phosphor via Energy Transfer for UV-Excited White LEDs. *Dalt. Trans.* **2015**, *44*, 8100–8106.

(4) Kuang, X.; Green, M. a; Niu, H.; Zajdel, P.; Dickinson, C.; Claridge, J. B.; Jantsky, L.; Rosseinsky, M. J. Interstitial Oxide Ion Conductivity in the Layered Tetrahedral Network Melilite Structure. *Nat. Mater.* **2008**, *7*, 498–504.

(5) Kézsmárki, I.; Kida, N.; Murakawa, H.; Bordács, S.; Onose, Y.; Tokura, Y. Enhanced Directional Dichroism of Terahertz Light in Resonance with Magnetic Excitations of the Multiferroic $Ba_2CoGe_2O_7$. *Phys. Rev. Lett.* **2011**, *106*, 57403.

(6) Kézsmárki, I.; Szaller, D.; Bordács, S.; Kocsis, V.; Tokunaga, Y.; Taguchi, Y.; Murakawa, H.; Tokura, Y.; Engelkamp, H.; Rõõm, T.; Nagel, U. One-Way Transparency of Four-Coloured Spin-Wave Excitations in Multiferroic Materials. *Nat. Commun.* **2014**, *5*, 3203.

(7) Akaki, M.; Tadokoro, T.; Kuwahara, H.; Kihara, T.; Tokunaga, M. Anisotropic Magnetic Properties in Åkermanite $Sr_2MSi_2O_7$ (M=Co, Mn) Crystals. *J. Korean Phys. Soc.* **2013**, *62*, 1812–1814.

(8) Endo, T.; Doi, Y.; Wakeshima, M.; Hinatsu, Y. Crystal Structures and Magnetic Properties of New Europium Melilites $Eu_2MSi_2O_7$ (M = Mg, Mn) and Their Strontium Analogues. *Inorg. Chem.* **2010**, *49*, 10809–10814.

(9) Akaki, M.; Kuwahara, H.; Matsuo, A.; Kindo, K.; Tokunaga, M. Successive Magnetic Transitions of $Ca_2CoSi_2O_7$ in High Magnetic Fields. *J. Phys. Soc. Japan* **2014**, *83*, 93704.

(10) Tian, T.; Han, Y.; Ma, B.; Wu, C.; Chang, J. Novel Co-Akermanite ($Ca_2CoSi_2O_7$ ) Bioceramics with the Activity to Stimulate Osteogenesis and Angiogenesis. *J. Mater. Chem. B* **2015**, *3*, 6773–6782.

(11) Sazonov, A.; Hutanu, V.; Meven, M.; Roth, G.; Kézsmárki, I.; Murakawa, H.; Tokura, Y.; Náfrádi, B. The Low-Temperature Crystal Structure of the Multiferroic Melilite $Ca_2CoSi_2O_7$. *Acta Crystallogr. Sect. B Struct. Sci. Cryst. Eng. Mater.* **2016**, *72*, 126–132.

(12) Adams, R. D.; Payen, C.; Datta, T. Syntheses, Structural Analyses, and Unusual Magnetic Properties of $Ba_2CoSi_2O_7$ and $BaCo_2Si_2O_7$. *Inorg. Chem.* **1996**, *35*, 3492–3497.

(13) Endo, T.; Doi, Y.; Hinatsu, Y.; Ohoyama, K. Magnetic and Neutron Diffraction Study on Melilite-Type Oxides $Sr_2MGe_2O_7$ (M = Mn, Co). *Inorg. Chem.* **2012**, *51*, 3572–3578.

(14) Masuda, T.; Kitaoka, S.; Takamizawa, S.; Metoki, N.; Kaneko, K.; Rule, K. C.; Kiefer, K.; Manaka, H.; Nojiri, H. Instability of Magnons in Two-Dimensional Antiferromagnets at High Magnetic Fields. *Phys. Rev. B* **2010**, *81*, 100402.

(15) Murakawa, H.; Onose, Y.; Miyahara, S.; Furukawa, N.; Tokura, Y. Comprehensive Study of the Ferroelectricity Induced by the Spin-Dependent D-P Hybridization Mechanism in $Ba_2XGe_2O_7$ (X = Mn, Co, and Cu). *Phys. Rev. B* **2012**, *85*, 174106.

(16) Soda, M.; Matsumoto, M.; Månsson, M.; Ohira-Kawamura, S.; Nakajima, K.; Shiina, R.; Masuda, T. Spin-Nematic Interaction in the Multiferroic Compound $Ba_2CoGe_2O_7$. *Phys. Rev. Lett.* **2014**, *112*, 127205.

(17) Murakawa, H.; Onose, Y.; Miyahara, S.; Furukawa, N.; Tokura, Y. Ferroelectricity Induced by Spin-Dependent Metal-Ligand Hybridization in $Ba_2CoGe_2O_7$. *Phys. Rev. Lett.* **2010**, *105*, 137202.

(18) Kim, J. W.; Khim, S.; Chun, S. H.; Jo, Y.; Balicas, L.; Yi, H. T.; Cheong, S.-W.; Harrison, N.; Batista, C. D.; Hoon Han, J.; Hoon Kim, K. Manifestation of Magnetic Quantum Fluctuations in the Dielectric Properties of a Multiferroic. *Nat. Commun.* **2014**, *5*, 4419.

(19) Solovyev, I. V. Magnetization Induced Local Electric Dipoles and Multiferroic Properties of $Ba_2CoGe_2O_7$. *Phys. Rev. B* **2015**, *91*, 224423.

(20) Capitani, F.; Koval, S.; Fittipaldi, R.; Caramazza, S.; Paris, E.; Mohamed, W. S.; Lorenzana, J.; Nucara, A.; Rocco, L.; Vecchione, A.; Postorino, P.; Calvani, P. Raman Phonon Spectrum of the Dzyaloshinskii-Moriya helimagnet$Ba_2CuGe_2O_7$. *Phys. Rev. B* **2015**, *91*, 214308.

(21) Togawa, Y.; Koyama, T.; Takayanagi, K.; Mori, S.; Kousaka, Y.; Akimitsu, J.; Nishihara, S.; Inoue, K.; Ovchinnikov, A. S.; Kishine, J. Chiral Magnetic Soliton Lattice on a Chiral Helimagnet. *Phys. Rev. Lett.* **2012**, *108*, 107202.

(22) Nucara, A.; Mohamed, W. S.; Baldassarre, L.; Koval, S.; Lorenzana, J.; Fittipaldi, R.; Balakrishnan, G.; Vecchione, A.; Calvani, P. Infrared Phonon Spectrum of the Tetragonal Helimagnet $Ba_2CuGe_2O_7$. *Phys. Rev. B* **2014**, *90*, 14304.

(23) Mühlbauer, S.; Gvasaliya, S.; Ressouche, E.; Pomjakushina, E.; Zheludev, A. Phase Diagram of the Dzyaloshinskii-Moriya Helimagnet $Ba_2CuGe_2O_7$ in Canted Magnetic Fields. *Phys. Rev. B* **2012**, *86*, 24417.

(24) Ochi, Y. Structures and Magnetic Properties of Rare Earth Compounds in the Melilite Group. *Yogyo Kyokaishi* **1983**, *91*, 229–235.

(25) Takahashi, H.; Igawa, K.; Arii, K.; Kamihara, Y.; Hirano, M.; Hosono, H. Superconductivity at 43 K in an Iron-Based Layered Compound $LaO_{1-x}F_xFeAs$. *Nature* **2008**, *453*, 376–378.

(26) Adamson, P.; Hadermann, J.; Smura, C. F.; Rutt, O. J.; Hyett, G.; Free, D. G.; Clarke, S. J. Competing Magnetic Structures and the Evolution of Copper Ion/Vacancy Ordering with Composition in the Manganite Oxide Chalcogenides $Sr_2MnO_2Cu_{1.5}(S_{1-x}Se_x)_2$. *Chem. Mater.* **2012**, *24*, 2802–2816.

(27) Yu, R.; Wang, J.; Zhang, M.; Zhang, J.; Yuan, H.; Su, Q. A New Blue-Emitting Phosphor of $Ce^{3+}$-Activated $CaLaGa_3S_6O$ for White-Light-Emitting Diodes. *Chem. Phys. Lett.* **2008**, *453*, 197–201.

(28) Yu, R. J.; Park, J. Y.; Yang, H. K.; Moon, B. K.; Choi, B. C.; Jeong, J. H. A New Deep Red-Emitting $Mn^{2+}$-Activated $SrLaGa_3S_6O$ Phosphor. *Key Eng. Mater.* **2012**, *531–532*, 145–148.

(29) Zhang, G.; Liu, C.; Wang, J.; Kuang, X.; Su, Q. A Dual-Mode Solar Spectral Converter $CaLaGa_3S_6$ $O:Ce^{3+},Pr^{3+}$ : UV-Vis-NIR Luminescence Properties and Solar Spectral Converting Mechanism. *J. Mater. Chem.* **2012**, *22*, 2226–2232.

(30) Zhang, X.; Zhang, J.; Liang, L.; Su, Q. Luminescence of $SrGdGa_3O_7:RE^{3+}$(RE=Eu, Tb) Phosphors and Energy Transfer from $Gd^{3+}$ to $RE^{3+}$. *Mater. Res. Bull.* **2005**, *40*, 281–288.

(31) Zhang, X.; Zhang, J.; Xu, J.; Su, Q. Luminescent Properties of $Eu^{2+}$-Activated $SrLaGa_3S_6O$ Phosphor. *J. Alloys Compd.* **2005**, *389*, 247–251.

(32) Teske, C. L. Über Oxidsulfide Mit Åkermanitstruktur $CaLaGa_3S_6O$, $SrLaGa_3S_6O$, $La_2ZnGa_2S_6O$ Und $Sr_2ZnGe_2S_6O$. *Zeitschrift für Anorg. und Allg. Chemie* **1985**, *531*, 52–60.

(33) Kim, T.-G.; Kim, S.-J.; Lin, C. C.; Liu, R.-S.; Chan, T.-S.; Im, S.-J. Melilite-Type Blue Chromophores Based on Mn3+ in a Trigonal-Bipyramidal Coordination Induced by Interstitial Oxygen. *J. Mater. Chem. C* **2013**, *1*, 5843.

(34) Izumi, F.; Momma, K. Three-Dimensional Visualization in Powder Diffraction. *Solid State Phenom.* **2007**, *130*, 15–20.

(35) Momma, K.; Izumi, F. VESTA 3 for Three-Dimensional Visualization of Crystal, Volumetric and Morphology Data. *J. Appl. Crystallogr.* **2011**, *44*, 1272–1276.

(36) Blaha, P.; Schwarz, K.; Madsen, G.; Kvasnicak, D.; Luitz, J. WIEN2k, An Augmented Plane Wave Plus Local Orbitals Program for Calculating Crystal Properties.; 2014.

(37) Tran, F.; Blaha, P. Accurate Band Gaps of Semiconductors and Insulators with a Semilocal Exchange-Correlation Potential. *Phys. Rev. Lett.* **2009**, *102*, 226401.

(38) Brown, I. D.; Altermatt, D. Bond-Valence Parameters Obtained from a Systematic Analysis of the Inorganic Crystal Structure Database. *Acta Crystallogr. Sect. B* **1985**, *41*, 244–247.

(39) Brese, N. E.; O'Keeffe, M. Bond-Valence Parameters for Solids. *Acta Crystallogr. Sect. B* **1991**, *47*, 192–197.

(40) Shannon, R. D. Revised Effective Ionic Radii and Systematic Studies of Interatomic Distances in Halides and Chalcogenides. *Acta Crystallogr. Sect. A* **1976**, *32*, 751–767.

(41) Bocquet, A. E.; Fujimori, A. Predictions for Core-Level X-Ray Photoemission Spectra of Divalent and Trivalent 3d Transition-Metal Compounds. *J. Electron Spectros. Relat. Phenomena* **1996**, *82*, 87–124.

(42) Oku, M.; Hirokawa, K.; Ikeda, S. X-Ray Photoelectron Spectroscopy of Manganese—oxygen Systems. *J. Electron Spectros. Relat. Phenomena* **1975**, *7*, 465–473.

(43) Carver, J. C. Use of X-Ray Photoelectron Spectroscopy to Study Bonding in Cr, Mn, Fe, and Co Compounds. *J. Chem. Phys.* **1972**, *57*, 973.

(44) Imada, M. Metal-Insulator Transitions. *Rev. Mod. Phys.* **1998**, *70*, 1039–1263.

(45) Hollinger, G.; Kumurdjian, P.; Mackowski, J. M.; Pertosa, P.; Porte, L.; Duc, T. M. ESCA Study of Molecular $GeS_{3-x}Te_xAs_2$ Glasses. *J. Electron Spectros. Relat. Phenomena* **1974**, *5*, 237–245.

(46) De Joungh, L. J. *Magnetic Properties of Layered Transition Metal Compouds*; Kluwer, Ed.; Academic Publishers: Dordrecht, 1990.

(47) Carlin, R. L. *Magnetochemistry*; Springer-Verlang: Berlin, 1986.

(48) Rushbrooke, G. S.; Wood, P. . On High Temperature Expansions for the Heisenberg Model. *J. Proc. Phys. Soc., London* **1955**, *68*, 1161–1169.

(49) Rushbrooke, G. S.; Wood, P. J. On the Curie Points and High Temperature Susceptibilities of Heisenberg Model Ferromagnetics. *Mol. Phys.* **1958**, *1*, 257–283.

(50) Stephenson, R. L.; Pirnie, K.; Wood, P. J.; Eve, J. On the High Temperature Susceptibility and Specific Heat of the Heisenberg Ferromagnet for General Spin. *Phys. Lett. A* **1968**, *27*, 2–3.

(51) Yamaji, K.; Konda, J. On the High-Temperature Susceptibilities of the Two-Dimensional Ferromagnetic Heisenberg Spin Systems. *J. Phys. Soc. Japan* **1973**, *35*, 25–32.

(52) Masuda, T.; Kitaoka, S.; Takamizawa, S.; Metoki, N.; Kaneko, K.; Rule, K. C.; Kiefer, K.; Manaka, H.; Nojiri, H. Instability of Magnons in Two-Dimensional Antiferromagnets at High Magnetic Fields. *Phys. Rev. B* **2010**, *81*, 100402.

(53) Joshua, S. J.; Cracknell, A. P. The Spin-Wave Contribution to the Specific Heat of $NiF_2$. *Phys. Lett. A* **1969**, *28*, 562–563.

(54) Kubelka, P.; Munk, F. Ein Beitrag Zur Optik Der Farbanstriche. *Z. Techn. Phys.* **1931**, *12*, 593.

(55) Tauc, J.; Grigorovici, R.; Vancu, A. Optical Properties and Electronic Structure of Amorphous Germanium. *Phys. Stat. Sol* **1966**, *15*, 627.

(56) Terasawa, H.; Kambara, T.; Gondaira, K. .; Teranishi, T.; Sato, K. The Blue Shift of the Optical Absorption Edge in α-MnS. *J. Phys. C Solid State Phys.* **1980**, *13*, 5615–5629.

(57) Zheng, Y.; Cheng, Y.; Wang, Y.; Zhou, L.; Bao, F.; Jia, C. Metastable γ -MnS Hierarchical Architectures : Synthesis , Characterization , and Growth Mechanism. *J. Phys. Chem. B* **2006**, *110*, 8284–8288.

(58) Company, E.; Introduction, I. HIGH TEMPERATURE MAGNETIC SUSCEPTIBILITIES Of MnO, MnSe AND MnTe. *J. Phys. Chem.* **1956**, *5*, 7–9.

(59) Lin, M. S.; Hacker, H. Antiferromagnetic Transitions in $MnS_2$ and $MnTe_2$. *Solid State Commun.* **1968**, *6*, 687–689.

(60) Chattopadhyay, T.; Rossat-Mignod, J.; Fjellvåg, H. Magnetic Ordering in $MnSe_2$. *Solid State Commun.* **1987**, *63*, 65–67.

# Chapter 6

# Crystal Structure Analysis, $^{151}$Eu Mössbauer Spectroscopy, and Magnetic Properties of Oxysulfide Melilites $Eu_2MGe_2S_6O$ ($M$ = Mn, Zn)

## 6.1 Introduction

The mixed-anion compounds often show novel electronic and magnetic properties[1,2]. In general, when the oxide ions are replaced by other anions, its crystal structure changes from the original oxides due to the ionic size and the electronegativity[3-5]. On the other hand, there are few reports on compounds in which crystal structures do not change before and after anion substitution, such as NaCl-type, ZnO-type structure and some systems[6, 7].

Recently, we have succeeded in synthesizing the melilite-type compound $Sr_2MnGe_2S_6O$, which has the same crystal structure before and after anion substitution[8]. This compound shows the long-range AFM ordering at 15.5 K, and its ordering temperature much higher than that of oxide analogues $Sr_2MnGe_2O_7$ (4.4 K)[9]. The melilite-type compounds are represented by a general formula $A_2MM'_2X_7$ ($A$ = larger cations such as alkali earth and lanthanide ions; $M$, $M'$ = smaller divalent to tetravalent ions; $X$ = N, O, F, S)[10, 11]. The schematic crystal structure of melilite-type compounds is illustrated in Figure 6.1. In this structure, both the $M$ and $M'$ ions occupy tetrahedral sites and these tetrahedra form a two-dimensional (2D) network in the $ab$-plane; larger $A$ ions are located between the networks.

However, most of the melilite-type compounds reported until now are the ones in which magnetic ions are occupied at the *M*-site. The *M* site locates at the corner and the base-center of the unit cell, thus the dominant pathway is the magnetic super-super exchange *M*-O-O-*M* interaction pathway in the *ab*-plane[12, 13]. On the other hand, there have been few reports about the melilite-type compounds in which magnetic ions occupy the *A* site. As far as we know, only the $Ln_2BeGe_2O_7$ (*Ln* = Pr, Sm, Gd, Dy and Er) and $Eu_2MgSi_2O_7$ have been reported[13, 14]. In these compounds, the super exchange *A*-O-*A* interaction pathway in the *ab*-plane is dominant. Since the interaction between *f* electrons in *Ln* ions is relatively weak, no magnetic transition is observed even at low temperatures. Thus, their magnetic properties are paramagnetic down to 1.8 K. As far as we know, $Eu_2MnSi_2O_7$ is the only compound which contains magnetic ions in both the M and A sites. This compound shows a ferrimagnetic transition at 10.9 K. The predominant magnetic interaction is the *f* - *d* interaction through Eu-O-Mn super exchange pathway, and both ferromangnetic Eu and Mn ions align parallel at 10.9K[13].

In this study, we investigated the syntheses, crystal structure analysis, and magnetic properties of new melilite-oxysulfides $Eu_2MGe_2S_6O$ (M = Mn, Zn). For comparison, the analogues compounds $Sr_2MnGe_2O_7$[9], $A_2MnSi_2O_7$ (*A* = Eu, Si)[13] and $Sr_2MGe_2S_6O$[8] were also prepared. The results of the powder X-ray diffraction (PXRD), magnetic susceptibility, specific heat measurements and the density functional theory (DFT) calculation are discussed. This is the first report on the introduction of two kind magnetic ions into the melilite-oxysulfides system.

## 6.2 Experimental procedures

### 6.2.1 Synthesis

The title compounds $Eu_2MGe_2S_6O$ ($M$ = Mn and Zn) were prepared as polycrystalline samples by the solid-state reaction. The starting materials (EuS, MnO, ZnO and $GeS_2$) were weighed out in a stoichiometric ratio and well grinded in an agate mortar in a glove-box under an Ar atmosphere. Mixtures of the starting materials were pressed into a pellet and then sealed in an evacuated quartz tube. To avoid reactions between the sample and quartz tube, the pellet was set into small inner crucibles made of carbon. The ampoules were heated at 800 °C for 12 h.

### 6.2.2 Crystal structure analysis

Powder X-ray diffraction measurements were performed at room temperature using a Multi-Flex diffractometer and RINT-2000 (Rigaku) with a Cu-Kα X-ray radiation source equipped with a curved graphite monochromator. The data were collected by step-scanning over the angle range of $10° \leq 2\theta \leq 120°$ at a step size of 0.02°. The PXRD data were analyzed by the Rietveld method using the program RIETAN-FP[15], and the crystal structures were drawn using the VESTA program package[16].

### 6.2.3 Characterization

The $^{151}$Eu Mössbauer spectra were measured at room temperature with a Mössbauer VT-6000 transmission spectrometer (Laboratory Equipment) using a radiation source $^{151}SmF_3$(1.85 GBq). The spectrometer was calibrated with α-Fe at room

temperature, and the isomer sift (*I.S.*) was determined relative to the shift of europium trifluoride ($EuF_3$). The γ-ray was detected by a NaI scintillation counter. The powder sample was wrapped in an aluminum foil (2.0 cm × 2.0 cm) with the density of 15 mg (Eu)/$cm^2$.

The UV-vis diffuse reflectance spectra were measured with a V-570 instrument (JASCO) over the wavelength range of 220-1000 nm.

The temperature dependence of the magnetic susceptibility was measured with a SQUID magnetometer (Quantum Design, MPMS-5S). The measurements were performed under both zero-field-cooled (ZFC) and field-cooled (FC) conditions over the temperature range between 1.8 and 300 K in an applied magnetic field of 0.1 T. The field dependence of the magnetization was measured over the magnetic field range between -5 and 5 T in the temperature range between 1.8 - 40 K.

The specific heat measurements were performed using a relaxation technique with a commercial physical property measurement system (Quantum Design, PPMS) over the temperature range of 1.8-300 K. The pelletized sample was mounted on a thin alumina plate with Apiezon N grease for better thermal contact.

### 6.2.4 DFT calculation

Calculations of the electronic structure and the density of states (DOS) were performed using the WIEN2k program package[17]. This program employs the full−potential linearized augmented plane wave + local orbitals (FP−LAPW+lo) method based on density functional theory. We used the generalized gradient approximation (GGA) + Hubbard *U* parameter for the Mn 3d and Eu 4f electrons. In the calculations, the convergence parameter was set to be $R_{MT}k_{max} = 7.0$, and the muffin tin (MT) sphere radii were $R_{MT}$(Sr) = 2.50 bohr, $R_{MT}$(Mn) = 2.46 bohr, $R_{MT}$(Ge) = 1.87 bohr, $R_{MT}$(O) = 1.69

bohr, and $R_{MT}$(S) = 1.84 bohr. We used 8 × 8 × 13 meshes with 70 *k* points in the first Brillouin zone (B.Z.).

## 6.3 Results and discussion

### 6.3.1 Synthesis and crystal structure

The new melilite-type oxysulfides $Eu_2MGe_2S_6O$ (*M* = Mn, Zn) were successfully prepared as light-green, yellow colored polycrystalline samples, respectively. The powder X-ray diffraction data are plotted in Figure 6.2. The observed Bragg peaks were indexed on a tetragonal unit cell with the space group *P*-42$_1$*m*, which is typical for the melilite-type compounds[10, 11]. The X-ray diffraction profiles were analyzed by the Rietveld method. For an initial structural model, the structural parameters of a melilite oxysulfide $Sr_2MnGe_2S_6O$ were used[8]. In addition, we tried to analyze the profile data using three other models with different occupations of S and O ions (see Table 6.1 and Table 6.2). As a result, the best fit was obtained for the initial model, i.e., the O ions occupy the 2*c* site and S ions occupy both the 4*e* and 8*f* sites. The calculated profiles are also shown in Figure 6.2, and these results suggest that the $Eu_2MGe_2S_6O$ (*M* = Mn, Zn) have the same structures with those for their Sr-analogues $Sr_2MGe_2S_6O$ (*M* = Mn, Zn)[8, 18].

The crystal structure of $Eu_2MGe_2S_6O$ is illustrated in Figure 1, and their structural parameters are summarized in Table 6.3. In this crystal structure, the *M* and Ge ions form the $MS_4$ and $GeS_3O$ tetrahedra. The $MS_4$ connects with four $GeS_3O$ by sharing the corner S ion, while the $GeS_3O$ connects with one $GeS_3O$ and two $MS_4$ by sharing the corner O and S ions, respectively, and the remaining one S ion is not shared. These connections construct a two-dimensional network of tetrahedra in the *ab*-plane. The Eu ions locate between such layers, and each Eu ion is surrounded by seven S and one O ions, forming distorted $EuS_7O$ square-antiprism. The selected interatomic

distances and bond valence sums (BVSs)[19, 20] are listed in Table 6.4 and the coordination environments of three cation sites in the $Eu_2MnGe_2S_6O$ are illustrated in Table 6.5. The interatomic distances are comparable to those calculated from the Shannon's ionic radii: $l(Eu^{2+}–S^{2-})$ = 3.09 Å, $l(Eu^{2+}–O^{2-})$ = 2.65 Å, $l(Mn^{2+}–S^{2-})$ = 2.50 Å, $l(Zn^{2+}–S^{2-})$ = 2.44 Å, $l(Ge^{4+}–S^{2-})$ = 2.23 Å, and $l(Ge^{4+}–O^{2-})$ = 1.79 Å.[21] The BVSs for the cations indicate that the Eu and Mn/Zn ions are divalent and the Ge ions are tetravalent, so the title compounds can be represented as $Eu^{2+}{}_2M^{2+}Ge^{4+}{}_2S^{2-}{}_6O^{2-}$.

The $^{151}$Eu Mössbauer spectrum measurements were carried out to elucidate the oxidation state of Eu ion. Figure 6.4 shows the $^{151}$Eu Mössbauer spectra for $Eu_2MnGe_2S_6O$ and $Eu_2ZnGe_2S_6O$ at room temperature. In both spectra, an absorption peak is observed at about -12.5 mm/s, which indicates the presence of the divalent Eu ions[22]. For both compounds, a weak absorption peak due to the trivalent Eu ion appears at ~0.5 mm/s; its small intensity (~5 % of total area intensity) may mean the existence of surface oxidation during the Mössbauer measurements. The observed main peak is somewhat asymmetric because the Eu ions occupy the 4*e* site with $m(C_s)$ point symmetry, i.e., there is an electric field gradient (EFG) at the nucleus due to the quadrupole interaction. The quadrupole Hamiltonian at a Eu nuclear site is given by

$$HQ = \frac{e^2qQ}{4I(2I-1)}(3I_z^2 - I(I+1) + \eta(I_x^2 - I_y^2)) \qquad (6.1)$$

where $I$ is the nuclear spin, $Q$ is the quadrupole moment, $eq = V_{ZZ}$, and $\eta = (V_{XX} - V_{YY}) / V_{ZZ}$ ($V_{ii}$ is the electric field gradient (EFG) tensor). The 12 possible transitions (eight allowed transitions and four forbidden transitions) due to a quadrupole interaction were taken into account. The observed spectra were fitted with the sum of these 12 Lorentzian functions, which were derived from the results by Shenoy and Dunlap[23] and a ratio of quadrupole moments in excited and ground states is $R_Q = Q_e/Q_g$ = 1.42. [24]

The fitting curves are shown in Figure 6.4, and the determined fitting parameters are listed in Table 6.5. The large Q.S. (6.77 ~ 6.93 mm/s) and non-zero $\eta$ (0.44~ 0.89)

values indicate that the Eu ion is in a greatly distorted coordination environment in these compounds. In fact, these Eu ions locate in the distorted $EuS_7O$ polyhedron with one short Eu-O and seven long Eu-S bond lengths (see Table 6.4). The large difference in the shape of Mössbauer spectra is ascribed to the distortion of $EuS_7O$ polyhedron between Mn and Zn compounds. The Q.S. and $\eta$ values are also calculated by the DFT calculation using the structural parameters for $Eu_2MnGe_2S_6O$ and $Eu_2ZnGe_2S_6O$. The obtained parameters are also listed in Table 6.5, and the Q.S. values are in good agreement with the experimental data. It should be noted that the Q.S. value is positive, while those of analogue oxides with eight Eu-O bonds are negative. The experimental and calculated Q.S. of $Eu_2MnSi_2O_7$ were reported to be -12.8 mm/s with $\eta = 0.26$ and -11.1 mm/s with $\eta = 0.46$, respectively[13]. In general, the EFG tensor $V_{ij}$ (= $V_{ij}^{4f} + V_{ij}^{latt}$) of Eu consists of the $V_{ij}^{4f}$ term depending on the 4f configuration and the lattice contribution $V_{ij}^{latt}$.[25] For $Eu^{3+}$ with the $^7F_1$ and $^7F_2$ excited states, most of signs of Q.S. are negative because of the significant $V_{ij}^{4f}$ contribution[26]. On the other hand, for $Eu^{2+}$ with the $^8S_{7/2}$ ground state, the $V_{ij}^{4f}$ term is quenched and the only lattice term $V_{ij}^{latt}$ contributes to the total $V_{ij}$, resulting in the fact that the Q.S. value is sensitive to the Eu coordination environment.

## 6.3.2 Magnetic properties.

### 6.3.2.1 $Eu_2ZnGe_2S_6O$

Temperature dependence of the reciprocal magnetic susceptibility ($\chi_M^{-1}$) for $Eu_2ZnGe_2S_6O$ is plotted in Figure 6.5. This compound shows the paramagnetic behavior down to 1.8 K. The data (100–300 K) were fitted by the Curie-Weiss law:

$$\chi_M = \frac{C}{T - \theta} + \chi_{TIP} \tag{6.2}$$

where $C$, $\theta$, and $\chi_{TIP}$ mean the Curie constant, Weiss constant, and temperature-independent paramagnetic susceptibility, respectively. The effective magnetic moment

($\mu_{eff}$) was determined to be 11.19(1) $\mu_B$ per formula unit, which is close to the spin-only value (11.22 $\mu_B$) calculated from the two $Eu^{2+}$ ions ($S$ = 7/2). The small $\theta$ value (–0.9(4) K) means the magnetic interaction between Eu ions is very weak, and its negative sign indicates that this interaction is antiferromagnetic.

Figure 6.6 (b) shows the temperature dependence of the specific heat for $Eu_2ZnGe_2S_6O$ below 50 K. At 5 K, the specific heat turns to increase with decreasing temperature, which shows the occurrence of the magnetic ordering of the $Eu^{2+}$ ions. The magnetic specific heat ($C_{mag}$) was obtained by subtracting the lattice specific heat ($C_{lat}$) from $C_p$. Then, the magnetic specific heat was determined by using the equation $S_{mag} = \int_0^T C_{mag}/TdT$. The magnetic specific heat below 1.8 K was extrapolated by the relation $C_{mag} \propto T^3$ from the spin-wave model for an antiferromagnet[27]. The temperature dependence of the magnetic specific heat divided by temperature ($C_{mag}/T$) and magnetic entropy ($S_{mag}$) are plotted in Figure 6.6 (c). The total magnetic entropy change is 3.1 J $mol^{-1}$ $K^{-1}$ at 10 K, and this value is 9 % of the expected value for $Eu^{2+}$, $2R$ ln8 (= 34.7 J $mol^{-1}$ $K^{-1}$) from the sum of when all the $Eu^{2+}$ moments order. The lower magnetic entropy changes than the expected value was caused by the incomplete magnetic transition in the experimental temperature range.

Figure 6.7 shows the field dependence of the magnetization for $Eu_2ZnGe_2S_6O$ measured at 1.8 K. The magnetization ($M$) increases and shows a saturation behavior with increasing the magnetic field ($H$), which is similar to the paramagnetic or ferromagnetic properties. The observed $M$-$H$ curve is somewhat smaller than the twofold of the Brillouin function with $S$ = 7/2 (a dashed curve in Figure 6.7) and there is no hysteresis loop; thus, this behavior is considered to be paramagnetic rather than ferromagnetic. Therefore, we fitted the data using a modified Brillouin funcrtion[28]:

$$M = 2 \times gSB_s\left(\frac{gS\mu_B H}{k_B(T - T_0)}\right) \tag{6.3}$$

where parameter $T_0$ accounts phenomenologically for the magnetic interaction between $Eu^{2+}$ ions. The fitting curve is shown in Figure 6.7 as a solid line, and two fitting parameters ($gS$ and $T_0$) are obtained to be 6.7 and –0.5 K, respectively. The former value is reasonable for $Eu^{2+}$ ions ($gS \sim 7$), and the latter one is negative and close to the Weiss constant (–0.9 K) which suggests the existence of the antiferromagnetic interaction. The magnetic properties of $Eu_2ZnGe_2S_6O$ are quite similar to those for the oxide analogue $Eu_2MgSi_2O_7$: a paramagnetic behavior down to 1.8 K with the small $\theta$ (–1.2 K) and $T_0$ (–1.0 K) values[13]. Despite the difference in anions, there is no much difference in magnetic properties between $Eu_2ZnGe_2S_6O$ and $Eu_2MgSi_2O_7$, and the magnetic interaction between the $Eu^{2+}$ ions are still weak.

### 6.3.2.2 $Eu_2MnGe_2S_6O$

The temperature dependence of the reciprocal magnetic susceptibility for $Eu_2MnGe_2S_6O$ is also plotted in Figure 6.5. From the result of fitting the data above 100 K by using eq (6.2), the $\mu_{eff}$ was determined to be 12.74(1) $\mu_B$ per formula unit. This value is close to $\sqrt{2\times\mu_{Eu^{2+}}^2+\mu_{Mn^{2+}}^2}=12.69\ \mu_B$, which is calculated from the magnetic moments of two $Eu^{2+}$ ($S$ = 7/2) and $Mn^{2+}$ ($S$ = 5/2) ions. The positive $\theta$ value (3.8(2) K) may indicate the presence of ferromagnetic interaction; however, no clear ferromagnetic behavior was observed in other measurements.

Figure 6.8 (a) and (b) show the temperature dependence of the magnetic susceptibility and specific heat ($C_p$) at low temperatures, respectively. From the $C_p$ data, two $\lambda$-type anomalies are observed at 14.8 and 2.3 K. The former anomaly is very similar to that found in analogues oxysulfide melilite $Sr_2MnGe_2S_6O$ at 15.5 K[8] indicating an antiferromagnetic transition of $Mn^{2+}$ ions. The corresponding anomaly is not found in the $\chi_M$ data at the same temperature; but it is considered that the very large $\chi_M$ value of $Eu^{2+}$ ions compared to that of $Mn^{2+}$ ion (0.01–0.08 emu/mol at 1.8–300 K observed in

$Sr_2MnGe_2S_6O$ [8]) makes the magnetic anomaly invisible. Conversely, both the $\chi_M$ and $C_p$ data show an anomaly at 2.3 K suggesting another magnetic transition.

Figure 6.8 (c) shows the magnetic part of specific heat divided by temperature ($C_{mag}/T$) and magnetic entropy ($S_{mag}$). The $C_{mag}$ and $S_{mag}$ were calculated by the same way as the case of $Eu_2ZnGe_2S_6O$. The total change of $S_{mag}$ corresponding to two magnetic transitions reaches 32.2 J $mol^{-1}$ $K^{-1}$ at 50 K. This value is 65 % of the theoretical magnetic entropy change calculated from $2R \ln (2S_{Eu2+} + 1) + R \ln (2S_{Mn2+} + 1) = 49.5$ J $mol^{-1}$ $K^{-1}$. The $\Delta S_{mag}$ for the anomaly at 14.8 K is 11.4 J $mol^{-1}$ $K^{-1}$, which is comparable to 13.2 J $mol^{-1}$ $K^{-1}$ observed in $Sr_2MnGe_2S_6O$ [8] and the theoretical value $R \ln 6 = 14.9$ J $mol^{-1}$ $K^{-1}$. Therefore, the anomaly at 14.8 K is due to the antiferromagnetic transition of $Mn^{2+}$ ions. On the other hand, the $\Delta S_{mag}$ for the anomaly at 2.3 K is about 20.8 J $mol^{-1}$ $K^{-1}$, which is much smaller than the entropy change due to magnetic ordering of $Eu^{2+}$ ions. One reason for this is that the large magnetic contribution below 1.8 K has not been taken into account.

Figure 6.7 also shows the field dependence of the magnetization for $Eu_2MnGe_2S_6O$ measured at 1.8 K. The magnetization of $Eu_2MnGe_2S_6O$ increases with magnetic field and shows a saturation behavior (12.7 $\mu_B$). The value of the saturation magnetization is regarded as two Eu ions (7 $\mu_B \times 2$), thus the contribution of Mn ions is very few.

### 6.3.3 DFT calculation

Figure 6.9 shows the UV-vis diffuse reflectance spectra of $Eu_2ZnGe_2S_6O$ and $Eu_2MnGe_2S_6O$. The absorption values were calculated from the reflectance data using the KubelkaMunk function:

$$F(R_\infty) = \frac{(1 - R_\infty)^2}{2R_\infty} \tag{6.4}$$

where $R_\infty$ is the reflectance[29]. The energy of the optical band gap was determined using the Tauc plot[30]. The optical band gaps were determined to be 2.35 eV for $Eu_2ZnGe_2S_6O$ and 2.34 eV for $Eu_2MnGe_2S_6O$ as shown in Figure 6.9. In this compound, the photon energy ($h\nu$) is proportional to $(F(R_\infty)h\nu)^2$ near the bottom of the conduction band. This band gap is close to the optical band gaps (~2.4 eV) of the europium sulfide EuS with the transitions between the $4f^7(^8S_{1/2})$ to $4f^6(^7F_J)5d(t_{2g})$ electronic states[31].

In order to discuss chemical bonding, we carried out the DFT calculation. Figure 6.10 (a) and (b) display the total densities of states (DOS) and the partial DOS of total electrons of Eu, Mn, Ge, O, and S for $Eu_2MnSi_2O_7$ and $Eu_2MnGe_2S_6O$, respectively. In the DFT calculations for insulators with strongly correlated electrons, the energy of the band gap is very sensitive to the Hubbard $U$ parameter. We have attempted to estimate the band gap ($E_g$) by varying the $U$ parameter, but the values of $E_g$ were almost constant because of the contribution to the conduction band by the Ge 3s and 3d orbitals which are independent of $U$. Thus, the $U$ parameters are set to 5.0 eV for Mn and 7.8 eV for Eu. The calculated values of $E_g$ (2.32 eV for $Eu_2MnSi_2O_7$ and 2.35 eV for $Eu_2MnGe_2S_6O$) are in good agreement with the optical band gap from the UV-vis spectrum. The valence band of $Eu_2MnGe_2S_6O$ demonstrates strong hybridization between the Mn 3d and S(3) 3p orbitals over the broad range from -5.2 eV to 0 eV, while the top of the valence band in the narrow range between -2.6 eV to -0.8 eV mainly consists of the Mn 3d orbitals for $Eu_2MnSi_2O_7$. The energy levels for $Eu_2MnSi_2O_7$ indicate that this compound is classified into a Mott-Hubbard insulator[32]. Because the spin-up 3d orbitals are located below the Fermi level ($E_F$) and the spin-down 3d orbitals exist above the $E_F$, the results reveal that the Mn ions are in the divalent state with the high-spin configuration and that both compounds have a magnetic moment of 4.4 $\mu_B$ per Mn atom. For the densities of state of $Eu_2MnGe_2S_6O$, the S atom exists between Eu atom and Mn atom levels, and it widens between Eu and Mn energy levels. This means that the magnetic interaction between the Eu - Mn ions in the $Eu_2MnGe_2S_6O$ is lowered than $Eu_2MnSi_2O_7$, which is the reason why the cooperative magnetic transition seen in the oxide disappeared.

## 6.4 Summary

Here, we have reported synthesis, crystal structures and magnetic properties of new melilite-type oxysulfides $Eu_2MGe_2S_6O$ ($M$ =Mn, Zn). They crystallize in a tetragonal melilite-type structure with space group $P\text{-}42_1m$. The temperature dependence of magnetic susceptibility for $Eu_2ZnGe_2S_6O$ is paramagnetic down to 1.8 K. On the other hand, the temperature dependence of magnetic susceptibility and the specific heat measurement for $Eu_2MnGe_2S_6O$ show two anomalies at $T_{N1}$ = 14.8 K and $T_{N2}$ = 2.3 K. They are due to long-range magnetic ordering of Mn and Eu sublattice.

## 6.5 Tables and figures

Table 6.1 The reliability factors of Rietveld analyses for $Eu_2MnGe_2S_6O$ with different O/S ion occupations.

| Model | $R_{wp}$ (%) | $R_B$ (%) | Occupancy of O/S ion and $B$ (Å$^2$) for three anion sites | | |
|---|---|---|---|---|---|
| | | | $X$(1) 2$c$ site | $X$(2) 4$e$ site | $X$(3) 8$f$ site |
| 1 (text) | 10.08 | 2.14 | 1.0/0.0<br>*0.97(42)* | 0.0/1.0<br>*0.97(10)* | 0.0/1.0<br>*0.97(8)* |
| 2 | 11.57 | 3.16 | 0.0/1.0<br>*44(2)* | 0.5/0.5<br>*-1.68(11)* | 0.0/1.0<br>*0.73(9)* |
| 3 | 11.87 | 4.03 | 0.0/1.0<br>*30(1)* | 0.0/1.0<br>*1.52(13)* | 0.25/0.75<br>*-0.40(9)* |
| 4 | 11.37 | 3.40 | 0.143/0.856<br>*26(1)* | 0.143/0.856<br>*0.56(12)* | 0.143/0.856<br>*0.18(8)* |

*Note*:

Model 1: the O ions occupy only the $X$(1) site. (the final result in the text); model 2: $X$(2) site, model 3: $X$(3) site; model 4: fully disordered arrangement between O and S.

Table 6.2 The reliability factors of Rietveld analyses for $Eu_2ZnGe_2S_6O$ with the different O/S ion occupations.

| Model | $R_{wp}$ (%) | $R_B$ (%) | Occupancy of O/S ion and $B$ (Å$^2$) for three anion sites | | |
|---|---|---|---|---|---|
| | | | $X$(1) 2$c$ site | $X$(2) 4$e$ site | $X$(3) 8$f$ site |
| 1 (text) | 8.84 | 1.94 | 1.0/0.0<br>*0.87(41)* | 0.0/1.0<br>*0.87(10)* | 0.0/1.0<br>*0.87(8)* |
| 2 | 9.75 | 3.02 | 0.0/1.0<br>*56(2)* | 0.5/0.5<br>*-1.77(10)* | 0.0/1.0<br>*0.26(7)* |
| 3 | 10.15 | 2.97 | 0.0/1.0<br>*38(1)* | 0.0/1.0<br>*1.60(12)* | 0.25/0.75<br>*-0.81(8)* |
| 4 | 9.64 | 2.63 | 0.143/0.856<br>*32(1)* | 0.143/0.856<br>*0.54(11)* | 0.143/0.856<br>*-0.25(7)* |

*Note*:

Model 1: the O ions occupy only the $X$(1) site. (the final result in the text); model 2: $X$(2) site, model 3: $X$(3) site; model 4: fully disordered arrangement between O and S.

Table 6.3 Structural parameters for $Eu_2MGe_2S_6O$ ($M$ = Mn, Zn).

| Atom | Site | *X* | *Y* | *Z* | *B* (Å$^2$) |
|---|---|---|---|---|---|
| $Eu_2MnGe_2S_6O$[a] | | | | | |
| Eu | 4*e* | 0.1566(1) | 0.6566 | 0.5076(2) | 0.77(3) |
| Mn | 2*a* | 0 | 0 | 0 | 0.64(8) |
| Ge | 4*e* | 0.6259(2) | 0.1259 | 0.9110(3) | 0.45(5) |
| O(1) | 2*c* | 0 | 1/2 | 0.1915(24) | 0.97(41) |
| S(2) | 4*e* | 0.6372(3) | 0.1372 | 0.2586(6) | 0.95(6) |
| S(3) | 8*f* | 0.0622(3) | 0.1779(3) | 0.2534(5) | 0.95(6) |
| $Eu_2ZnGe_2S_6O$[b] | | | | | |
| Eu | 4*e* | 0.1580(1) | 0.6580 | 0.5022(2) | 0.83(3) |
| Zn | 2*a* | 0 | 0 | 0 | 0.89(7) |
| Ge | 4*e* | 0.6275(2) | 0.1275 | 0.9220(3) | 0.68(5) |
| O(1) | 2*c* | 0 | 1/2 | 0.1830(23) | 1.40(43) |
| S(2) | 4*e* | 0.6372(3) | 0.1372 | 0.2693(6) | 0.85(10) |
| S(3) | 8*f* | 0.0631(3) | 0.1734(4) | 0.2434(5) | 0.85(8) |

Note :

[a] Space group *P*-42$_1$*m* (No. 113), $Z$ = 2, $a$ = 9.4867(2) Å, $c$ = 6.1787(2) Å, $V$ = 556.07(2) Å$^3$, $R_{wp}$ = 10.08 %, $R_p$ = 7.21 %, $R_B$ = 2.15 %, and $R_F$ = 1.03 %.

[b] Space group *P*-42$_1$*m* (No. 113), $Z$ = 2, $a$ = 9.3966(3) Å, $c$ = 6.1586(2) Å, $V$ = 543.77(3) Å$^3$, $R_{wp}$ = 8.83 %, $R_p$ = 6.33 %, $R_B$ = 1.95 %, and $R_F$ = 0.95 %.

$R_{wp} = \{\sum_i w_i[y_i - f_i(x)]^2 / \sum_i w_i y_i^2\}^{1/2}$, $R_p = \sum_i |y_i - f_i(x)| / \sum_i y_i$,.

$R_B = \sum_K |I_0(\boldsymbol{h}_k) - I(\boldsymbol{h}_k)| / \sum_K I_0(\boldsymbol{h}_k)$ , and $R_e = [(N-P)/\sum_i w_i y_i^2]^{1/2}$ .

Table 6.4 Selected interatomic distances (Å) and bond valence sums.

| Cation sites | $Eu_2MnGe_2S_6O$ | $Eu_2ZnGe_2S_6O$ | Anion sites | $Eu_2MnGe_2S_6O$ | $Eu_2ZnGe_2S_6O$ |
|---|---|---|---|---|---|
| Eu-O(1) | 2.869(10) | 2.876(10) | O(1)-Ge × 2 | 1.804(5) | 1.814(5) |
| Eu-S(3) × 2 | 3.040(3) | 3.057(3) | O(1)-Eu × 2 | 2.869(1) | 2.876(10) |
| Eu-S(3)' × 2 | 3.055(3) | 3.061(3) | **BVS: O(1)** | **2.00** | **1.84** |
| Eu-S(2) × 2 | 3.145(3) | 3.116(3) | S(2)-Ge | 2.153(4) | 2.143(4) |
| Eu-S(2)' | 3.166(4) | 3.077(4) | S(2)-Eu × 2 | 3.145(3) | 3.116(3) |
| **BVS: Eu** | **1.93** | **1.99** | S(2)-Eu' | 3.165(4) | 3.077(4) |
| *M*-S(3) × 4 | 2.377(3) | 2.292(3) | **BVS: S(2)** | **1.84** | **1.96** |
| **BVS: *M*** | **2.61** | **2.32** | S(3)-Ge | 2.204(4) | 2.214(4) |
| Ge-O(1) | 1.804(5) | 1.814(5) | S(3)-*M* | 2.377(3) | 2.291(3) |
| Ge-S(2) | 2.153(4) | 2.143(4) | S(3)-Eu | 3.040(3) | 3.057(3) |
| Ge-S(3) × 2 | 2.204(4) | 2.214(4) | S(3)-Eu' | 3.055(4) | 3.061(3) |
| **BVS: Ge** | **4.11** | **4.07** | **BVS: S(3)** | **2.26** | **2.13** |

Table 6.5 Mössbauer parameters for $Eu_2MGe_2S_6O$ ($M$ = Mn, Zn).

| Compounds | | I.S. ($mm/s^{-1}$) | Q.S. ($mm/s^{-1}$) | $\eta$ | $\Gamma$ ($mm/s^{-1}$) | $A(Eu^{2+})/A(E^{u3+})$ |
|---|---|---|---|---|---|---|
| $Eu_2MnGe_2S_6O$ | Expt. | $Eu^{2+}$: -12.62(9) | 6.93(2) | 0.80(5) | 2.17(2) | 0.98 |
| | Calc. | - | 7.11 | 0.69 | - | - |
| | Expt. | $Eu^{3+}$: 0.43 (3) | - | - | 2.56(7) | - |
| $Eu_2ZnGe_2S_6O$ | Expt. | $Eu^{2+}$: -12.52(1) | 6.77(8) | 0.44(2) | 3.11(6) | 0.95 |
| | Calc. | - | 6.69 | 0.72 | - | - |
| | Expt. | $Eu^{3+}$: 0.48 (2) | - | - | 2.95(6) | - |

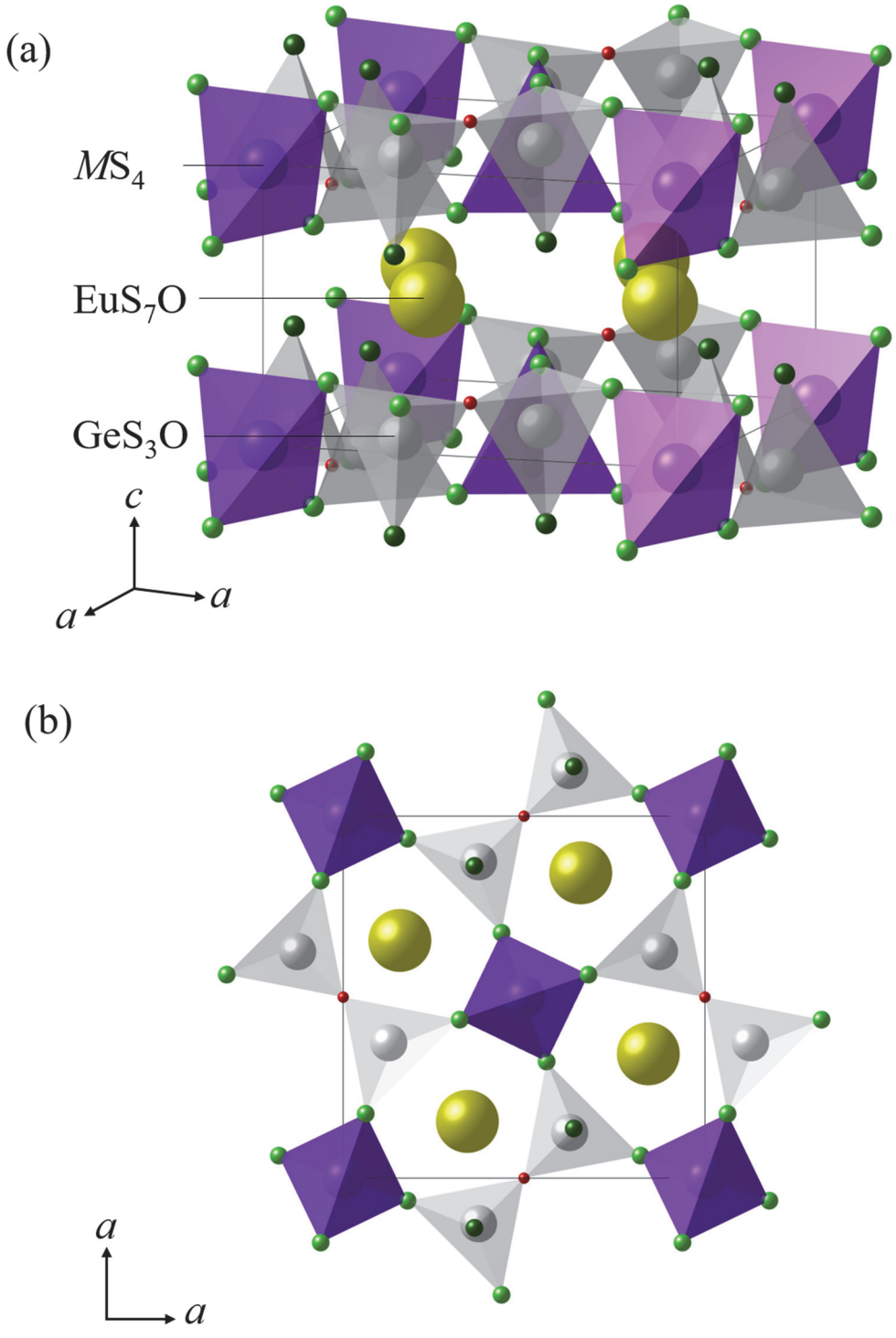


Figure 6.1 Schematic crystal structures of melilite-type $Eu_2MGe_2S_6O$: (a) standard orientation of crystal shape, (b) viewed from the c axis.

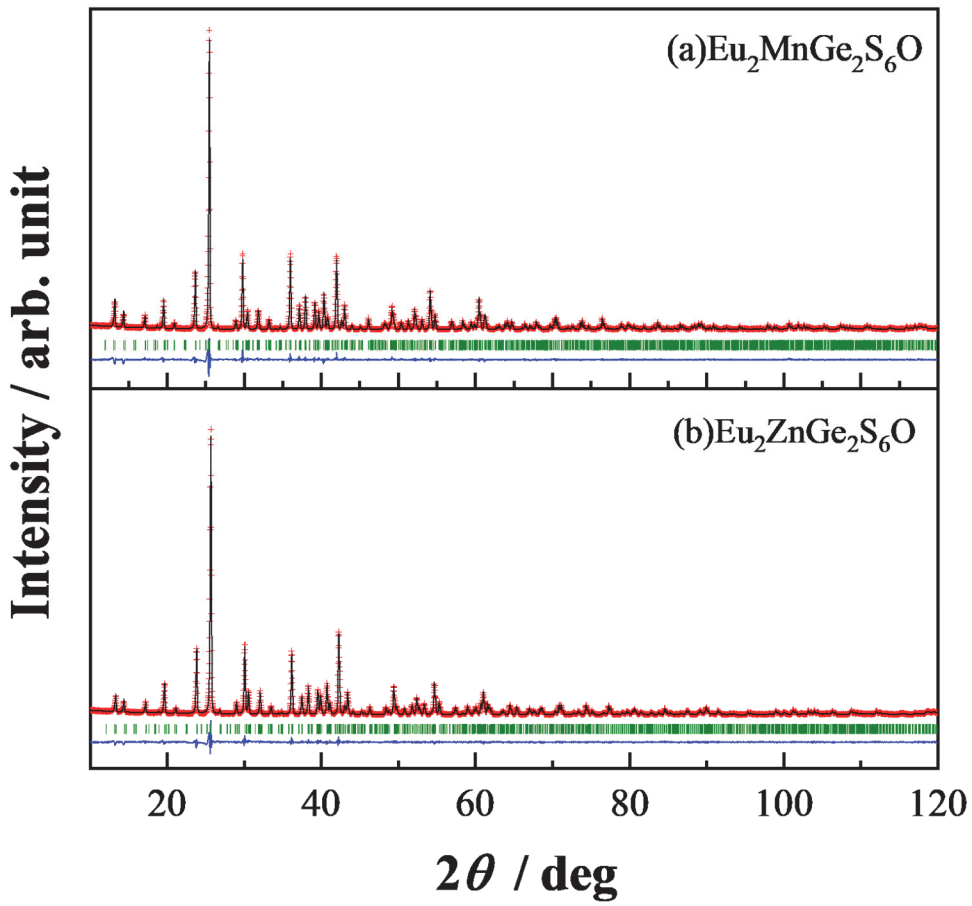


Figure 6.2 Powder XRD profiles for (a)$Eu_2MnGe_2S_6O$ and (b)$Eu_2ZnGe_2S_6O$. The calculated and observed profiles are shown as the top black solid line and red markers, respectively. The vertical marks in the middle show positions calculated for Bragg reflection. The lower trace is a plot of the difference between calculated and observed intensities.

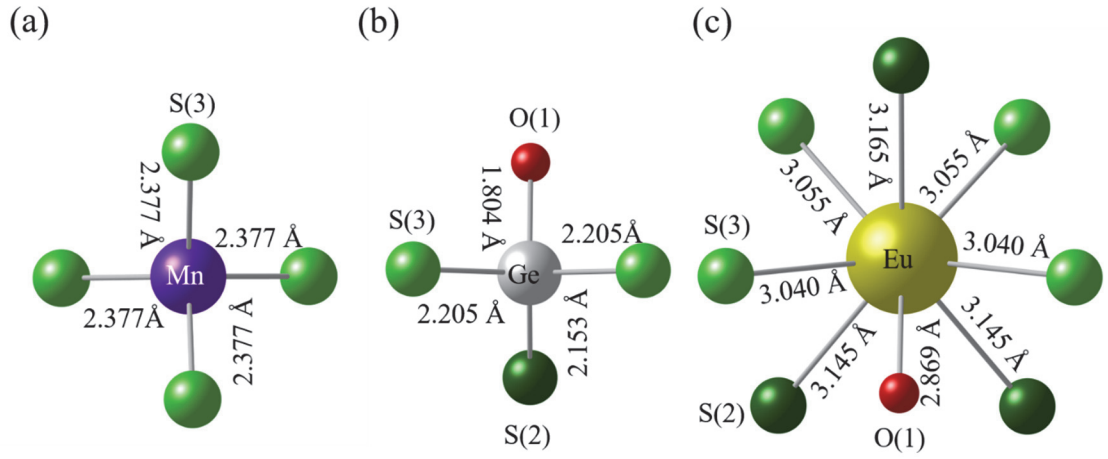


Figure 6.3 Schematic environment of the cation sites coordination for (a)Eu, (b)Mn and (c)Ge sites, respectively.

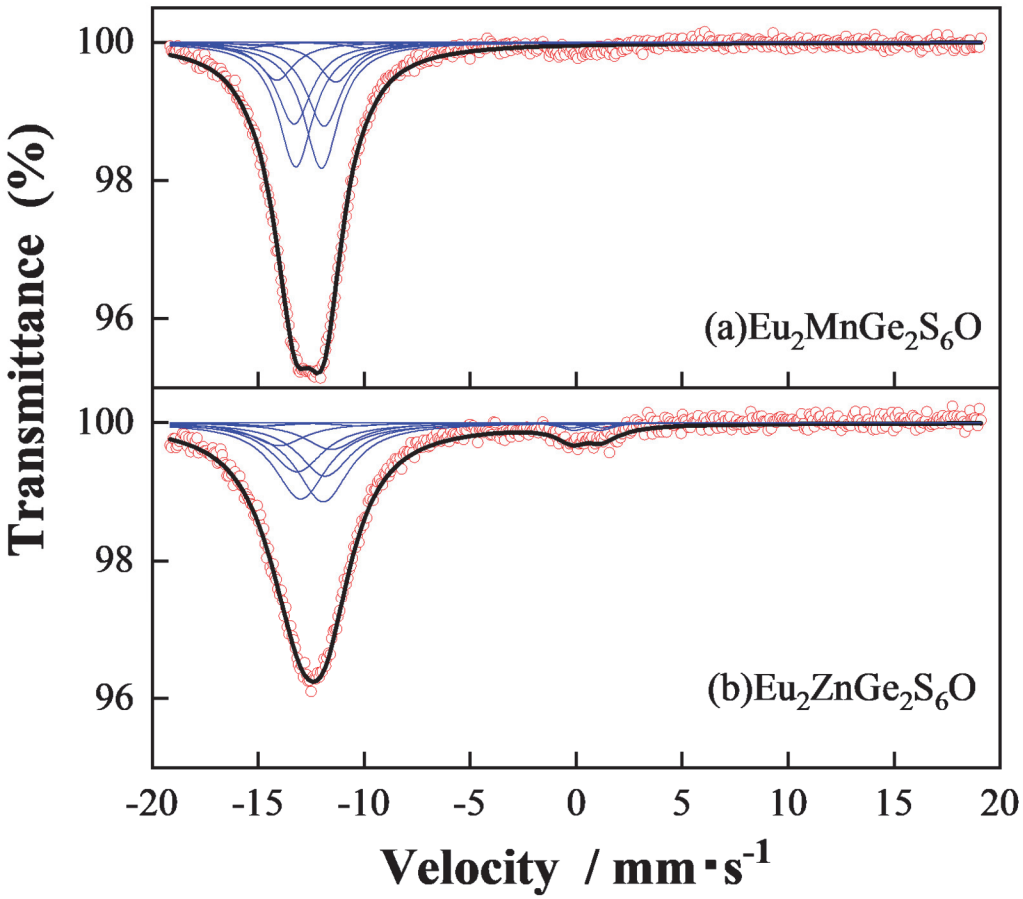


Figure 6.4 Mössbauer spectra for (a) $Eu_2MnGe_2S_6O$ and (b) $Eu_2ZnGe_2S_6O$. The observed spectra are shown on the red circles.

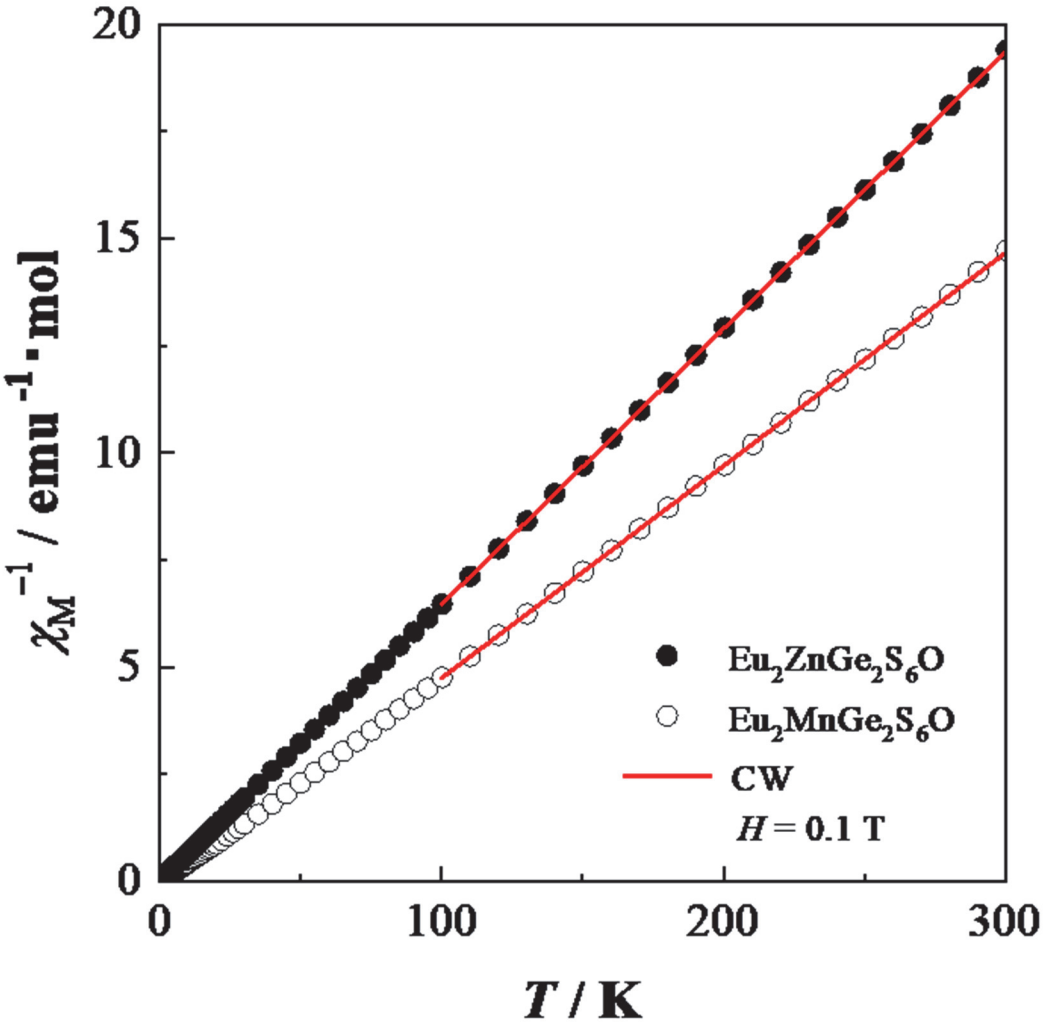


Figure 6.5 Temperature dependence of the reciprocal magnetic susceptibility for $Eu_2ZnGe_2S_6O$ and $Eu_2MnGe_2S_6O$.The red solid lines are fitting results by the Curie-Weiss law (CW).

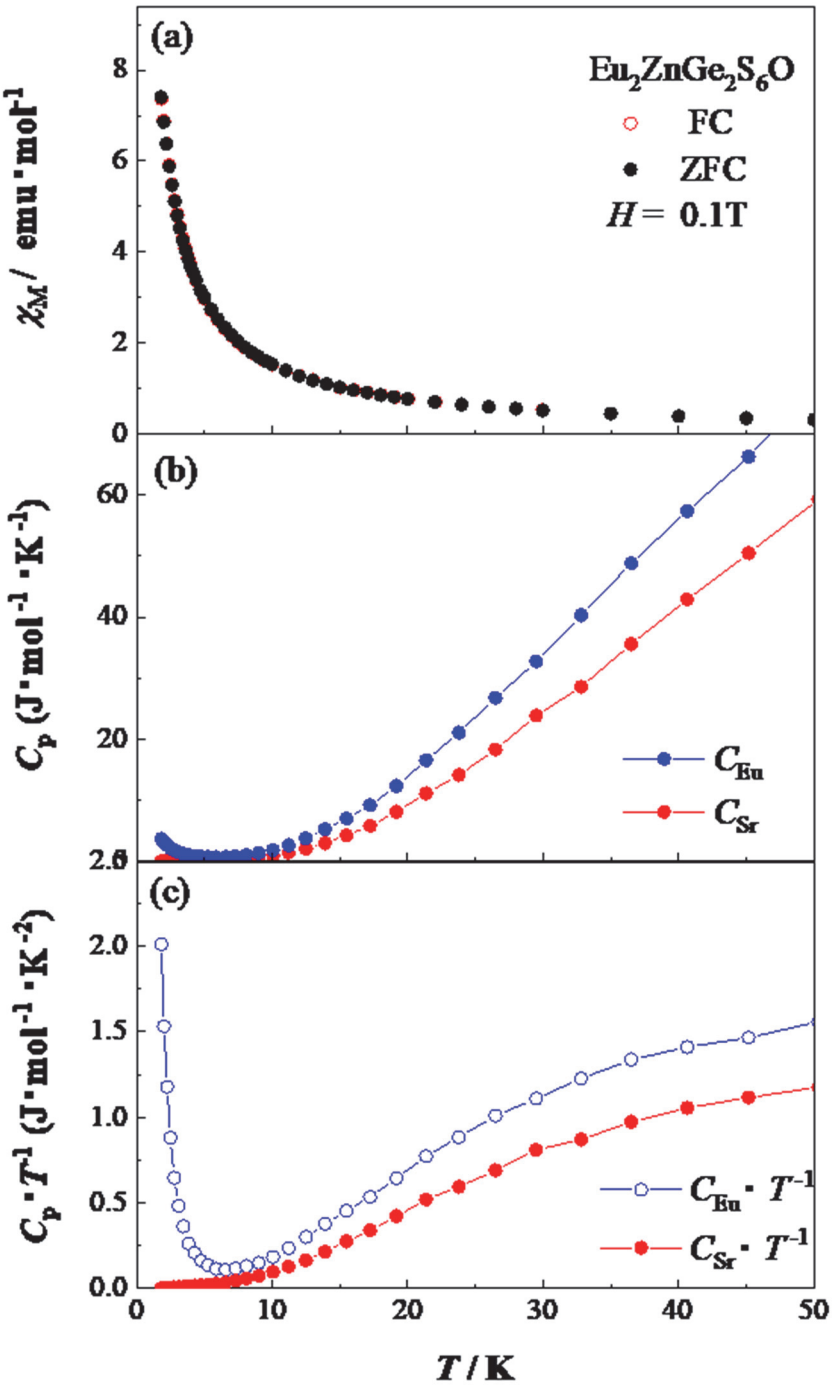


Figure 6.6 Temperature dependence of the magnetic susceptibility, specific heat($C_p$), magnetic specific heat divided by temperature ($C_{mag}$/T), and magnetic entropy of $Eu_2ZnGe_2S_6O$.

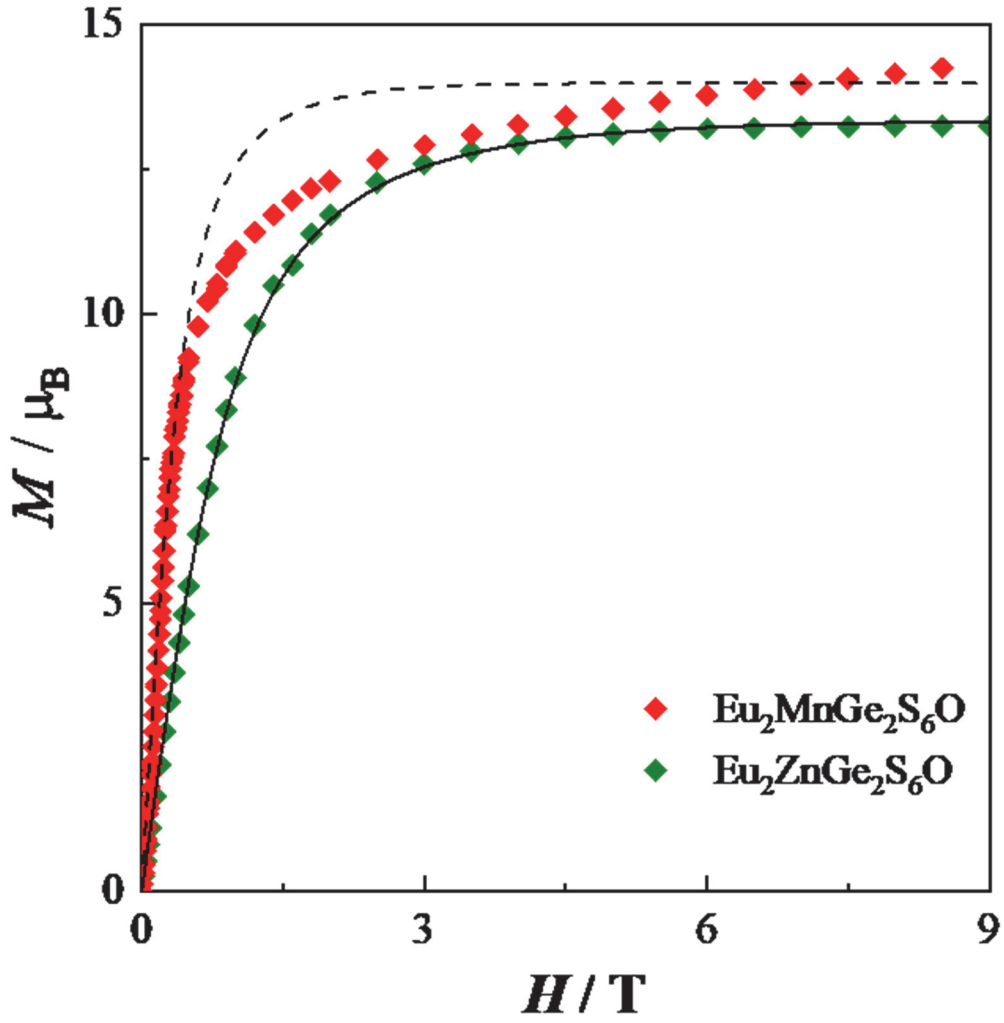


Figure 6.7 Field dependence of the magnetization for $Eu_2ZnGe_2S_6O$ and $Eu_2MnGe_2S_6O$ in the field range of 0 to 9 T.

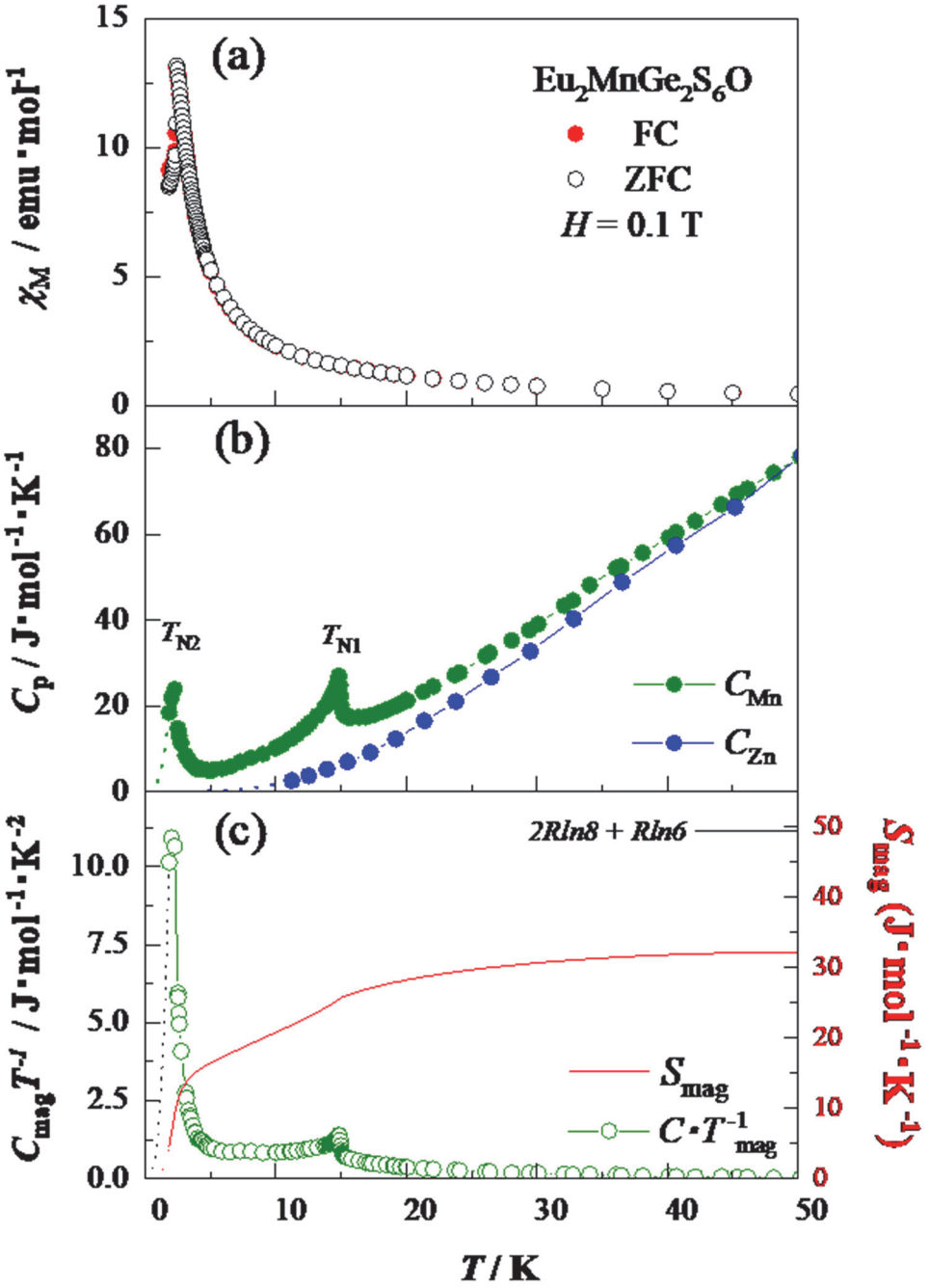


Figure 6.8 Temperature dependence of the magnetic susceptibility, specific heat($C_p$), magnetic specific heat divided by temperature ($C_{mag}$/T), and magnetic entropy of $Eu_2MnGe_2S_6O$.

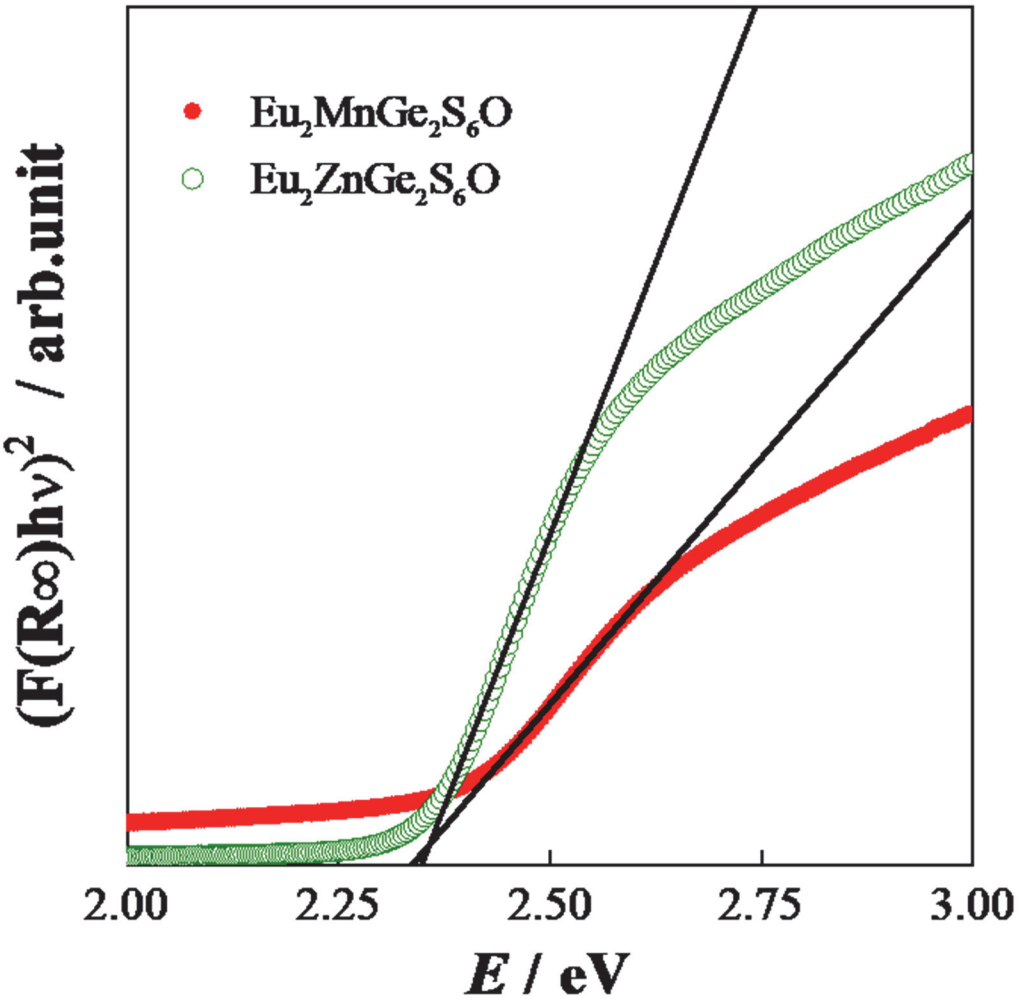


Figure 6.9 Diffuse reflectance spectrum of $Eu_2ZnGe_2S_6O$and $Eu_2MnGe_2S_6O$. The tauc plot is shown.

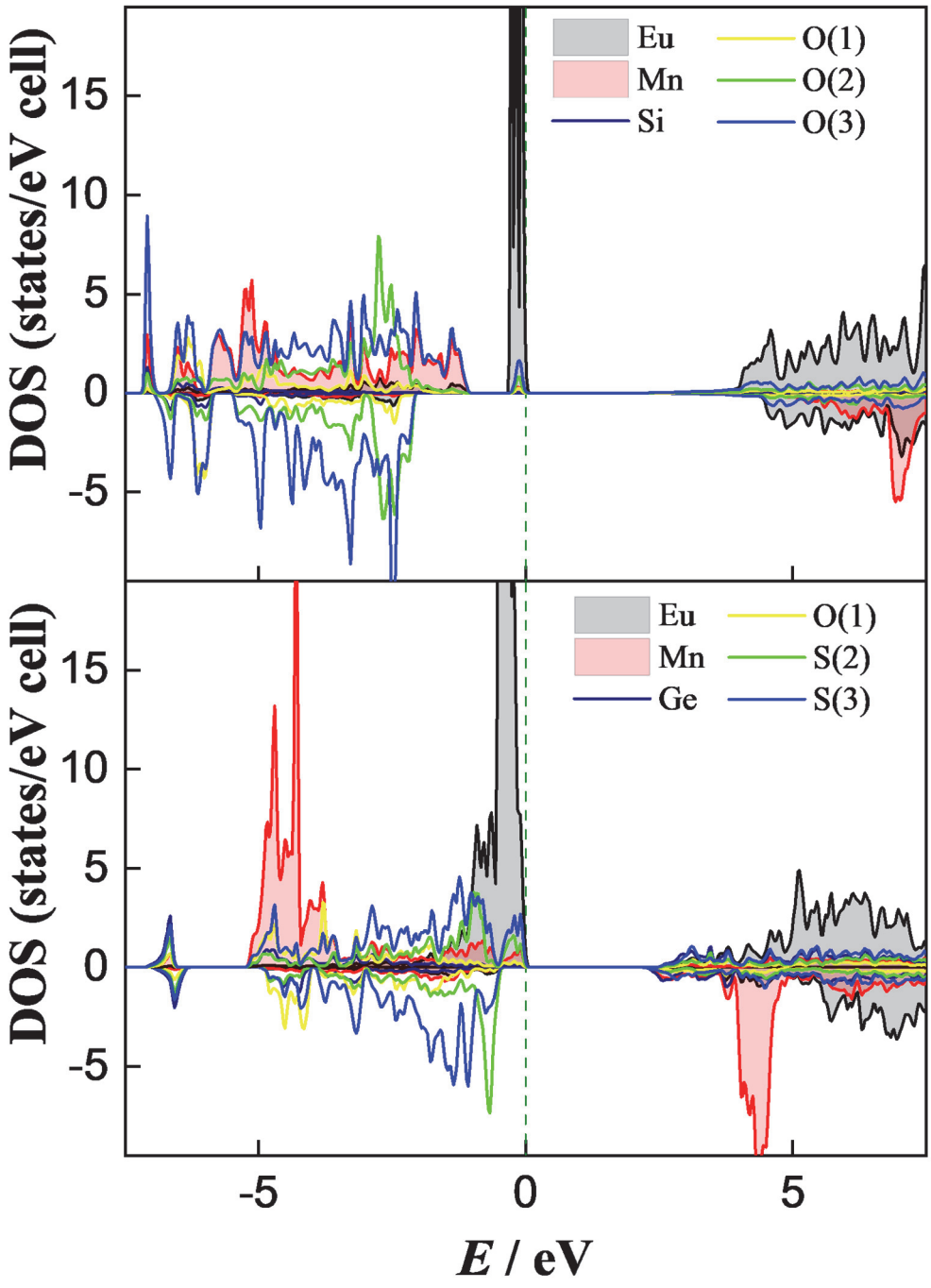


Figure 6.10 Density of states of (a)$Eu_2MnSi_2O_7$, and (b)$Eu_2MnGe_2S_6O$.

## 6.6 References

(1) Takahashi, H.; Igawa, K.; Arii, K.; Kamihara, Y.; Hirano, M.; Hosono, H. Superconductivity at 43 K in an Iron-Based Layered Compound $LaO_{1-x}F_xFeAs$. *Nature* **2008**, *453*, 376–378.

(2) Adamson, P.; Hadermann, J.; Smura, C. F.; Rutt, O. J.; Hyett, G.; Free, D. G.; Clarke, S. J. Competing Magnetic Structures and the Evolution of Copper Ion/Vacancy Ordering with Composition in the Manganite Oxide Chalcogenides $Sr_2MnO_2Cu_{1.5}(S_{1-x}Se_x)_2$. *Chem. Mater.* **2012**, *24*, 2802–2816.

(3) Luu, S. D. N.; Vaqueiro, P. Layered Oxychalcogenides: Structural Chemistry and Thermoelectric Properties. *J. Mater.* **2016**, *2*, 131–140.

(4) Clarke, S. J.; Adamson, P.; Herkelrath, S. J. C.; Rutt, O. J.; Parker, D. R.; Pitcher, M. J.; Smura, C. F. Structures, Physical Properties, and Chemistry of Layered Oxychalcogenides and Oxypnictides. *Inorg. Chem.* **2008**, *47*, 8473–8486.

(5) Stock, C.; McCabe, E. E. The Magnetic and Electronic Properties of Oxyselenides - Influence of Transition Metal Ions and Lanthanides. *J. Phys. Condens. Matter* **2016**, *28*, 453001.

(6) Narita, K. Crystal Structures of Nonmetalic Inclusion in Iron and Steel, and Its Homologue. *Trans. Iron Steel Inst. Japan* **1967**, *53*, 1024–1055.

(7) Kanno, R.; Murayama, M. Lithium Ionic Conductor Thio-LISICON: The $L_2S$-$GeS_2$-$P_2S_5$ System. *J. Electrochem. Soc.* **2001**, *148*, A742.

(8) Endo, T.; Doi, Y.; Wakeshima, M.; Suzuki, K.; Matsuo, Y.; Tezuka, K.; Ohtsuki, T.; Shan, Y. J.; Hinatsu, Y. Magnetic Properties of the Melilite-Type Oxysulfide $Sr_2MnGe_2S_6O$: Magnetic Interactions Enhanced by Anion Substitution. *Inorg. Chem.* **2017**, *56*, 2459–2466.

(9) Endo, T.; Doi, Y.; Hinatsu, Y.; Ohoyama, K. Magnetic and Neutron Diffraction Study on Melilite-Type Oxides $Sr_2MGe_2O_7$(*M*= Mn, Co). *Inorg. Chem.* **2012**, *51*, 3572–3578.

(10) Burzo, E. Melilites and Related Silicates. In *Sorosilicates*; Springer-Verlag: Berlin/Heidelberg, 2009; Vol. 14, pp 29–60.

(11) Kaminskii, A. A.; Bohatý, L.; Becker, P.; Liebertz, J.; Held, P.; Eichler, H. J.; Rhee, H.; Hanuza, J. Tetragonal $Ba_2MgGe_2O_7$ - a Novel Multifunctional Optical Crystal with Numerous Manifestations of Nonlinear-Laser Effects: Almost Sesqui-Octave Stokes and Anti-Stokes Combs and Cascaded $\chi$ (3) ↔ $\chi$ (2) Lasing with Involved Sec. *Laser Phys. Lett.* **2008**, *5*, 845–868.

(12) Masuda, T.; Kitaoka, S.; Takamizawa, S.; Metoki, N.; Kaneko, K.; Rule, K. C.; Kiefer, K.; Manaka, H.; Nojiri, H. Instability of Magnons in Two-Dimensional Antiferromagnets at High Magnetic Fields. *Phys. Rev. B* **2010**, *81*, 100402.

(13) Endo, T.; Doi, Y.; Wakeshima, M.; Hinatsu, Y. Crystal Structures and Magnetic Properties of New Europium Melilites $Eu_2MSi_2O_7$ (*M* = Mg, Mn) and Their Strontium Analogues. *Inorg. Chem.* **2010**, *49*, 10809–10814.

(14) Ochi, Y.; Morikawa, H.; Marumo, F.; Nozaki, H. Structures and Magnetic Properties of Rare Earth Compounds in the Melilite Group. *Yogyo Kyokaishi* **1983**, *91*, 229–235.

(15) Izumi, F.; Momma, K. Three-Dimensional Visualization in Powder Diffraction. *Solid State Phenom.* **2007**, *130*, 15–20.

(16) Momma, K.; Izumi, F. VESTA 3 for Three-Dimensional Visualization of Crystal, Volumetric and Morphology Data. *J. Appl. Crystallogr.* **2011**, *44*, 1272–1276.

(17) Blaha, P.; Schwarz, K.; Madsen, G.; Kvasnicak, D.; Luitz, J. WIEN2k, An Augmented Plane Wave Plus Local Orbitals Program for Calculating Crystal Properties.; 2001.

(18) Teske, C. L. Über Oxidsulfide Mit Åkermanitstruktur $CaLaGa_3S_6O$, $SrLaGa_3S_6O$, $La_2ZnGa_2S_6O$ Und $Sr_2ZnGe_2S_6O$. *Zeitschrift für Anorg. und Allg. Chemie* **1985**, *531*, 52–60.

(19) Brown, I. D.; Altermatt, D. Bond-Valence Parameters Obtained from a Systematic Analysis of the Inorganic Crystal Structure Database. *Acta Crystallogr. Sect. B Struct. Sci.* **1985**, *41*, 244–247.

(20) Brese, N. E.; O'Keeffe, M. Bond-Valence Parameters for Solids. *Acta Crystallogr. Sect. B* **1991**, *47*, 192–197.

(21) Shannon, R. D. Revised Effective Ionic Radii and Systematic Studies of Interatomic Distances in Halides and Chalcogenides. *Acta Crystallogr. Sect. A* **1976**, *32*, 751–767.

(22) Long, G. J.; Grandjean, F. *Mössbauer Spectroscopy Applied to Inorganic Chemistry Vol.3*; Plenum Press: New York, 1986.

(23) Shenoy, G. K.; Dunlap, B. D. Method for the Analysis of Pure Quadrupole Spectra in Nuclear Gamma-Ray Resonance. *Nucl. Instruments Methods* **1969**, *71*, 285–291.

(24) Raghavan, P. Table of Nuclear Moments. *At. Data Nucl. Data Tables* **1989**, *42*, 189–291.

(25) Blok, J.; Shirley, D. A. Systematic Variation of Quadrupole Crystal-Field Shielding in Rare-Earth Ethyl Sulfates. *Phys. Rev.* **1966**, *143*, 278–283.

(26) Stadnik, Z. M.; Stroink, G.; Arakawa, T. Quadrupole Interactions at Divalent and Trivalent Europium Sites in Several Europium Oxides. *Phys. Rev. B* **1991**, *44*, 12552–12558.

(27) Joshua, S. J.; Cracknell, A. P. The Spin-Wave Contribution to the Specific Heat of NiF2. *Phys. Lett. A* **1969**, *28*, 562–563.

(28) Neel, L. Propriétés Magnétiques Des Ferrites. Ferrimagnétisme et Antiferromagnétism. *Ann. Phys. Paris.* **1948**, *3*, 137–198.

(29) Kubelka, P.; Munk, F. Ein Beitrag Zur Optik Der Farbanstriche. *Z. Techn. Phys.* **1931**, *12*, 593.

(30) Tauc, J.; Grigorovici, R.; Vancu, A. Optical Properties and Electronic Structure of Amorphous Germanium. *Phys. Stat. Sol* **1966**, *15*, 627.

(31) Busch, G.; Güntherodt, G.; Wachter, P. Optical Transitions and the Energy Level Scheme of the Europium Chalcogenides. *Le J. Phys. Colloq.* **1971**, *32*, C1-928-C1-929.

(32) Imada, M. Metal-Insulator Transitions. *Rev. Mod. Phys.* **1998**, *70*, 1039–1263.

# Chapter 7

# Concluding Remarks

This dissertation presents the solid-state chemistry of some melilite-type oxides and oxysulfide $A_2MM'_2X_7$. Their crystal structures were determined by the Rietveld analysis for both the X-ray diffraction and the neutron diffraction profiles. The local structure around the Eu ions were cleared by the Mössbauer spectroscopy. The magnetic properties of their compounds were investigated by the DC magnetic susceptibility, magnetic hysteresis and specific heat measurements. Magnetic transitions were observed for some compounds and their magnetic structures were determined from the neutron diffraction measurements. To clarify the detail of the magnetic properties, we carried out the UV-vis spectroscopy measurements and DFT calculations.

## 7.1 Melilite-type oxide compounds

$Sr_2MM'_2O_7$ ($M$ = Mn, Co, $M'$ = Si, Ge) contain magnetic ions only at $M$ sites and crystalize in the tetragonal melilite structure with space group $P\text{-}42_1m$ ($a$ ~ 8 Å, c ~ 5Å). The coordination environments are very similar between them. The $M$ ions occupy tetrahedral sites in an ordered manner, and they form a square-planar lattice in the *ab* plane. Both compounds do not show the structural phase transition down to 2.5 K. The temperature dependence of magnetic susceptibility for $Sr_2MnGe_2O_7$ show a broad peak at ~6.0 K, which is due to the two-dimensional magnetic interaction between Mn ions in the *ab* plane. At 4.4 K, another antiferromagnetic transition was observed. The magnetic structure was determined by the neutron powder diffraction measurements at 2.5 K. It can be represented by the propagation vector $k$ = (0, 0, 1/2), and the magnetic moments of $Mn^{2+}$ (3.99 $\mu_B$) ions order antiferromagnetically in a colinear manner along the $c$ axis. On the other hand, the $Sr_2CoGe_2O_7$, shows an antiferromagnetic transition at 6.5 K with

divergence between zero-field-cooled and field-cooled susceptibilities due to Dzyaloshinsky-Moriya interaction. Its magnetic structure determined at 2.5 K has a magnetic propagation vector $k = (0, 0, 0)$, and the ordered magnetic moment of $Co^{2+}$ (2.81 $\mu_B$) adopts a colinear arrangement lying on the *ab* plane. This result is mainly due to the anisotropic character of the $Co^{2+}$ ions compared with the isotropic $Mn^{2+}$.

$Eu_2MgSi_2O_7$ contains magnetic ions only at *A* sites and crystalizes in the tetragonal melilite structure with space group $P\text{-}42_1m$ ($a$= 8.0138(2) Å, c = 5.1711(1)Å). The $^{151}$Eu Mössbauer measurements show that the Eu ions are in the divalent state. The magnetic susceptibility curve above 100 K was fitted with the Curie-Weiss law. The Weiss constant were determined to be -1.2(4) K, which may indicate the existence of the antiferromagnetic interaction between Eu ion; however. no magnetic transition is observed down to 1.8 K. This result is due to relatively weak Eu-O-Eu magnetic interaction.

$Eu_2MnSi_2O_7$ is the melilite-type compounds containing magnetic ions at both *A* and *M* sites. From the XRD profiles, the observed diffraction lines were indexed in a tetragonal unit cell. This compound crystallizes in the tetragonal melilite structure with space group $P\text{-}42_1m$ ($a$ = 8.1390(2) Å, c = 5.1635(1)Å). The coordination environments are very similar to those for $Sr_2MnSi_2O_7$, which reflects almost the same ionic radii between $Sr^{2+}$ (1.26Å) and $Eu^{2+}$ (1.25Å). The $^{151}$Eu Mössbauer measurements show that the Eu ions are in the divalent state. The temperature dependence of magnetic susceptibility shows a ferrimagnetic transition at 10.7 K. From the magnetization and specific heat measurements, it is found that the $Eu^{2+}$ (14 $\mu_B$) and $Mn^{2+}$ (5 $\mu_B$) sublattices order antiferromagnetically. This result indicates that an interaction between *f-d* electrons (Eu-Mn) predominantly operate in this compound.

## 7.2 Melilite-type oxysulfide compounds

$A_2MGe_2S_6O$ ($A$ = Sr, Eu, $M$ = Zn, Mn) are crystallizes in the melilite structure with space group $P\text{-}42_1m$. In this structure, the $S^{2-}$ and $O^{2-}$ ions occupy different crystallographic sites in an ordered manner. The temperature dependence of the magnetic susceptibility of $Sr_2MnGe_2S_6O$ shows a broad peak due to a two-dimensional magnetic interaction between Mn ions in the *ab* plane. The specific heat data show that this compound has an antiferromagnetic transition temperature ($T_N$ = 15.5 K) which is much higher than that of the oxide analogue $Sr_2MnGe_2O_7$ ($T_N$ = 4.4 K).

The temperature dependence of magnetic susceptibility for Eu-containing oxysulfide $Eu_2ZnGe_2S_6O$ shows the paramagnetic down behavior to 1.8 K. On the other hand, the $Eu_2MnGe_2S_6O$ shows antiferromagnetic behavior at low temperatures. The specific heat data of $Eu_2MnGe_2S_6O$ show two anomalies at $T_{N1}$ = 14.8 K and $T_{N2}$ = 2.3 K. The former anomaly is very similar to that found in analogues $Sr_2MnGe_2S_6O$ at 15.5 K, indicating an antiferromagnetic transition of $Mn^{2+}$ ions. Both the magnetic susceptibility and specific heat data show an anomaly at 2.3 K suggesting the existence of another magnetic transition. DFT calculation showed that the magnetic interaction is enhanced by covalency in the Mn-S bonding.

It is concluded that melilite-type compounds containing both lanthanide and transition metal ions show interesting magnetic properties, which are originated from the characteristics of crystal structure and the magnetic interactions. In order to deepen this understanding and to find more fascinating magnetic properties, further investigations on compounds containing other metal ions or related crystal structures such a fresnoite compounds will be required.

# List of Publications

[Thesis]

Original papers

(1) Endo, T.; Doi, Y.; Wakeshima, M.; Hinatsu, Y. Crystal Structures and Magnetic Properties of New Europium Melilites $Eu_2MSi_2O_7$ ($M$ = Mg, Mn) and Their Strontium Analogues. *Inorg. Chem.* **2010**, *49*, 10809–10814.

(2) Endo, T.; Doi, Y.; Hinatsu, Y.; Ohoyama, K. Magnetic and Neutron Diffraction Study on Melilite-Type Oxides $Sr_2MGe_2O_7$($M$= Mn, Co). *Inorg. Chem.* **2012**, *51*, 3572–3578.

(3) Endo, T.; Doi, Y.; Wakeshima, M.; Suzuki, K.; Matsuo, Y.; Tezuka, K.; Ohtsuki, T.; Shan, Y. J.; Hinatsu, Y. Magnetic Properties of the Melilite-Type Oxysulfide $Sr_2MnGe_2S_6O$: Magnetic Interactions Enhanced by Anion Substitution. *Inorg. Chem.* **2017**, *56*, 2459–2466.

Other papers

(1) Fuwa, Y.; Endo, T.; Wakeshima, M.; Hinatsu, Y.; Ohoyama, K. Orthogonal Spin Arrangement in Quasi-Two-Dimensional $La_2Co_2O_3Se_2$. *J. Am. Chem. Soc. commun.* **2010**, *132*, 18020–18022.

(2) Endo, T.; Sugino, Y.; Ohono, N.; Ukai, S.; Miyazaki, N.; Wang, Y.; Ohnuki, S. Three-Dimensional Characterization of ODS Ferritic Steel Using by FIB-SEM Serial Sectioning Method. *Microscopy* **2014**, *63*, i23–i23.

(3) Yanase, T.; Kawahito, A.; Hashimoto, Y.; Endo, T.; Wang, Y.; Nagahama, T.; Shimada, T. Fe Whisker Growth Revisited: Effect of Au Catalysis for [02̄] Oriented Nanowires with 100 nm Diameter. *RSC Adv.* **2014**, *4*, 27620–27624.

(4) Kawahito, A.; Yanase, T.; Endo, T.; Nagahama, T.; Shimada, T. Fabrication of Fe Nanowires on Yittrium-Stabilized Zirconia Single Crystal Substrates by Thermal CVD Methods. *J. Appl. Phys.* **2015**, *117*, 17D506.

(5) Nagakura, H.; Wakasugi, T.; Ohkubo, K.; Tanioka, T.; Endo, T.; Isobe, S.; Wang, Y.; Hashimoto, N.; Ohnuki, S. B12-O-21 Development of High Pressure Gas Environmental Cell and Its Application to Hydrogen Reaction. *Microscopy* **2015**, *64*, i29–i29.

(6) Xie, W.; Kawahito, A.; Miura, T.; Endo, T.; Wang, Y.; Yanase, T.; Nagahama, T.; Otani, Y.; Shimada, T. Colorful Carbon Nanopopcorns Formed by Codepositing $C_{60}$ with Diamond-like Carbon Followed by Reaction with Water Vapor. *Chem. Lett.* **2015**, *44*, 1205–1207.

(7) Kim, K. H.; Yoshihara, Y.; Abe, Y.; Kawamura, M.; Kiba, T.; Endo, T. Effects of Ni Dopant on Structural Properties of Zinc Oxide Nanorods. *Microelectron:Eng*: **2016**, 165, 20–22.

(8) Hasegawa, T.; Endo, T.; Tsuchiya, E.; Kudo, A.; Shen, Z.; Moritani, Y.; Abe, M.; Yamamoto, T.; Hongo, H.; Tsuboi, K.; Yoshida, T.; Nagai, T.; Khadiza, N.; Yokoyama, A.; Luiz de Freitas, P. H.; Li, M.; Amizuka, N. Biological Application of Focus Ion Beam-Scanning Electron Microscopy (FIB-SEM) to the Imaging of Cartilaginous Fibrils and Osteoblastic Cytoplasmic Processes. *J. Oral Biosci.* **2017**, *59*, 55–62.

(9) Hosono, A.; Masubuchi, Y.; Endo, T.; Kikkawa, S. Molten $BaCN_2$ for the Sintering and Crystal Growth of Dielectric Oxynitride Perovskites $Sr_{1-x}Ba_xTaO_2N$ ($x$ = 0.04–0.23). *Dalt. Trans.* **2017**, *46*, 16837–16844.

# Acknowledgements

I would like to express my great appreciation and gratitude to Professor Yukio Hinatsu for his invaluable comments, suggestions, and constant encouragement during the period of this thesis. I also wish to thank Professors Sadamu Takeda, Masako Kato, Kiyoharu Tadanaga who acted as examiners of this dissertation for their helpful and useful suggestions.

I especially would like to express my deepest appreciation to my supervisor, Dr. Yoshihiro Doi for his elaborated guidance, considerable encouragement and invaluable discussion that make my research of great achievement and my study life unforgettable.

I am deeply grateful to Dr. Makoto Wakeshima for many valuable discussions and constant encouragement. My thanks are also due to all the members who studied together with me at *Inorganic Chemistry Laboratory*.

I would also like to thank Professor Noboru Kitamura, Professor Yasutaka Matsuo Professor, Mr. Keita Suzuki in Hokkaido University, Dr. Keitaro Tezuka in Utsunomiya University, Dr. Eri Sakuda in Nagasaki University, Dr. Akitaka Ito in Kouchi University of Technology, Dr. Kenji Ohoyama in Tohoku University, for their help with the measurement and analysis of XPS, UV-vis and powder neutron diffraction data.

Special thanks are expressed to my colleagues; Emeritus Professor Soumei Ohnuki, Professor Naoyuki Hashimoto, Dr. Yongming Wang, Mr. Nobuyuki Miyazaki, Ms. Rena Ota and Ms. Ryoko Yokohira for their experimental support.

I would like to acknowledge for the supports by the “Global COE” Program (Project No. B01: Catalysis as the Basis for Innovation in Materials Science) and “Hokkaido University Ambitious Leader’s Program – fostering Future Leaders to Open New Frontiers in Materials Sciences –”. A part of this work was conducted at “Joint-use Facilities: Laboratory of Nano-Micro Material Analysis”, Hokkaido University, supported by “Advanced Physical Property Open Unit (APPOU)”, “Material Analysis

and Structure Analysis Open Unit (MASAOU)" and "Nanotechnology Platform" Program of the Ministry of Education, Culture, Sports, Science and Technology (MEXT), Japan.

Finally, I sincerely thank my family for their constant encouragement, understanding and support.